OUKA
Osaka University Knowledge Archive

Title	Molecular Dynamics Study on the Phase Interfaces of Water-Alcohol Mixtures and Relevance of Macro-Scale Wetting Theory on Microscopic Droplets
Author(s)	Surblys, Donatas
Citation	大阪大学, 2014, 博士論文
Version Type	VoR
URL	https://doi.org/10.18910/50522
rights	
Note	

Osaka University Knowledge Archive : OUKA

https://ir.library.osaka-u.ac.jp/

Osaka University

Doctoral Dissertation

Molecular Dynamics Study on the Phase Interfaces of Water-Alcohol Mixtures and Relevance of Macro-Scale Wetting Theory on Microscopic Droplets

Donatas Surblys

July 2014

Graduate School of Engineering,
Osaka University

Contents

List of Figures

List of Tables

Nomenclature

Roman Symbols

A	area
d	distance
$\mathrm{d}W$	Wiener noise
E	kinetic energy
E_r	rotational kinetic energy
E_{set}	control kinetic energy
E_t	translational kinetic energy
$\vec{e}$	position vector
f	mass fraction
$\vec{F}$	force vector
g	Gibbs free energy per unit area
H	effective enthalpy
H_{cut}	Heaviside step function
h	time step
$\mathbf{I}$	intertia moment matrix
k	spring constant
k_b	Boltzmann constant
l	height
l_{ctrl}	pressure control region distance to system center
m	mass
N	number of particles
N_f	number of degrees of freedom
N_P	number of pressure control directions
$\vec{n}$	unit normal vector
$\vec{n}^z$	unit vector to $+z$-direction
P	pressure
P^N	normal pressure
P^T	tangential pressure
P_Φ	potential energy component contributing to pressure
P_{set}	control pressure
P_E	kinetic energy component contributing to pressure
ΔP	Laplace pressure
$\mathbf{Q}$	quaternion matrix
q	electric charge
$\vec{q}$	quaternion vector
R	radius
$\mathbf{R}$	rotation matrix
r_0	equilibrium distance
r_{cut}	cut-off distance
$\vec{r}$	position vector
T	temperature
T_{set}	control temperature
$\vec{T}$	torque vector
t	time
V	volume
$\vec{v}$	velocity vector
W	piston inertia
X	random number from unit Gaussian distribution
Z	interface position

Greek Symbols

α	Euler angle
α_{damp}	damping coefficient
β	Euler angle
Γ	relative adsorption
γ	Euler angle
γ^{lv}	liquid-vapor interfacial tension
γ^{sl}	solid-liquid interfacial tension

NOMENCLATURE

γ^{lv}	solid-vapor interfacial tension
ε	energy parameter of Lennard-Jones potential
η	proportional to volume change rate
Θ	angle
θ	contact angle
λ	Lagrangian multiplier
λ_{deb}	Debye temperature
λ_{set}	temperature scaling factor
μ	chemical potential
ρ_{W}	number density of surface particles
σ	length parameter of Lennard-Jones potential
σ_{F}	standard deviation of random force
τ_P	barostat relaxation time
τ_T	thermostat relaxation time
Φ	potential energy
$\vec{\omega}$	angular velocity vector

Superscripts

(0)	initial state or value
b	body-fixed frame

Subscripts

sl	slab
C	Coulomb
ctrl	pressure control region
LJ	Lennard-Jones
W	wall

Other Symbols

$\hbar$	reduced Planck constant

Acronyms

IPA	isopropyl alcohol
MeOH	methanol

1

INTRODUCTION

1.1 Background

1.1.1 Wetting

In everyday life, we are constantly in contact with liquids, of which water makes the largest part. Liquids are not only abundant around ourselves, but our body itself depends on their properties to function properly. One of the most important properties that determine how liquids interact with their environment is wettability, which is the ability of a liquid to maintain contact with a solid surface, resulting from the intermolecular interaction between the two substances. A famous example of how wettability plays a crucial role in nature is the lotus effect, where water droplets on a lotus leaf do not adhere to it, but retain their round shape and collect any dirt particles in their proximity, thus performing a cleaning function.[1,2] At the other end of the wettability spectrum, several types of pitcher plants use highly wettable surfaces to make insects slip into their traps more easily.[3] The importance of wettability is in no way limited to plant life: for example, it has been reported that wettability highly influences gecko adhesion to wet surfaces.[4]

An early and groundbreaking work on wettability was done by Young in 1805,[5] where he formulated that the contact angle of a droplet is determined by the horizontal force balance among interfacial tensions at the three-phase interface. Especially recently, wettability has come to play an increasing role in various industrial processes, such as quenching oils,[6] oil recovery,[7] coating,[8] lubrication,[9] printing[10] and semiconductor manufacturing.[11] A typical example where wettability plays a crucial role is recent industrial printing technology, in which the required resolution has reached up to nanometer scale in high-speed relief or gravure printing processes. Another example is the semiconductor industry, where mass production of 14 nm-scale transistors is

scheduled to start in year 2014, and cleaning and rinsing with liquids at this scale is still needed. For those processes, profound understanding of the wettability behavior of a liquid with a solid surface at a micro- or nano-scale might provide new insights to help control and maintain the resulting quality.

1.1.2 Young's equation and wettability in the micro-scale

It has been argued that the relation put forth by Young is not enough to be used at micro-scale, and proposals, such as the introduction of a microscopic contact angle,[12] adding an additional line tension for the three-phase interface[13,14] and taking precursor films into account,[15] have been put forward, but experimental validation has so far been difficult as the evaluation of solid-liquid and solid-vapor interfacial tensions is a non-trivial task.[16,17]

On the other hand, computer simulation proved to be a valuable tool in this field. Already in year 1949, Kirkwood and Buff published a paper which provided a relation of the surface tension to the intermolecular potential and molecular distribution functions,[18] which formed the basis of the methods used in Monte Carlo simulations to evaluate interfacial tension. In 1990, Nijmeijer devised microscopic expressions for the surface and line tensions,[19] which enabled direct calculation of these interfacial tensions from the pressure distribution profiles, that could be readily evaluated by molecular dynamics (MD) simulations. In the same year, Nijmeijer followed up with his own MD simulation of a mono-atomic Lennard-Jones (L-J) liquid film on a solid surface, and demonstrated that even at nano-scale the Young's relation is applicable.[20] The validity of Young's relations has also been confirmed for a phase-separated binary mixture of L-J fluids by Das and Binder by using Monte Carlo simulations.[21] Savano et al.[22] have carried out MD simulations mimicking a macro-scale experiment, where they immersed a rod of nano-scale size into an L-J liquid, and concluded that Young's relation is applicable to this case as well. A number of research has gone beyond of just validating the Young's relation and studies on the wetting of L-J system have also been carried out e.g. for molecular-level roughness of the surface,[23] effect of the potential well depth of the interatomic solid-liquid interaction,[24] wetting of spherical particulates,[25] or sessile droplet.[26] Nishida et al.[4] of our research group succeeded at *in situ* extraction of the pressure distribution of an L-J droplet on a solid surface, and provided insight into the transition layers at various droplet interfaces.

1.1.3 Wetting in water-alcohol mixture systems

Adding minute amounts of alcohol is a well-known way in various industrial fields to radically change the wetting behavior of water, and it has also been experimentally confirmed that there is a considerable decrease in liquid-vapor interfacial tensions.[28] Up until now, empirical data and statistical mechanics have been used to create expressions capable of predicting the surface tension of mixtures, and while some success has been met,[29–31] a quantitatively precise and universal expression has not been derived yet. Unfortunately, as can be seen from the discussion up to this point, most extensive simulation research concerning wettability has been done on either single-phase or separate-phase mono-atomic L-J liquids. Because both water and alcohol molecules have a three-dimensional structure and are highly polar, i.e. strongly governed by Coulomb interactions, the results obtained from mono-atomic L-J liquid systems cannot be applied to water-alcohol mixtures in a straightforward manner. There is a need to conduct simulations with systems closer to the real world alcohol-mixture systems.

At the point of writing, few computational simulation works have been published dealing with the wettability of water-alcohol mixtures. Wilson and Pohorille investigated the adsorption of a single methanol or ethanol molecule on the liquid-vapor interface of water.[32] They calculated the free energy profiles and found that there was a deep minimum at the interface, pointing to substantial surface excess concentrations. The concentrations calculated from the Gibbs adsorption isotherm showed a good agreement with experimental results. Later publications directly investigated the liquid-vapor interfaces of water-alcohol mixture systems, where they discovered a strong tendency for alcohols to gather at the liquid-vapor interface and found the interfacial tensions to be consistent with what was observed experimentally,[33,34] as earlier predicted by Wilson and Pohorille. There is even less work done in dealing with the wettability of water-alcohol mixture droplets. Lundgren et al.[35] performed simulations of water-ethanol mixture droplets on a graphite surface and noted that ethanol molecules gather not only at the liquid-vapor, but also at the solid-liquid interface. They also noted that the decrease in the contact angle was significant compared to a pure water droplet, which was in accordance with experimentally observed results. Unfortunately, they did not conduct more detailed investigation on the interfaces, such as calculating the interfacial tensions. It is apparent that currently there are only some works done on the liquid-vapor interfaces and their interfacial tensions, which puts us in the same predicament as faced by experiments: because of the lack of information on

solid-liquid and solid-vapor interfaces, we cannot consistently evaluate the wettability of water-alcohol mixture systems. This study aims to remedy this by providing detailed analysis of the interfaces and the interfacial tensions occurring there.

1.2 Objectives

The objective of this work is to investigate the effect of alcohol additives on droplet wettability, where methanol and IPA are chosen as the alcohol components because of their wide industrial use, abundance of experimental data and ease of implementation. By employing molecular dynamics, not only a direct observation of molecule structure and movement is possible, but interfacial tensions can also be directly calculated, which is a non-trivial task to do experimentally. This will enable direct observation of change inside droplets and their interfaces, allowing to precisely determine the main factors causing wettability change.

Another primary objective of this work is to validate if the wetting theory used in macro-scale is still applicable to nano-scale mixture droplets. It is important to note that molecular-scale phenomena, such as the composition of the three-phase interface, are not pursued thoroughly in this work. Rather, droplets are treated using the macroscopic wetting theory, where an idealized model of interfaces with zero thickness is applied, although the actual interfaces have transition layers of finite thickness.

A secondary objective is to evaluate the validity of the methods used to obtain these interfacial tensions.

1.3 Paper Outline

This study deals with droplet systems and systems containing planar interfaces using MD simulation. The main focus is on two-phase solid-liquid and liquid-vapor interfaces, where their compositions and interfacial tension are investigated.

Chapter 2 describes the outline and theory of molecular dynamics method as well as non-trivial analysis methods used in this research. Specifically, the handling of pressure and interfacial tensions in MD is described.

Chapter 3 deals with the creation and analysis of water-methanol and water-IPA mixture droplets on a solid surface. The density distribution profiles as well as the Laplace pressure in the droplets are calculated and droplet wettability is evaluated using the contact angle.

Chapter 4 contains the quasi-one-dimensional water-alcohol systems. Systems with either planar solid-liquid and liquid-vapor or only solid-vapor interfaces are created and the interfacial tensions are directly calculated. Molecular orientations at solid-liquid and liquid-vapor interfaces are also investigated.

Chapter 5 has another type of quasi-one-dimensional systems to be used for thermodynamic integration, which provides an alternative way to obtain solid-liquid interfacial tensions.

Chapter 6 summarizes the data obtained in the previous chapters to confirm if the macro-scale wettability model, i.e. the Young's equation, is also valid for the droplets constructed in Chapter 3. Afterwards, the validity of the method used to obtain solid-liquid and liquid-vapor interfacial tensions in Chapter 4 is investigated.

2

MOLECULAR DYNAMICS METHOD AND THEORY

2.1 Equations of Motion

The molecular dynamics (MD) method calculates the time evolution of a system by solving discretized equations of motion for every particle. Particles are basically assumed to consist of a single mass point or a set of mass sites with relative positions fixed. For most of the simulations particles are assumed to behave according to classical Newtonian mechanics as well as Eulerian mechanics in case of rotational motion. However, in several cases Newton's equations for translational motion are modified to produce isothermal-isobaric systems, although rotational motion always follows Euler's equations. For multiple site particles, their movement is implemented as a rigid body motion.

2.1.1 Translational motion

Translational movement of the center of particle's mass is expressed by Newton's second law of motion

$$m\frac{\mathrm{d}^2\vec{r}}{\mathrm{d}t^2} = \vec{F}, \tag{2.1}$$

where m and $\vec{r}$ denote total mass and positional vector of the center of mass of a particle, respectively, and t designates time. The total force $\vec{F}$ in right-hand side of Equation 2.1 is a sum of outside forces, such as gravity, and forces due to interactions with other particles working on interaction sites situated on the particle. Suppose there are N particles and each particle consists of n_i $(i = 1, \cdots, N)$ interaction sites with their positions $\vec{r}_i^{\,1}, \cdots, \vec{r}_i^{\,n_i}$ and the potential energy function $\Phi\left(\vec{r}_1^{\,1}, \cdots, \vec{r}_1^{\,n_1}, \cdots, \vec{r}_N^{\,1}, \cdots, \vec{r}_N^{\,n_N}\right)$

only depends on interaction site positions, then the total force $\vec{F}_i$ being applied to particle i due to the potential interaction can be derived by partial differentiation

$$\vec{F}_i = -\sum_{j=1}^{n_i} \frac{\partial \Phi}{\partial \vec{r}_i^{\,j}}, \tag{2.2}$$

while the position of center of mass $\vec{r}_i$ is written as

$$\vec{r}_i = \frac{\sum_{j=1}^{n_i} m_i^j \vec{r}_i^{\,j}}{\sum_{j=1}^{n_i} m_i^j}. \tag{2.3}$$

The equation of motion of the center of mass with a total mass m_i thus becomes

$$m_i \frac{\mathrm{d}^2 \vec{r}_i}{\mathrm{d}t^2} = \vec{F}_i. \tag{2.4}$$

To make numerical integration possible, velocity $\vec{v}_i$ is introduced as an independent variable and Equation 2.4 is rewritten into two equations as

$$\frac{\mathrm{d}\vec{r}_i}{\mathrm{d}t} = \vec{v}_i, \tag{2.5}$$

$$m_i \frac{\mathrm{d}\vec{v}_i}{\mathrm{d}t} = \vec{F}_i. \tag{2.6}$$

By numerically integrating Equations 2.5 and 2.6, the velocity and position can be obtained.

2.1.2 Rotational motion

Most simulations in this research are done with particles assumed to be rigid bodies. In a body-fixed frame with axes set along the principal axes of a particle and its origin at the center of mass, the rotational motion of a rigid body follows Euler's equations

$$\begin{aligned} I_{xx}^b \dot{\omega}_x^b - \omega_y^b \omega_z^b \left(I_{yy}^b - I_{zz}^b \right) &= T_x^b, \\ I_{yy}^b \dot{\omega}_y^b - \omega_z^b \omega_x^b \left(I_{zz}^b - I_{xx}^b \right) &= T_y^b, \\ I_{zz}^b \dot{\omega}_z^b - \omega_x^b \omega_y^b \left(I_{xx}^b - I_{yy}^b \right) &= T_z^b, \end{aligned} \tag{2.7}$$

where the dot denotes time derivative and I, T and ω are components of principal moment of inertia $\mathbf{I}$, principal torque $\vec{T}$ and principal angular velocity $\vec{\omega}$, respectively. The superscript letter "b" indicates the body-fixed frame and the subscript letters indicate the direction in the frame.

Regarding the position of points in a particle, body orientation in a laboratory frame relative to the body frame can be expressed by three Euler angles (α, β, γ) in the laboratory frame. By using the rotation matrix

$$\mathbf{R} = \begin{pmatrix} \cos\alpha\cos\gamma - \sin\alpha\cos\beta\sin\gamma & \sin\alpha\cos\gamma + \cos\alpha\cos\beta\sin\gamma & \sin\beta\sin\gamma \\ -\cos\alpha\sin\gamma - \sin\alpha\cos\beta\cos\gamma & -\sin\alpha\sin\gamma + \cos\alpha\cos\beta\cos\gamma & \sin\beta\cos\gamma \\ \sin\alpha\sin\beta & -\cos\alpha\sin\beta & \cos\beta \end{pmatrix}, \tag{2.8}$$

the relation between position vectors in laboratory and body frames in expressed by

$$\vec{e} = \mathbf{R}^{\intercal} \cdot \vec{e}^{\,b} + \vec{r}, \tag{2.9}$$

where $\vec{e}$ and $\vec{e}^{\,b}$ denote the position of a point in the laboratory and body-fixed frames, respectively, while $\vec{r}$ is the position vector of the center of mass in the laboratory frame. Furthermore, the following relation stands between Euler angles (α, β, γ) in the laboratory frame and principal angular velocities:

$$\begin{aligned} \omega_x^b &= \dot{\alpha}\sin\beta\sin\gamma + \dot{\beta}\cos\gamma, \\ \omega_y^b &= \dot{\alpha}\sin\beta\sin\gamma - \dot{\beta}\cos\gamma, \\ \omega_z^b &= \dot{\alpha}\cos\beta + \dot{\gamma}. \end{aligned} \tag{2.10}$$

The solution of Equation 2.10 for $(\dot{\alpha}, \dot{\beta}, \dot{\gamma})$ is

$$\begin{aligned} \dot{\alpha} &= \frac{1}{\sin\beta}\left(\omega_x^b\sin\gamma + \omega_y^b\cos\gamma\right), \\ \dot{\beta} &= \omega_x^b\cos\gamma - \omega_y^b\sin\gamma, \\ \dot{\gamma} &= \omega_z^b - \frac{\cos\beta}{\sin\beta}\left(\omega_x^b\sin\gamma + \omega_y^b\cos\gamma\right). \end{aligned} \tag{2.11}$$

However, it is clear from Equation 2.11, that $\dot{\alpha}$ and $\dot{\gamma}$ become singular for $\beta = 0$. To avoid this singularity, quaternion $\vec{q} = (q_0, q_1, q_2, q_3)^{\intercal}$ has been used instead to express the body orientation:

$$\begin{aligned} q_0 &= \sin\frac{\beta}{2}\sin\frac{\gamma-\alpha}{2}, \\ q_1 &= \sin\frac{\beta}{2}\cos\frac{\gamma-\alpha}{2}, \\ q_2 &= \cos\frac{\beta}{2}\sin\frac{\gamma+\alpha}{2}, \\ q_3 &= \cos\frac{\beta}{2}\cos\frac{\gamma+\alpha}{2}. \end{aligned} \tag{2.12}$$

To compensate for an extra degree of freedom, the following constraint must also be in place as

$$|\vec{q}| = q_0^2 + q_1^2 + q_2^2 + q_3^2 = 1. \tag{2.13}$$

Rotation matrix in Equation 2.8 can now be written as

$$\mathbf{R} = \begin{pmatrix} -q_0^2 + q_1^2 - q_2^2 + q_3^2 & 2\left(q_2 q_3 - q_0 q_1\right) & 2\left(q_1 q_2 - q_0 q_3\right) \\ 2\left(q_1 q_2 - q_0 q_3\right) & q_0^2 - q_1^2 - q_2^2 + q_3^2 & 2\left(q_1 q_3 - q_0 q_2\right) \\ 2\left(q_1 q_2 - q_0 q_3\right) & -2\left(q_0 q_1 - q_2 q_3\right) & -q_0^2 - q_1^2 + q_2^2 + q_3^2 \end{pmatrix}. \tag{2.14}$$

By introducing the following matrix $\mathbf{Q}$

$$\mathbf{Q} = \frac{1}{2} \begin{pmatrix} -q_2 & -q_3 & q_1 \\ q_3 & -q_2 & -q_0 \\ q_0 & q_1 & q_3 \\ -q_1 & q_0 & -q_2 \end{pmatrix}, \tag{2.15}$$

Equation 2.11 is equivalently written as

$$\dot{\vec{q}} = \frac{1}{2} \mathbf{Q} \cdot \vec{\omega}^b, \tag{2.16}$$

without any singularity. There is also an additional benefit of eliminating trigonometric functions.

2.2 Potential Functions

In this research, SPC/E[36] potential model is used for water molecules and OPLS-UA[37,38] potential model is used for methanol and IPA molecules. Both models cover intermolecular interactions and OPLS-UA additionally has intramolecular potentials to represent internal rotations. All molecular models are represented as a group of interaction sites and treated as rigid bodies. An interaction site can be a point charge subject to Coulomb interaction as well as van der Waals interaction expressed by Lennard-Jones (L-J) potential.

Coulomb potential between two interaction sites i and j with a distance r_{ij} is as follows

$$\Phi_{\mathrm{C}}^{ij} = \frac{q_i q_j}{4\pi\varepsilon_0}\frac{1}{r_{ij}}, \tag{2.17}$$

where ε_0 denotes vacuum permittivity and q_i and q_j are the charges of sites i and j. In the case of L-J, the potential between two interaction sites is

$$\Phi_{\mathrm{LJ}}^{ij} = 4\varepsilon_{ij}\left\{\left(\frac{\sigma_{ij}}{r_{ij}}\right)^{12} - \left(\frac{\sigma_{ij}}{r_{ij}}\right)^{6}\right\}, \tag{2.18}$$

where σ_{ij} and ε_{ij} are the distance at which inter-site potential becomes zero and the potential well depth, respectively. Values for the interaction sites are provided later in this chapter, while those between different sites are given by the Lorentz-Berthelot mixing rules as

$$\begin{aligned}\sigma_{ab} &= \frac{\sigma_a + \sigma_b}{2},\\ \varepsilon_{ab} &= \sqrt{\varepsilon_a \varepsilon_b}.\end{aligned} \tag{2.19}$$

While these mixing rules are simple and widely used, they are very general and cannot accurately reproduce mixture properties that are observed experimentally, although the general tendencies are retained and that is deemed enough for this work. In case of only rigid bodies, the whole potential of a system is simply the sum of L-J and Coulomb potentials over every combination of N particles with $n_l\,(l = 1, \cdots, N)$ interaction sites for each particle and without intra-combination:

$$\Phi = \frac{1}{2}\sum_{l=1}^{N}\sum_{\substack{m=1\\ m\neq l}}^{N}\sum_{i=1}^{n_l}\sum_{j=1}^{n_m}\left(\Phi_{\mathrm{LJ}}^{l,i\ m,j} + \Phi_{\mathrm{C}}^{l,i\ m,j}\right). \tag{2.20}$$

2.2.1 Water model

The extended simple point charge model, SPC/E[36] for water (H_2O) molecule, is a rigid isosceles triangle, with charges on each of the three atoms, shown in Fig. 2.1. The bond

length of both O–H bonds is 0.1 nm, with a bond angle of 109.47 degrees. In addition to Coulomb interactions due to the charges, van der Waals interactions are implemented by an L-J site, situated on the oxygen atom. Coulomb, L-J and mass parameters are shown in Table 2.1.

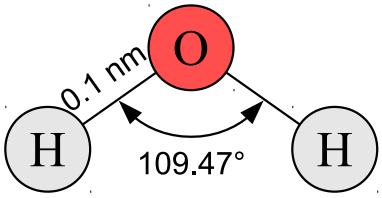

Figure 2.1: SPC/E water model.

Table 2.1: Potential and mass parameters of SPC/E water model.

σ_O (nm)	ε_O (nm)	q_O (e)	m_O (kg)
0.3166	1.079×10^{-21}	-0.8476	2.658×10^{-26}
σ_H (nm)	ε_H (nm)	q_H (e)	m_H (kg)
-	-	0.4238	1.674×10^{-27}

2.2.2 Alcohol model

The optimized potentials for liquid simulations (OPLS) force field was developed for the simulation of organic liquids, which reproduce many bulk properties at room temperature. In this research, OPLS-UA (united atom) flavor of the model is used. In the united atom version, carbon atoms and any neighboring hydrogen atoms are treated as a single interaction site, thus saving computing time. Geometric parameters, i.e. bond lengths and angles between bonds, are provided based on neighboring atoms.

Based on OPLS-UA, models for methanol (CH_3OH) and isopropyl alcohol (IPA, $(CH_3)_2CHOH$) are created. Methanol has no internal degrees of freedom as shown in Fig. 2.2 and can be handled as a rigid body. In the case of IPA however, according to the original model shown in Fig. 2.3 there is one rotational degree of freedom around the CH–O bond, and a rotational potential is given in the original paper.[38] There exist three distinct conformers at local minimums of the rotational potential as shown in Fig. 2.4. Instead of handling rotation and intramolecular interaction, a simplified IPA model is created as a mixture of three rigid conformer molecules with the approximate mixing ratios taken from the original reference.[38] Intermolecular potential and mass parameters for methanol and IPA are shown in Tables 2.2 and 2.3.

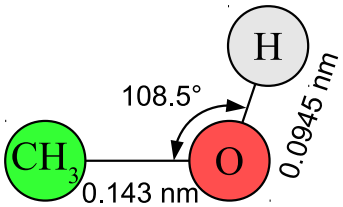

Figure 2.2: OPLS-UA methanol model.[37,38]

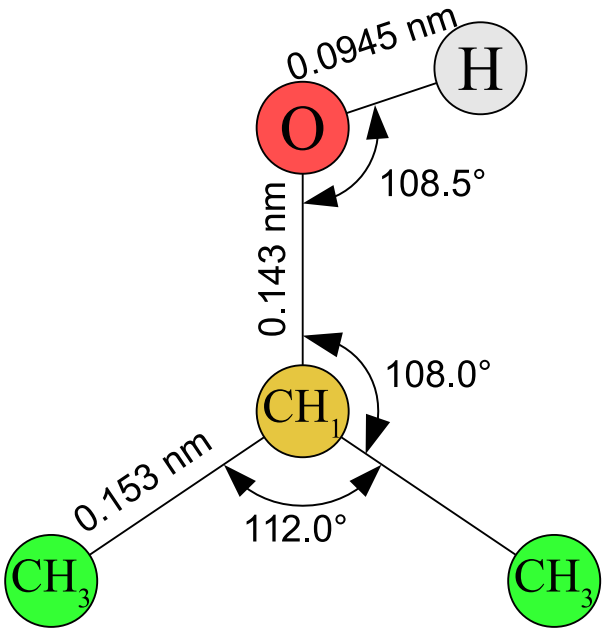

Figure 2.3: Original OPLS-UA model of IPA.[37,38]

(a) Two gauche conformers (b) Trans conformer

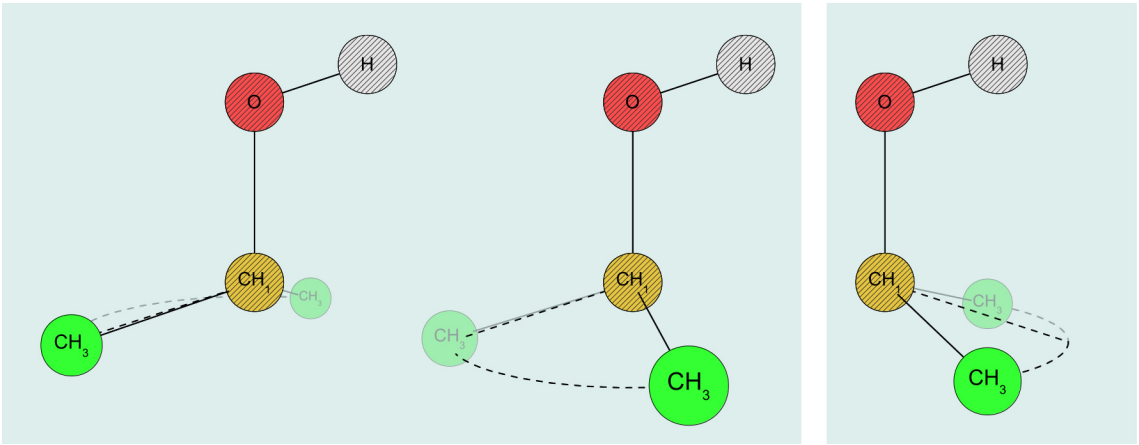

Figure 2.4: Three conformers of the IPA molecule.

Table 2.2: Potential and mass parameters of OPLS-UA methanol.

σ_{O} (nm)	ε_{O} (J)	q_{O} (e)	m_{O} (kg)
0.307	1.181×10^{-21}	-0.7	2.658×10^{-26}
$\sigma_{\mathrm{CH_3}}$ (nm)	$\varepsilon_{\mathrm{CH_3}}$ (J)	$q_{\mathrm{CH_3}}$ (e)	$m_{\mathrm{CH_3}}$ (kg)
0.377	1.438×10^{-21}	0.265	2.497×10^{-26}
σ_{H} (nm)	ε_{H} (J)	q_{H} (e)	m_{H} (kg)
-	-	0.435	1.674×10^{-27}

Table 2.3: Potential and mass parameters of OPLS-UA model of IPA.

σ_{CH} (nm)	$\varepsilon_{\mathrm{CH}}$ (J)	q_{CH} (e)	m_{CH} (kg)
0.385	5.559×10^{-22}	0.265	2.162×10^{-26}
$\sigma_{\mathrm{CH_3}}$ (nm)	$\varepsilon_{\mathrm{CH_3}}$ (J)	$q_{\mathrm{CH_3}}$ (e)	$m_{\mathrm{CH_3}}$ (kg)
0.391	1.112×10^{-21}	0.0	2.497×10^{-26}
σ_{O} (nm)	ε_{O} (J)	q_{O} (e)	m_{O} (kg)
0.307	1.181×10^{-21}	-0.7	2.657×10^{-26}
σ_{H} (nm)	ε_{H} (J)	q_{H} (e)	m_{H} (kg)
-	-	0.435	1.674×10^{-27}

2.2.3 Solid surface potential

Solid surface is made up of three layers of atoms creating an fcc (111) surface. Each atom is assumed as a site that has no Coulomb interaction and interacts with only non-surface particles. The interaction between surface atoms is expressed by a harmonic potential for nearest neighbors

$$\Phi_{\mathrm{H}}(r_{ij}) = \frac{k}{2}\left(r_{ij} - r_0\right)^2, \tag{2.21}$$

where k and r_0 are the spring constant and equilibrium distance of nearest neighboring particles, respectively. Values of platinum crystal are adopted for the mass, lattice constant, Young's modulus and van der Waals radius, from which r_0, σ_{wall} and k are derived, and the L-J potential parameter $\varepsilon_{\mathrm{wall}}$ is empirically set to provide an approximate contact angle of 90 degrees for SPC/E water droplets. The potential and mass parameter are shown in Table 2.4.

Table 2.4: Potential and mass parameters of solid surface.

σ_{wall} (nm)	$\varepsilon_{\mathrm{wall}}$ (J)	q_{wall} (e)	m_{wall} (kg)	k (N/m)	r_0 (nm)
0.35	1.447×10^{-21}	0	3.239×10^{-25}	46.8	0.277

2.2.4 Potential wall

A one-dimensional wall potential is also created to mimic the mean potential field of a single layer of the solid surface described in the previous section. This is done by assuming the solid surface atoms to be distributed uniformly inside a layer and integrating Equation 2.18 over the whole area to produce the gross potential

$$\Phi_{\mathrm{W}}(d) = \int_0^\infty \rho_{\mathrm{W}} \Phi_{\mathrm{LJ}}(R)\, 2\pi r \mathrm{d}r, \tag{2.22}$$

where ρ_{W} denotes the area number density of the surface particles, and other variables are illustrated in Fig. 2.5. Integrating Equation 2.22 produces

$$\Phi_{\mathrm{W}}(d_{ij}) = 2\pi\varepsilon_{ij}\rho_{\mathrm{W}} \left\{ \frac{2}{5} \left(\frac{\sigma_{ij}}{d_{ij}} \right)^{12} - \left(\frac{\sigma_{ij}}{d_{ij}} \right)^{6} \right\} d_{ij}^2, \tag{2.23}$$

where d_{ij} denotes the distance between site i and plane j. The surface particle density ρ_{W} depends on the crystal orientation and lattice spacing, and for fcc (111) is $\frac{2}{\sqrt{3}r_0^2}$ The same L-J parameters are used as for the solid surface shown in Table 2.4. By placing three potential walls with $\sqrt{\frac{2}{3}}r_0$ interval, one-dimensional solid surface potential field is reproduced. These walls only interact with fluid particles.

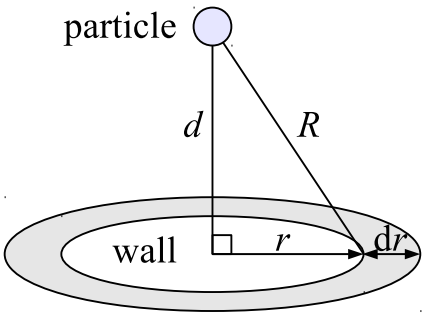

Figure 2.5: Integration for obtaining one-dimensional wall potential.

2.3 Temperature

Water, methanol and IPA molecules in this study are rigid bodies whose motion can be separated into translational and rotational motions. Except for molecules with a linear structure, rigid molecules have 3 degrees of freedom for translational motion and 3 degrees of freedom for rotational motion, making 6 degrees of freedom in total.

The kinetic energy of a system composed of rigid molecules can be divided into translational and rotational components

$$E = E_t + E_r. \tag{2.24}$$

In case of N rigid molecules, letting $\vec{v}$ be the relative velocity to the system's center of mass, the internal kinetic energy E_t coming from the translational motion is

$$E_t = \frac{1}{2}\sum_{i=1}^{N} m_i \vec{v}_i \cdot \vec{v}_i, \tag{2.25}$$

and the internal kinetic energy E_r coming from the rotational motion is

$$E_r = \frac{1}{2}\sum_{i=1}^{N} \left(\mathbf{I}_i^b \cdot \vec{\omega}_i^b\right) \cdot \vec{\omega}_i^b. \tag{2.26}$$

From this, the system temperature can be defined by

$$T = \frac{2}{k_b N_f} E = \frac{2}{k_b N_f} \left(E_t + E_r\right), \tag{2.27}$$

where k_b is the Boltzmann constant and N_f is the number of degrees of freedom that is equal to $6N - 3$ in a system without stationary frame of reference.

2.3.1 Simple velocity scaling

The velocity scaling method is the simplest way of temperature control, suitable only when the energy flux as well as a precise description of the system are not important. In this method, for a desired control temperature T_{set} velocities of all molecules are simultaneously scaled by a same factor

$$\lambda_{\text{set}} = \sqrt{\frac{T_{\text{set}}}{T}}. \tag{2.28}$$

For rigid bodies velocities of the centers of mass and angular velocities are modified in the following way for every molecule in the system

$$\begin{aligned} \vec{v}_i &= \vec{v}_i^{(\text{old})} \lambda_{\text{set}}, \\ \vec{\omega}_i^b &= \vec{\omega}_i^{b(\text{old})} \lambda_{\text{set}}. \end{aligned} \tag{2.29}$$

2.3.2 Stochastic velocity scaling

When direct velocity scaling is unavoidable and a precise description of a system is necessary, a stochastic velocity scaling scheme that is known to sample the NVT ensemble is used.[39] In this scheme, the particle translational velocities are scaled so that the rate of change of the kinetic energy E is expressed by a differential equation

$$\mathrm{d}E = (E_{\mathrm{set}} - E)\,\frac{\mathrm{d}t}{\tau_T} + 2\sqrt{\frac{EE_{\mathrm{set}}}{N_f}}\,\frac{\mathrm{d}W}{\sqrt{\tau_T}}, \tag{2.30}$$

where τ_T, $\mathrm{d}W$ and $E_{\mathrm{set}} = \frac{1}{2}k_b N_f T_{\mathrm{set}}$ are thermostat relaxation time, Wiener noise and control kinetic energy, respectively. When considering only the first term of the right-hand side of Equation 2.30, the solution is simply

$$E\,(t) = [E\,(0) - E_{\mathrm{set}}] \exp\left(-\frac{t}{\tau_T}\right) + E_{\mathrm{set}}, \tag{2.31}$$

where $E\,(0)$ is the initial kinetic energy. The velocity scaling ratio $\lambda_{\mathrm{set}} = \sqrt{\frac{E(h)}{E(0)}}$ after a calculation step h can be derived by using the first-order Taylor approximation

$$\lambda_{\mathrm{set}}^2 = \left(1 - \frac{E_{\mathrm{set}}}{E\,(0)}\right) \exp\left(-\frac{h}{\tau_T}\right) + \frac{E_{\mathrm{set}}}{E\,(0)} \approx 1 + \frac{h}{\tau_T}\left(\frac{T_{\mathrm{set}}}{T} - 1\right), \tag{2.32}$$

which produces the widely used Berendsen's thermostat.[40] Unfortunately Berendsen's thermostat does not produce a proper NVT ensemble. This is solved by adding random noise, as shown in Equation 2.30, and the solution is given in the original paper[39] as

$$\begin{aligned}\lambda_{\mathrm{set}}^2 = \exp\left(-\frac{h}{\tau_T}\right) + \frac{E_{\mathrm{set}}}{N_f E}\left\{1 - \exp\left(-\frac{h}{\tau_T}\right)\right\}\left(X_1^2 + \sum_{i=2}^{N_f} X_i^2\right) \\ + 2\exp\left(-\frac{h}{2\tau_T}\right)\sqrt{\frac{E_{\mathrm{set}}}{N_f E}\left\{1 - \exp\left(-\frac{h}{\tau_T}\right)\right\}}\,X_1,\end{aligned} \tag{2.33}$$

where X_i denotes an independent random number from a Gaussian distribution with unity variance. The velocity scaling ratio λ_{set} is used to scale translational and angular velocities in the same manner as described in the previous section by Equation 2.29.

2.3.3 Langevin method

For most systems with a solid surface, the Langevin method is used to maintain the surface temperature.[41] The solid atoms subject to the Langevin temperature control are considered to be attached to a heat bath and the whole system is maintained at a constant temperature. Because there is no direct tampering with liquid molecules, this is a preferred method for observing an equilibrium system at a constant temperature.

The solid surface consisting of three layers is shown Fig. 2.6. The temperature control is applied through phantom particles positioned in the second layer. Each phantom particle is connected to a damper with a damping coefficient of

$$\alpha_{\mathrm{damp}} = m\frac{\pi}{6}\frac{k_b\lambda_{\mathrm{deb}}}{\hbar}, \tag{2.34}$$

where m, λ_{deb} and $\hbar$ are the mass of solid atom, Debye temperature and reduced Planck constant, respectively. The Debye temperature is set to $\lambda_{\mathrm{deb}} = 240$ K using the value of platinum in this study and thus giving the damping coefficient $\alpha_{\mathrm{damp}} = 5.33 \times 10^{-13}$ kg/s. The damping is independently applied to the three velocity components.

In addition to this, each phantom particle is excited by a random force having Gaussian distribution with standard deviation

$$\sigma_F = \sqrt{\frac{2\alpha_{\mathrm{damp}}k_bT_{\mathrm{set}}}{h}}, \tag{2.35}$$

where h denotes the time step. When the system is at the control temperature T_{set}, the amount of energy lost through dampers and gained through random forces is exactly the same, producing a thermal equilibrium.

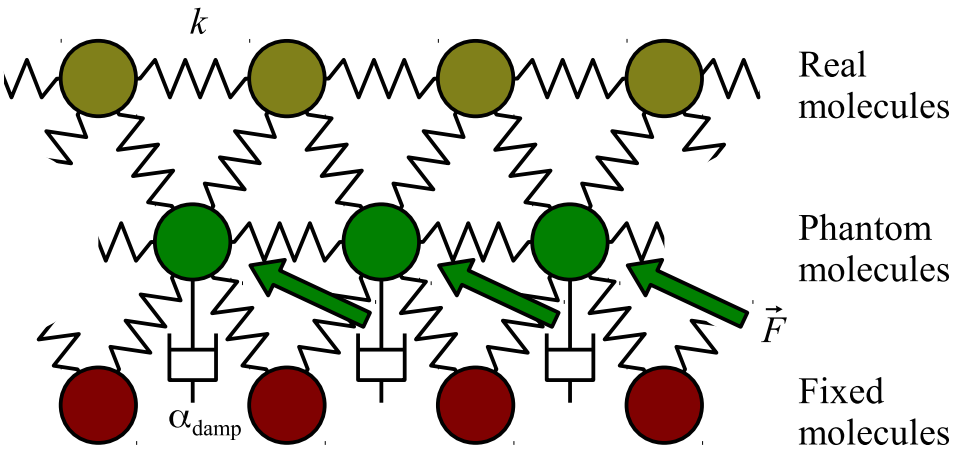

Figure 2.6: Temperature control of solid surface with Langevin method.

2.4 Pressure

Pressure is one of the most fundamental properties of liquids and gasses. However, the definition of pressure in molecular dynamics is not as straightforward as in macroscopic continuum-based fluid dynamics or thermodynamics since it is a property of the whole system, in other words, pressure does not directly work on the particles as the interatomic potential does in microscopic scale molecular dynamics. In this section, the microscopic concept of pressure is described.

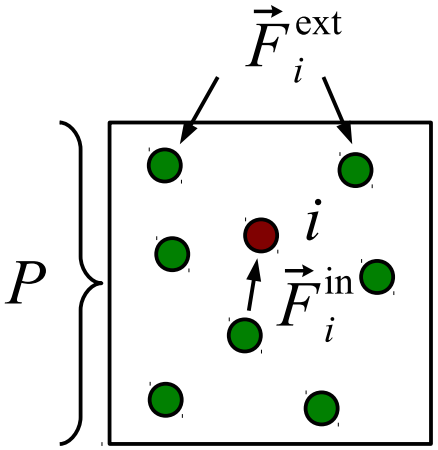

Figure 2.7: Liquid molecules inside a container.

2.4.1 System pressure

In order to define the system pressure, a container of volume V with a number of particles inside is considered as shown in Fig. 2.7. Forces working upon particle i can be separated into ones from interaction with particles inside the container and ones from the container walls

$$m_i \ddot{\vec{r}}_i = \vec{F}_i^{\text{in}} + \vec{F}_i^{\text{ext}}. \tag{2.36}$$

Take note that for molecules with several interaction sites $\vec{F}_i$ represents the net force working on the center of mass at position vector $\vec{r}_i$. The following equation is obtained by taking the inner product of $\vec{r}_i$ for both sides of Equation 2.36, summing over all

particles inside the container and taking the time average

$$\sum m_i \left\langle \vec{r}_i \cdot \ddot{\vec{r}}_i \right\rangle = \sum \left\langle \vec{r}_i \cdot \vec{F}_i^{\text{in}} \right\rangle + \sum \left\langle \vec{r}_i \cdot \vec{F}_i^{\text{ext}} \right\rangle . \tag{2.37}$$

The left side of Equation 2.37 term is transformed through a partial integration

$$\begin{aligned} m_i \left\langle \vec{r}_i \cdot \ddot{\vec{r}}_i \right\rangle &= \lim_{t\to\infty} \frac{1}{2t} m_i \int_{-t}^{t} \vec{r}_i \cdot \ddot{\vec{r}}_i \mathrm{d}\tau \\ &= \lim_{t\to\infty} \left(\frac{1}{2t} m_i \left[\vec{r}_i \cdot \dot{\vec{r}}_i \right]_{-t}^{t} - \frac{1}{2t} m_i \int_{-t}^{t} \dot{\vec{r}}_i \cdot \dot{\vec{r}}_i \mathrm{d}\tau \right) = -m_i \left\langle \dot{\vec{r}}_i \cdot \dot{\vec{r}}_i \right\rangle . \end{aligned} \tag{2.38}$$

With this, Equation 2.37 can be rewritten as

$$\sum m_i \left\langle \dot{\vec{r}}_i \cdot \dot{\vec{r}}_i \right\rangle + \sum \left\langle \vec{r}_i \cdot \vec{F}_i^{\text{in}} \right\rangle = -\sum \left\langle \vec{r}_i \cdot \vec{F}_i^{\text{ext}} \right\rangle . \tag{2.39}$$

The right side of Equation 2.39 is due to the outside forces from the container walls working on the particles inside. If it is assumed that the right side is a result of isotropic pressure P being applied to the surface of volume V at the container walls, it is equivalently expressed using pressure P

$$-\sum \left\langle \vec{r}_i \cdot \vec{F}_i^{\text{ext}} \right\rangle = -\iint \vec{r} \cdot (-P\vec{n}) \, \mathrm{d}A = P \iint \vec{r} \cdot \vec{n} \mathrm{d}A. \tag{2.40}$$

Take note that $\vec{n}$ is outward unit normal vector of the surface volume V. By using the divergence theorem, Equation 2.40 becomes

$$-\sum \left\langle \vec{r}_i \cdot \vec{F}_i^{\text{ext}} \right\rangle = P \iint \vec{r} \cdot \vec{n} \mathrm{d}A = P \iiint \nabla \vec{r} \mathrm{d}V = 3PV. \tag{2.41}$$

By substituting the right side of Equation 2.39 with Equation 2.41, the system pressure is expressed by velocity and interactive forces as

$$P = \frac{1}{3V} \sum m_i \left\langle \vec{v}_i \cdot \vec{v}_i \right\rangle + \frac{1}{3V} \left\langle \vec{r}_i \cdot \vec{F}_i^{\text{in}} \right\rangle . \tag{2.42}$$

This is the so-called virial pressure. Because all interactions can be expressed as symmetric site-site interactions in this study, the force component can be rewritten in the following more convenient form

$$P = \frac{1}{3V} \sum m_i \left\langle \vec{v}_i \cdot \vec{v}_i \right\rangle + \frac{1}{3V} \sum_i \sum_{j(>i)} \left\langle \vec{r}_{ij} \cdot \vec{F}_{ij} \right\rangle . \tag{2.43}$$

Take note that $\vec{r}_{ij} = \vec{r}_i - \vec{r}_j$ and $\vec{F}_{ij}$ is force acting on particle i due to interaction with particle j. Through similar procedure the pressure tensor can also be derived that results in the following equation

$$P^{\alpha\beta} = \frac{1}{V} \sum m_i \left\langle v_i^{\alpha} v_i^{\beta} \right\rangle + \frac{1}{V} \sum_{i<j} \left\langle r_{ij}^{\alpha} F_{ij}^{\beta} \right\rangle . \tag{2.44}$$

Note that the following relation holds between isotropic pressure and the diagonal components of the pressure tensor

$$P = \frac{1}{3}\sum_{\alpha=1}^{3} P^{\alpha\alpha}. \tag{2.45}$$

Up to here, a closed container with particles inside was assumed. During our calculations where system pressure is needed, periodic boundary conditions are imposed upon the system. Surprisingly, system pressure tensor is correctly provided by the same Equation 2.44 even though explicit external forces no longer exit. Instead, "external" pressure is considered to come from inter-molecular interactions that cross the periodic boundaries.[42]

2.4.2 Local pressure

To investigate interfaces and calculate their surface tensions, a way to calculate local pressure tensor is needed. In this work, the system is divided into several slabs as shown in Fig. 2.8. The aim is to find the pressure tensor in each slab. In Equation 2.44, it is clear that the calculation of the velocity component is very simple: only the velocity of particles inside the slab needs to be considered. On the other hand, it is not as straightforward for the force component because the force vector $\vec{F}_{ij}$ may pass over multiple slabs. This inconvenience can be compensated by redefining the force component in Equation 2.44. Firstly the z-direction pressure applied onto the surface perpendicular to the z-axis is investigated. According to the Irving-Kirkwood convention,[43] if the line between the centers of mass of two particles crosses a surface element, then the intermolecular force between the two particles contributes to the pressure of the surface element by the force component of $\vec{F}_{ij}$ perpendicular to the surface. From this, an equation can be derived: consider a surface element with an area A^z_{sl}, the pressure contribution P^z_A from intermolecular force $\vec{F}_{ij}$ acting on particle i due to particle j passing through the surface element is determined by

$$P^z_A = \frac{1}{A^z_{sl}}\sum_i \sum_{j(>i)} \vec{F}_{ij}\cdot\vec{n}^z \frac{r^z_{ij}}{\left|r^z_{ij}\right|} = \frac{1}{A}\sum_i \sum_{j(>i)} F^z_{ij}\frac{r^z_{ij}}{\left|r^z_{ij}\right|}, \tag{2.46}$$

where $\vec{n}^z$ is the unit vector to $+z$-direction, and F^z_{ij} and $\vec{r}^z_{ij}$ denote z-components of force vector F_{ij} from j to i and relative position vector r_{ij}, respectively. Through multiplying by $\frac{r^z_{ij}}{|r^z_{ij}|}$ not only the absolute value of the perpendicular force is gained, but repulsive and attractive forces are also distinguished in Equation 2.46, i.e. these forces respectively correspond to positive and negative pressures exerted onto the surface

area. Force is assumed to uniformly act on a straight line. Therefore the contribution of particle interaction to pressure can be defined by averaging over all surface areas contained in a slab k

$$P_k^z = \frac{1}{L_{sl}} \int_{\text{slab } k} P_A^z \mathrm{d}z = \frac{1}{V_{sl}} \sum_i \sum_{j(>i)} \int_{\text{slab } k} F_{ij}^z \frac{r_{ij}^z}{\left|r_{ij}^z\right|} \mathrm{d}z = \frac{1}{V_{sl}} \sum_i \sum_{j(>i)} F_{ij}^z r_{ij}^z \frac{L_{k,ij}^z}{\left|r_{ij}^z\right|}, \tag{2.47}$$

where V_{sl} and L_{sl}^z are the volume and height of the slab in the z-direction, respectively, while $L_{k,ij}^z$ is the z-component length of the part of the relative vector r_{ij} in slab k. Since the force is constant along the line connecting the two particles, the integration in Equation 2.47 is solved as a simple product. For example in Fig. 2.8, $L_{3,ij}^z$ is L_{sl}^z and $L_{1,ij}^z$ is L_1^z. In case both particles are in the same slab it is simply $\left|r_{ij}^z\right|$ and pressure contribution exactly matches the one defined in the previous section. By applying a similar procedure to other directions, the pressure tensor in slab k is derived as follows

$$P_k^{\alpha\beta} = \frac{1}{V_{sl}} \sum_{i \in \text{slab } k}^{N} m_i \left\langle v_i^\alpha v_i^\beta \right\rangle + \frac{1}{V_{sl}} \sum_{i<j}^{N} \left\langle r_{ij}^\alpha F_{ij}^\beta \frac{L_{k,ij}^z}{\left|r_{ij}^z\right|} \right\rangle, \tag{2.48}$$

which is an equations widely used to calculate local pressure in slabs.[44] To be specific, the weighting function $\frac{L_{k,ij}^z}{\left|r_{ij}^z\right|}$ is only valid for a system divided into slabs due to triangle similarity. In general, the weighting function is the fraction of a particle-joining line that lies within the volume of interest.

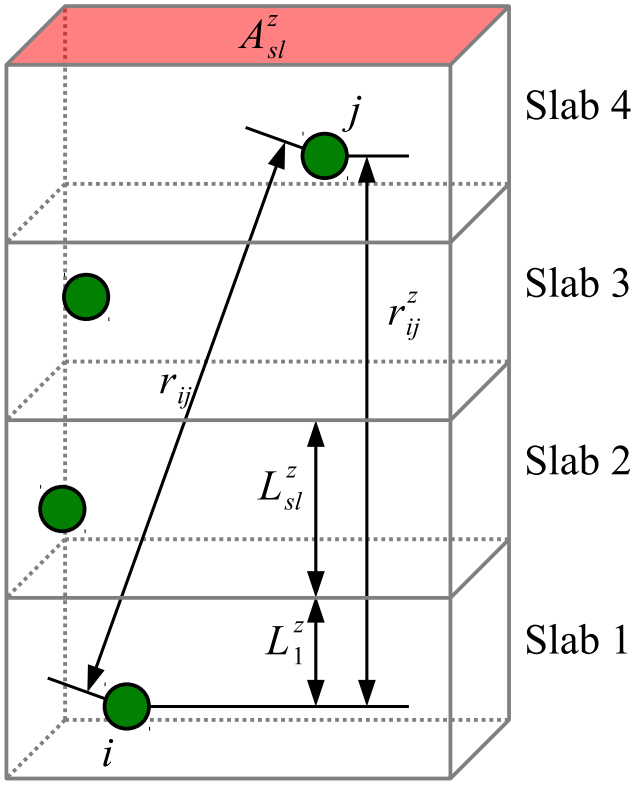

Figure 2.8: Example of pressure through slabs.

2.4.3 Pressure control

The pressure control scheme proposed by Bussi et al.[45] is used when there is a need to keep the system pressure constant and create an NPT ensemble. The calculation cell volume becomes a variable with its own equation of motion

$$\dot{V} = 3V\eta, \tag{2.49}$$

where η is proportional to the relative change rate of the volume. The difference between the actual system pressure P and the control pressure P_{set} influences this change rate

$$\dot{\eta} = 3\frac{V\left(P - P_{\text{set}}\right) + 2k_bT_{\text{set}}}{W}, \tag{2.50}$$

where W is the so called "inertia of the piston", which determines how sensitive the volume change is to the system pressure. In accordance to the original paper, this is defined as

$$W = N_f k_b T_{\text{set}} \tau_P^2, \tag{2.51}$$

where τ_P is the barostat relaxation time.[45] The equation of motion for translational motion shown in Equation 2.4 is also modified by

$$\dot{\vec{r}}_i = \vec{v}_i + \eta\vec{r}_i, \tag{2.52}$$

$$\dot{\vec{v}}_i = \frac{\vec{F}_i}{m_i} - \eta\vec{v}_i, \tag{2.53}$$

and this shows that the rate of change in position is no longer equal to the particle velocity. Take note that although equations of motion have changed, the derivations in Sections 2.4.1 and 2.4.2 are still valid, and Equation 2.43 is used to calculate system pressure. Additionally, this scheme is only valid when using positions and velocities relative to that of system's center of mass, and the equation of motion responsible for rotational motion is left unchanged. In a system governed by these equations of motion, the intermolecular energy is no longer conserved, and instead a new quantity is defined by

$$H = E + \Phi - 2k_bT_{\text{set}}\log\frac{V}{V_0} + PV + \frac{W\eta^2}{2} = H_0, \tag{2.54}$$

where V_0 and H_0 are the initial values of system volume and the conservation quantity. This conservation quantity is almost equivalent to the enthalpy of the systems $(E + \Phi + PV)$, thus dubbed "effective enthalpy", and is a time invariant

$$\frac{\mathrm{d}H}{\mathrm{d}t} = \sum\frac{\partial H}{\partial\vec{r}_i}\cdot\dot{\vec{r}}_i + \sum\frac{\partial H}{\partial\vec{v}_i}\cdot\dot{\vec{v}}_i + \frac{\partial H}{\partial V}\dot{V} + \frac{\partial H}{\partial\eta}\dot{\eta} = 0. \tag{2.55}$$

This method is devised to control the pressure of a bulk system, and each dimension of the calculation cell is scaled by $\sqrt[3]{\frac{V}{V_0}}$ to fulfil system volume's equation of motion. The described equations of motions do not strictly produce an NPH ensemble, as the effective enthalpy slightly deviates from the real enthalpy. This is of no concern however, as stochastic velocity scaling described in Section 2.3.2 is used in conjunction to produce a correct NPT ensemble. Because system volume has become a variable, the system degrees of freedom N_f are increased by one and $\frac{W\eta^2}{2}$ is added to the kinetic energy in Equation 2.24, while η is scaled by the same coefficient as velocities in Equation 2.33.

2.4.4 Local one-dimensional pressure control

The pressure control method described previously is modified to provide one-dimensional pressure control inside a local region while still preserving the conservation of effective enthalpy H. The basic concept is shown in Fig. 2.9 and the equation of motion is modified in the following way

$$\dot{r}_i^\alpha = v_i^\alpha + \eta \left[r_i^\alpha - \mathrm{sgn}\left(r_i^\alpha\right) \cdot l_{\mathrm{ctrl}}^\alpha \right], \tag{2.56}$$

$$\dot{v}_i^\alpha = \frac{F_i^\alpha}{m_i} - \eta v_i^\alpha, \tag{2.57}$$

$$\dot{\eta} = \frac{V_{\mathrm{ctrl}} \left(P_{\mathrm{ctrl}}^\alpha - P_{\mathrm{set}}\right) + 2k_b T_{\mathrm{set}}}{W}, \tag{2.58}$$

$$\dot{V}_{\mathrm{ctrl}} = \eta V_{\mathrm{ctrl}}. \tag{2.59}$$

A sign function is used together with the starting position l_{ctrl}^α of the pressure control region to account for the system symmetry. Equations 2.56 and 2.57 are only applied in the pressure control direction of particles inside the control region, and classical Newtonian equation of motion is used otherwise. The pressure control region is treated as a single slab and the α component of the local pressure P_{ctrl}^α is calculated as described in Section 2.4.2. This provides a system where there is only direct pressure control on the outermost regions, while the effective enthalpy H is still conserved in its unmodified form.

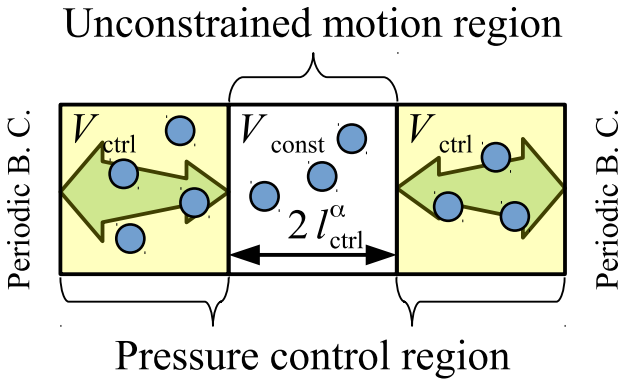

Figure 2.9: The concept of a system with one-dimensional pressure control confined to a local region. Particles in the middle white region follow the classical Newtonian equation of motion, while particles in the yellow side region move according to the modified equation of motion. The horizontal dimension of the white region is $2l^{\alpha}_{\mathrm{ctrl}}$ and its volume is constant, while the horizontal dimension of the yellow region, and thus its volume V_{ctrl}, vary according to its equation of motion. Periodic boundary conditions are set in all lateral directions.
*Reprinted with permission from "D. Surblys, Y. Yamaguchi, K. Kuroda, M. Kagawa, T. Nakajima and H. Fujimura, The Journal of Chemical Physics, 140, 034505 (2014)". Copyright 2014, American Institute of Physics.

2.5 Interfacial Tension

Surface tension is generally known as the force working along liquid-vapor interface that is responsible for a number of phenomena including the spherical shape of droplets and capillary effect. Surface tension is defined as the force along a line of unit length, where the force is parallel to the surface and perpendicular to the line. Surface tension also has a dimension of energy per unit area. The same kind of definition is also used for interfaces such as solid-vapor, solid-liquid or between different liquids.

2.5.1 Bakker's equation

In macro-scale, the pressure tensor components of a static liquid bulk satisfy the following:

$$P = P^{xx} = P^{yy} = P^{zz}, \tag{2.60}$$

$$P^{xy} = P^{yz} = P^{zx} = 0. \tag{2.61}$$

However, it is not the case for a flat interface. Consider an interface that is perpendicular to the z-axis as shown in Fig. 2.10. Because of symmetric properties and static condition, the non-diagonal components are still all equal to zero as in Equation 2.61. However, P^{zz} is no longer equal to P^{xx} and P^{yy} due to the interface and surface tension force which only acts parallel to the surface, although P^{xx} is still equal to P^{yy}. Here the three diagonal components are rewritten using normal and tangential pressures P^N and P^T:

$$P^{zz} = P^N, \tag{2.62}$$

$$P^{xx} = P^{yy} = P^T. \tag{2.63}$$

Because surface tension only works along the interface and the system is in static equilibrium, the only force working along the z-direction is the static pressure. Therefore, normal pressure $P^{zz} = P^N$ at the interface is the same as the static pressure P in the bulk

$$P^N = P, \tag{2.64}$$

and considering the force balance in z-direction, P^N is constant in the whole system.

Consider a surface area perpendicular to the x-axis with unit width in the y-direction and its height equal to l with the height range $\left[-\frac{l}{2}, \frac{l}{2}\right]$ in the z-direction which completely covers the interface thickness of this surface area as shown in Fig. 2.11. The stress acting perpendicular to the side is given by integrating tangential pressure over the area as $-\int_{-\frac{l}{2}}^{\frac{l}{2}} P^T \mathrm{d}z$. If no interface exists, the total stress is simply equal to $-lP$,

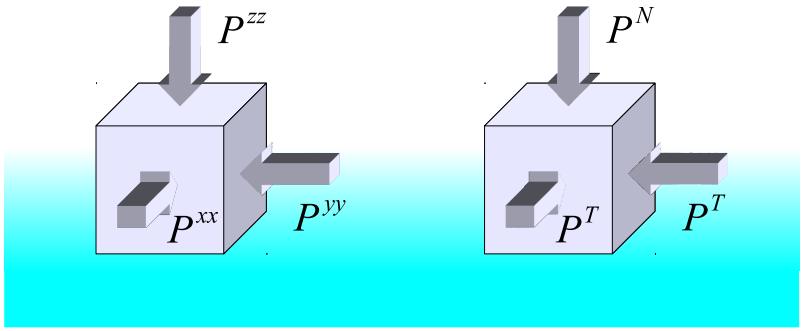

Figure 2.10: Illustration of normal and tangential pressures.

however with an interface, the surface is "pulled" by the surface tension, i.e. positive stress is additionally applied. Following the mechanical definition used by Kirkwood and Buff,[18] surface tension is the excess of stress due to the interface. Hence, because the surface area is of unit width, the surface tension can be obtained by

$$\gamma^{lv} = -\int_{-\frac{l}{2}}^{\frac{l}{2}} P^T \mathrm{d}z + lP = \int_{-\frac{l}{2}}^{\frac{l}{2}} P - P^T \mathrm{d}z. \tag{2.65}$$

Because the normal pressure P^N is constant along the z-direction, Equation 2.65 can be equivalently rewritten as

$$\gamma^{lv} = \int_{-\frac{l}{2}}^{\frac{l}{2}} P^N - P^T \mathrm{d}z. \tag{2.66}$$

Since the tangential pressure becomes equal to the bulk pressure $P = P^N = P^T$ sufficiently away from the interface, Equation 2.66 can also be written as follows in case there is only one interface in an infinite system in z-direction

$$\gamma^{lv} = \int_{-\infty}^{\infty} P^N - P^T \mathrm{d}z, \tag{2.67}$$

and this equation is known as the Bakker's equation. Because several systems in this work have more than one interface, Equation 2.66 is used exclusively.

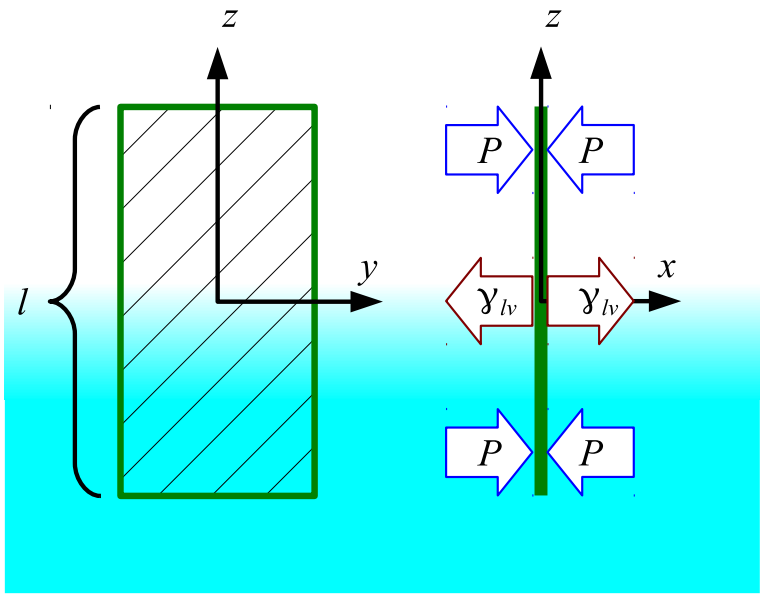

Figure 2.11: Liquid-vapor interface with a surface area stretching over it. Front view on the right and side view on the left.

2.5.2 Young-Laplace equation

The relation between droplet's internal pressure and its liquid-vapor interfacial tension is discussed in this section. Because only quasi-two-dimensional droplets are investigated in this study, this section will also be limited to two dimensions.

Consider a small two-dimensional surface area of a static droplet that is expressed by angle Θ and radius R, as shown in Fig. 2.12. This area is affected by the droplet's internal pressure P^{in}, the vapor phase's external pressure P^{out} and the liquid-vapor interfacial tension γ^{lv}. Because the droplet is static, the forces must be in balance. While force balance for the horizontal direction is obvious, the following equations can be derived to describe the force balance in the vertical direction as

$$2R\sin\left(\frac{\Theta}{2}\right)P^{\text{in}} = 2R\sin\left(\frac{\Theta}{2}\right)P^{\text{out}} + 2\gamma^{lv}\sin\left(\frac{\Theta}{2}\right). \tag{2.68}$$

This provides the Young-Laplace equation given by

$$P^{\text{in}} - P^{\text{out}} = \Delta P = \frac{\gamma^{lv}}{R}, \tag{2.69}$$

where ΔP is called "Laplace pressure". Equation 2.69 provides a relationship among pressure difference across curved surface, its surface tension and radius of curvature, showing that Laplace pressure is larger for larger interfacial tension and smaller radius of curvature.

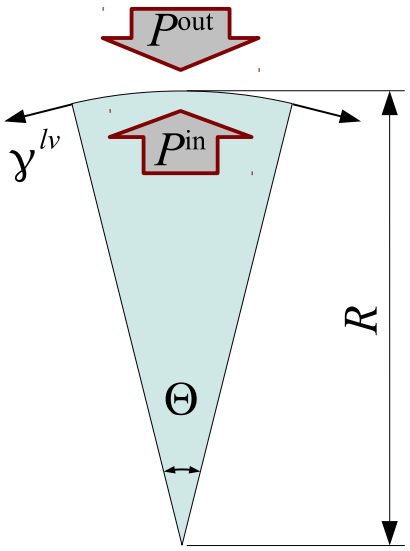

Figure 2.12: A two-dimensional minuscule surface area, with a length of ΘR.

2.5.3 Thermodynamic integration

The solid-liquid interfacial tension can also be obtained by using thermodynamic integration proposed by Leroy et al.[46] It is especially useful when Bakker's equation is not applicable. The basic premise is to use a phantom wall, for which the interfacial tension is already known, in a similar way to a piston to quasi-reversibly push the fluid away from the solid surface by moving the said phantom wall. The reversible work done by the phantom wall corresponds to the difference in Gibbs free surface energy between the solid-liquid interfaces of the walls and the thermodynamic work done to increase the system volume. For an interface between phases α and β, the relationship between Gibbs free energy per unit area $g^{\alpha\beta}$ of the interface and interfacial tension $\gamma^{\alpha\beta}$ is as follows[47]

$$\gamma^{\alpha\beta} = g^{\alpha\beta} - \sum_i \Gamma_i^{\alpha\beta}\mu_i, \tag{2.70}$$

where $\Gamma_i^{\alpha\beta}$ and μ_i are the surface excess at the interface and chemical potential for component i, respectively. For systems containing only a single-component phase there is no excess $\Gamma^{\alpha\beta} = 0$, and the Gibbs free energy of the interface and interfacial tensions become equivalent

$$\gamma^{\alpha\beta} = g^{\alpha\beta}, \tag{2.71}$$

therefore the interfacial tension difference can be readily obtained from the work done by the phantom wall.

A set of systems used for the integration in this study is shown in Fig. 2.13. Several systems with differently positioned phantom walls are created to obtain the pressure that is exerted onto the walls in a quasi-reversible process. The interfacial tension difference is thus obtained by

$$\gamma^{sl}_{\text{solid}} - \gamma^{sl}_{\text{phantom}} = -\int_{Z^0}^{Z^1} P^{\text{W}}_{\text{phantom}} \mathrm{d}Z + \frac{P}{2}\left(l_z^1 - l_z^0\right), \tag{2.72}$$

where $\gamma^{sl}_{\text{solid}}$ and $\gamma^{sl}_{\text{phantom}}$ are the solid-liquid interfacial tensions for the solid surface and phantom wall, while $P^{\text{W}}_{\text{phantom}}$ and P are the pressure exerted on the phantom walls by liquid molecules and system pressure, respectively. The distance from the center of the calculation cell to the phantom wall and the mean length of calculation cell in the horizontal direction are respectively denoted by Z and l_z, and the values of Z before and after the quasi-reversible change are Z^0 and Z^1.

This method can only be easily applied to single-component liquid systems, because as shown in Equation 2.70 the need to calculate the chemical potential arises for mixtures.

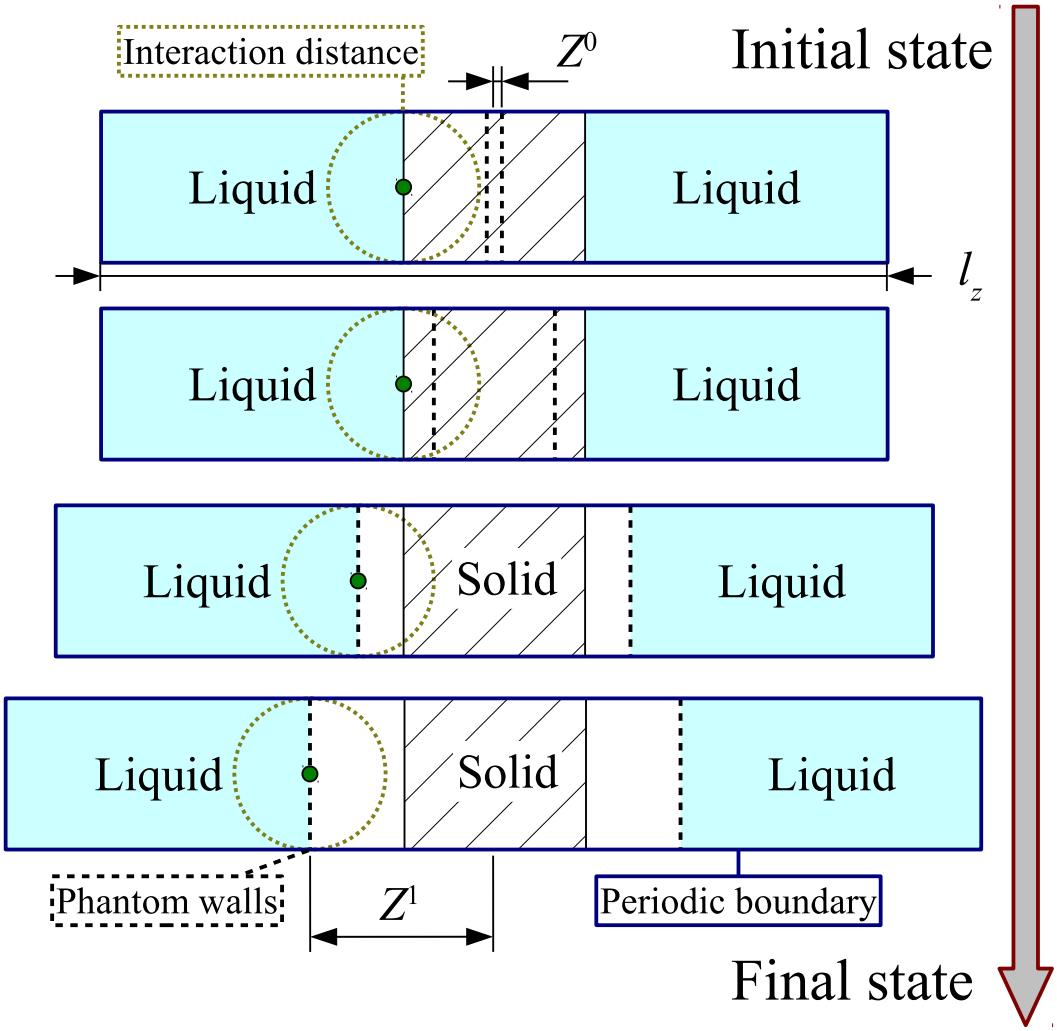

Figure 2.13: A set of systems used to calculate interfacial tension difference from thermodynamic integration. The arrow shows the integration direction. The phantom walls are initially positioned at Z^0 from the system center and out of the interaction range of the liquid phase, while in the final stage, the liquid phase is pushed to a distance of Z^1 from the system center where no solid-liquid interaction occurs. Periodic boundary is applied in all directions.

2.5.4 Young's equation and wettability

When a static macro-scale droplet is formed on a flat surface as schematically illustrated in Fig. 2.14, there are three two-phase interfaces: solid-liquid, solid-vapor and liquid-vapor. Each interface has its own surface tension per unit length that are marked here as γ^{sl}, γ^{sv} and γ^{lv}. Each interface exerts a certain force aiming to reduce its area. The area where the three-phase interface exists is called the contact line, and it is also the place where the three interfacial forces meet. Since droplet in Fig. 2.14 is in a static equilibrium, it is clear that these forces are balanced. The following equation known as Young's relation describes the balance in horizontal direction

$$\gamma^{sl} + \gamma^{lv} \cos\theta - \gamma^{sv} = 0, \tag{2.73}$$

where the angle θ is called contact angle. The smaller the contact angle is, the greater the solid-liquid interface becomes. At an angle of $\theta = 0$ liquid expands and covers as much of solid surface as possible, while at $\theta = \pi$ the droplet acquires a spherical shape and has almost no contact with the solid surface. The contact angle is a measure of wettability: solid surfaces with $\theta > \frac{\pi}{2}$ and $\theta < \frac{\pi}{2}$ are referred to as hydrophilic and hydrophobic, respectively.

In addition, it is believed that the surface provides the forces necessary to reach equilibrium for the vertical direction.

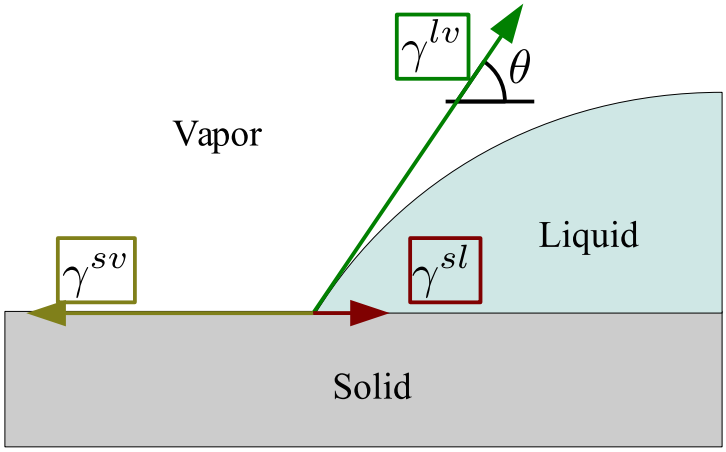

Figure 2.14: Force balance at three-phase interface line of a liquid droplet in contact with a solid surface.

2.5.5 Young's equation at the micro-scale

Strictly speaking, Fig. 2.14 does not illustrate the state of a micro-scale droplet accurately. As will be show in Chapter 3, an adsorption layer exists at the solid-liquid interface, and the contact angle at the three-phase interface is different from that of a macroscopic droplet as illustrated in Fig. 2.15. It is also difficult to define the three-phase interface as a single point since each of the interfaces has a transition layer of a finite thickness. Because of these reasons, it is no longer reasonable to consider the force balance at the three-phase interface. An alternative approach is taken as shown in Fig. 2.15, where the horizontal force balance on a control volume containing the three-phase interface in a two-dimensional droplet is considered

$$\gamma^{sl} + \gamma^{lv}\cos\theta' - \gamma^{sv} - lP^{\text{in}} + lP^{\text{out}} = 0, \tag{2.74}$$

where l and θ' are the height of the control volume and the "contact" angle between the upper boundary of the control volume and the droplet, while P^{in} and P^{out} are the droplet and vapor phase pressures, respectively. If we assume that the droplet has a constant curvature outside the control volume and the Young-Laplace Equation 2.69 can be used, the force balance is further simplified to

$$\gamma^{sl} + \gamma^{lv}\left(\cos\theta' - \frac{l}{R}\right) - \gamma^{sv} = 0, \tag{2.75}$$

where R is the radius of the droplet outside the control volume.

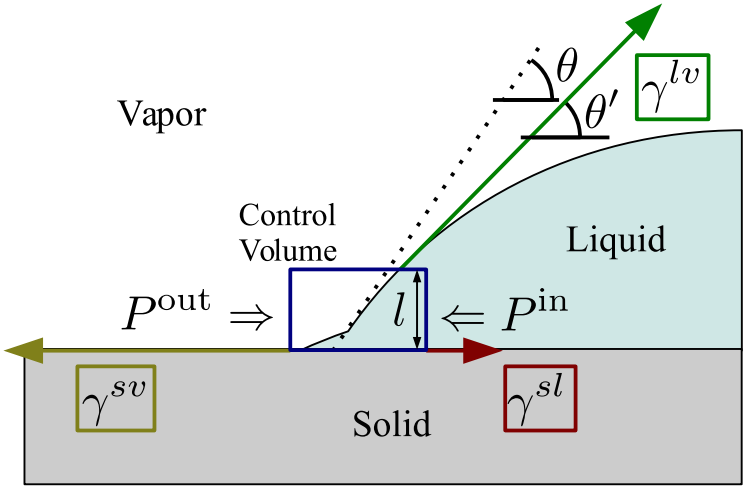

Figure 2.15: Force balance at the control volume set over the three-phase interface line.

Next, lets investigate the geometrical relation between θ and θ', where θ is the macroscopic contact angle, i.e. the contact angle if there was no adsorption layer at

the three-phase interface. Consider a circle drawn over the droplet using its radius as illustrated in Fig. 2.16. The following simple geometric relations hold

$$\begin{aligned} \cos\theta &= \frac{d}{R}, \\ \cos\theta' &= \frac{d+l}{R}, \end{aligned} \tag{2.76}$$

where d is the distance from the circle center to the solid-liquid interface. It is trivial to see that Eq. 2.75 reduces to

$$\gamma^{sl} + \gamma^{lv}\cos\theta - \gamma^{sv} = 0, \tag{2.77}$$

which is identical to Young's Equation 2.73. This shows that when applying the Young's relation to micro-scale droplets, the macroscopic contact angle, and not that of the adsorption layer, should be used.

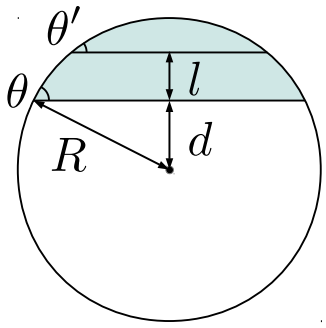

Figure 2.16: Geometric relation between the contact angles.

2.6 Force Balance at Interfaces

As will be shown in later sections, interfaces have transition layers of finite thickness, but the wetting theory described in Sections 2.5.4 and 2.5.5 uses an idealized model of interfaces with zero thickness. It is possible to define an interface position, so that the balance of force and moment due to the pressure tensor distribution become equivalent between the idealized model and the actual interface with a transition layer.[48] In accordance with the original paper, for a flat interface between two α and β phases, the equations are given as

$$\int_{-\frac{l}{2}}^{Z^{\alpha\beta}} P^{\alpha} \mathrm{d}z + \int_{Z^{\alpha\beta}}^{\frac{l}{2}} P^{\beta} \mathrm{d}z - \gamma^{\alpha\beta} = \int_{-\frac{l}{2}}^{\frac{l}{2}} P^{T} \mathrm{d}z, \tag{2.78}$$

$$\int_{-\frac{l}{2}}^{Z^{\alpha\beta}} P^{\alpha} z \mathrm{d}z + \int_{Z^{\alpha\beta}}^{\frac{l}{2}} P^{\beta} z \mathrm{d}z - Z^{\alpha\beta}\gamma^{\alpha\beta} = \int_{-\frac{l}{2}}^{\frac{l}{2}} P^{T} z \mathrm{d}z, \tag{2.79}$$

where $\gamma^{\alpha\beta}$ and $Z^{\alpha\beta}$ are the interfacial tension and the position of the interface, while P^{α} and P^{β} denote the isotropic bulk pressure in each phase. Following the assumption used in the previous Section 2.5.1 that the normal pressure P^{N} is constant along the z-direction, the isotropic bulk pressures can be replaced by P^{N}, giving

$$\gamma^{\alpha\beta} = \int_{-\frac{l}{2}}^{\frac{l}{2}} P^{N} - P^{T} \mathrm{d}z, \tag{2.80}$$

$$Z^{\alpha\beta} = \frac{1}{\gamma^{\alpha\beta}} \int_{-\frac{l}{2}}^{\frac{l}{2}} \left(P^{N} - P^{T}\right) z \mathrm{d}z, \tag{2.81}$$

where Equation 2.80 returns to Bakker's Equation 2.66 used to calculate interfacial tensions. Using Equation 2.81 it is trivial to obtain the position of the interface.

2.7 Numerical Integration

The velocity Verlet method is used for integrating both translational and rotational equations of motion. The basic premise is to calculate future position using current values, then use the newly calculated position to calculate total force at the next step, and finally use all to predict velocity.

2.7.1 Numerical integration of translational motion

In case of translational motion of a particle of mass m, using the current position of center of mass $\vec{r}(t)$, velocity $\vec{v}(t)$ and force $\vec{F}(t)$ at time t, the position of the center of mass $\vec{r}(t+h)$ after a time step h is obtained as

$$\vec{r}(t+h) = \vec{r}(t) + h\vec{v}(t) + \frac{h^2}{2m}\vec{F}(t)\,. \tag{2.82}$$

Using $\vec{r}(t+h)$, potential $\Phi(t+h)$ and more importantly total force $\vec{F}(t+h)$ can be computed. With this, velocity $\vec{v}(t+h)$ can also be obtained as

$$\vec{v}(t+h) = \vec{v}(t) + \frac{h}{2m}\left\{\vec{F}(t) + \vec{F}(t+h)\right\}. \tag{2.83}$$

2.7.2 Numerical integration of rotational motion

For the integration of rotational motion velocity Verlet method with modified quaternion-constraint techniques[49,50] is used in this study. The first step is to predict quaternion $\vec{q}$ after a time step h by

$$\vec{q}(t+h) = \vec{q}(t) + h\dot{\vec{q}}(t) + \frac{h^2}{2}\ddot{\vec{q}}(t) - \lambda(t)\,h^2\vec{q}(t)\,, \tag{2.84}$$

where $\dot{\vec{q}}(t)$ can be determined from the quaternion $\vec{q}(t)$ and principal angular velocity $\vec{\omega}^b(t)$ via Equation 2.16. The second derivative $\ddot{\vec{q}}(t)$ is obtained from the following relation through the time derivative of Equation 2.16 as

$$\ddot{\vec{q}} = \frac{1}{2}\mathbf{Q}\dot{\vec{\omega}}^b - \vec{q}\left(\dot{\vec{q}}^{\mathrm{T}}\dot{\vec{q}}\right). \tag{2.85}$$

The principal angular acceleration $\dot{\vec{\omega}}^b$ is obtained by solving Equations 2.7. The last term in Equation 2.84 is a constraint force that works to fulfill constraint in Equation 2.13. By adding this constraint force, uncertainty that arises from numerical solution is reduced. The coefficient λ is derived from the constraint in Equation 2.13 as

$$\lambda h^2 = 1 - \frac{h^2}{2}\dot{\vec{q}}\cdot\dot{\vec{q}} - \sqrt{1 - h^2\dot{\vec{q}}\cdot\dot{\vec{q}} - h^3\dot{\vec{q}}\cdot\ddot{\vec{q}} - \frac{h^4}{4}\left\{\ddot{\vec{q}}\cdot\ddot{\vec{q}} - \left(\dot{\vec{q}}\cdot\dot{\vec{q}}\right)^2\right\}}\,. \tag{2.86}$$

Having obtained $\vec{q}(t+h)$, provided that $\vec{r}(t+h)$ and $\vec{F}(t+h)$ have also been computed, it is possible to calculate principal torque $\vec{T}^b(t+h)$. A natural procedure would be to calculate the next principal angular velocity $\vec{\omega}^b(t+h)$ as

$$\vec{\omega}^b(t+h) = \vec{\omega}^b(t) + \frac{h}{2}\left\{\dot{\vec{\omega}}^b(t) + \dot{\vec{\omega}}^b(t+h)\right\}. \tag{2.87}$$

However, if Equation 2.7 is rewritten as

$$\begin{aligned}
\dot{\omega}_x^b &= \frac{T_x^b}{I_{xx}^b} + \omega_y^b \omega_z^b \frac{I_{yy}^b I_{zz}^b}{I_{xx}^b}, \\
\dot{\omega}_y^b &= \frac{T_y^b}{I_{yy}^b} + \omega_z^b \omega_x^b \frac{I_{zz}^b I_{xx}^b}{I_{yy}^b}, \\
\dot{\omega}_z^b &= \frac{T_z^b}{I_{zz}^b} + \omega_x^b \omega_y^b \frac{I_{xx}^b I_{yy}^b}{I_{zz}^b},
\end{aligned} \tag{2.88}$$

it is clear that the angular acceleration has a non-linear dependence on the angular velocity, thus making Equation 2.87 also non-linear. It is necessary to iteratively calculate Equation 2.88 in order to obtain a solution. A rough estimation of the principal angular acceleration $\dot{\vec{\omega}}^{b(0)}$ can be given by only considering the principal torque part of Equation 2.88,

$$\dot{\vec{\omega}}^{b(0)} = \left(\mathbf{I}^b\right)^{-1} \cdot \vec{T}^b \tag{2.89}$$

with $\mathbf{I}^b$ being the principal inertia moment matrix

$$\mathbf{I}^b = \begin{pmatrix} I_{xx}^b & 0 & 0 \\ 0 & I_{yy}^b & 0 \\ 0 & 0 & I_{zz}^b \end{pmatrix}, \tag{2.90}$$

and $\vec{T}^b$ being the principal torque. With this it is also possible to estimate angular velocity $\vec{\omega}^{b(0)}$:

$$\vec{\omega}^{b(0)}(t+h) = \vec{\omega}^b(t) + \frac{h}{2}\left\{\dot{\vec{\omega}}^{b(0)}(t+h) + \dot{\vec{\omega}}^b(t)\right\}. \tag{2.91}$$

This value can now be used to get a more precise estimate of principal angular acceleration via Equation 2.88. At least three iterations are needed to obtain a satisfactory estimation. In this research, the iterations are continued until the absolute difference of the angular velocity components between iterations is less than 0.02 rad/s, with the upper limit being one-hundred iterations.

2.7.3 Numerical integration under pressure control

When under pressure control, the equation of motion for translational motion is modified and system volume becomes a variable with its own equation of motion, therefore

reformulation of numerical integration is needed. The volume size $V(t+h)$ is obtained only by straightforward substitution

$$\begin{aligned} V(t+h) &= V(t) + h\dot{V}(t) + \frac{h^2}{2}\ddot{V}(t) \\ &= \left[1 + N_P \cdot h\eta(t) + \frac{N_P \cdot h^2}{2}\left\{\dot{\eta}(t) + N_P \cdot \eta(t)^2\right\}\right] V(t), \end{aligned} \tag{2.92}$$

where $\dot{\eta}(t)$ is obtained by either Equation 2.50 or 2.58, and N_P is the number of pressure control directions: 3 for the original bulk pressure control scheme and 1 for one-dimensional local pressure control. The positions for bulk pressure control scheme $\vec{r}(t+h)$ and the control component α for that of one-dimensional local pressure control scheme $r^\alpha(t+h)$ are obtained in a similar way

$$\begin{aligned} \vec{r}(t+h) &= \vec{r}(t) + h\dot{\vec{r}}(t) + \frac{h^2}{2}\ddot{\vec{r}}(t) \\ &= \left[1 + h\eta(t) + \frac{h^2}{2}\left\{\dot{\eta}(t) + \eta(t)^2\right\}\right]\vec{r}(t) + h\vec{v}(t) + \frac{h^2}{2m}\vec{F}(t), \end{aligned} \tag{2.93}$$

$$\begin{aligned} r^\alpha(t+h) &= r^\alpha(t) + h\dot{r}^\alpha(t) + \frac{h^2}{2}\ddot{r}^\alpha(t) \\ &= \left[1 + h\eta(t) + \frac{h^2}{2}\left\{\dot{\eta}(t) + \eta(t)^2\right\}\right] r^\alpha(t) + hv^\alpha(t) + \frac{h^2}{2m}F^\alpha(t) \\ &\quad - \operatorname{sgn}\left\{r^\alpha(t)\right\} \cdot \left[h\eta(t) + \frac{h^2}{2}\left\{\dot{\eta}(t) + \eta(t)^2\right\}\right] l^\alpha_{\mathrm{ctrl}}. \end{aligned} \tag{2.94}$$

Using the updated positions the total force $\vec{F}(t+h)$ can be computed. With this, the remaining variables at $t+h$ can be obtained. A simple attempt for calculating the change rate $\eta(t+h)$ is given by

$$\eta(t+h) = \eta(t) + \frac{h}{2}\left\{\dot{\eta}(t) + \dot{\eta}(t+h)\right\}. \tag{2.95}$$

Similarly, velocities for bulk pressure control scheme $\vec{v}(t+h)$ and the control component α for that of one-dimensional local pressure control scheme $v^\alpha(t+h)$ are given by

$$\begin{aligned} \vec{v}(t+h) &= \vec{v}(t) + \frac{h}{2}\left\{\dot{\vec{v}}(t) + \dot{\vec{v}}(t+h)\right\} \\ &= \frac{1}{1 + \frac{h}{2}\eta(t+h)}\left[\left\{1 - \frac{h}{2}\eta(t)\right\}\vec{v}(t) + \frac{h}{2m}\left\{\vec{F}(t) + \vec{F}(t+h)\right\}\right], \end{aligned} \tag{2.96}$$

$$\begin{aligned} v^\alpha(t+h) &= v^\alpha(t) + \frac{h}{2}\left\{\dot{v}^\alpha(t) + \dot{v}^\alpha(t+h)\right\} \\ &= \frac{1}{1 + \frac{h}{2}\eta(t+h)}\left[\left\{1 - \frac{h}{2}\eta(t)\right\}v^\alpha(t) + \frac{h}{2m}\left\{F^\alpha(t) + F^\alpha(t+h)\right\}\right]. \end{aligned} \tag{2.97}$$

This obviously creates a problem, since $\eta(t+h)$ is necessary to calculate $\vec{v}(t+h)$ and $v^\alpha(t+h)$, but $\eta(t+h)$ itself is obtained by either Equation 2.50 or 2.58, which requires

pressure that is obtained by either Equation 2.43 or 2.48, and where the velocities at $t+h$ are required. A non-linear relation exists that must be solved iteratively. Firstly, an estimate of the velocities is calculated by

$$\vec{v}^{(0)}(t+h) = \left\{1 - \frac{h}{2}\eta(t)\right\}\vec{v}(t) + \frac{h}{2m}\left\{\vec{F}(t) + \vec{F}(t+h)\right\}, \tag{2.98}$$

$$v^{\alpha(0)}(t+h) = \left\{1 - \frac{h}{2}\eta(t)\right\}v^{\alpha}(t) + \frac{h}{2m}\left\{F^{\alpha}(t) + F^{\alpha}(t+h)\right\}. \tag{2.99}$$

The pressure can be divided into kinetic energy and intermolecular potential energy members,

$$P = P_E + P_\Phi, \tag{2.100}$$

where P_E and P_Φ correspond to the first and second terms on the right-hand side of Equations 2.43 and 2.48, respectively. While $P_\Phi(t+h)$ can be readily calculated from only $\vec{r}(t+h)$ and $V(t+h)$, the following relation holds for P_E

$$P_E(t+h) = \frac{1}{\left\{1 + \frac{h}{2}\eta(t+h)\right\}^2} P_E^{(0)}(t+h), \tag{2.101}$$

where $P_E^{(0)}$ is the kinetic energy term calculated from the estimated velocities. Finally, the i-th estimation of $\eta(t+h)$ is given by the following equation

$$\eta^{(i)}(t+h) = \eta(t) + \frac{h}{2}\left[\dot{\eta}(t) + N_p \cdot \frac{V(t+h)\left\{P_\Phi(t+h) - P_{\mathrm{set}}\right\} + 2k_b T_{\mathrm{set}}}{W}\right] + N_P \cdot \frac{h}{2W}\frac{V(t+h)\,P_E^{(0)}(t+h)}{\left\{1 + \frac{h}{2}\eta^{(i-1)}(t+h)\right\}^2}, \tag{2.102}$$

where the value from the previous time step is used initially $\eta^{(0)}(t+h) = \eta(t)$. The Equation 2.102 is iterated at most one-thousand times or until $\eta^{(i)}(t+h)$ fully converges. Once $\eta(t+h)$ is obtained, velocities can be easily calculated by using the estimations made earlier

$$\vec{v}(t+h) = \frac{1}{1 + \frac{h}{2}\eta(t+h)}\vec{v}^{(0)}(t+h), \tag{2.103}$$

$$v^{\alpha}(t+h) = \frac{1}{1 + \frac{h}{2}\eta(t+h)}v^{\alpha(0)}(t+h). \tag{2.104}$$

Only one non-linear equation must be solved iteratively, thus it is possible to obtain a high-precision solution.

2.8 Calculation Speed-Up Techniques and Boundary Conditions

2.8.1 Cut-off

By only considering interactions between sites closer than a cut-off distance r_{cut} and neglecting any possible effect further than that, calculation time is greatly saved because the number of interactions to be calculated is reduced. The Coulomb and L-J interactions in Equations 2.17 and 2.18 are truncated at a cut-off distance r_{cut} using the Heaviside step function H_{cut} and approach zero smoothly at r_{cut} with the coefficients in Equations 2.107 and 2.108:

$$\Phi_{\text{C}}(r_{ij}) = H(r_{\text{cut}} - r_{ij}) \cdot \frac{q_i q_j}{4\pi\varepsilon_0} \left[\frac{1}{r_{ij}} + \frac{1}{r_{\text{cut}}} \left\{ c_{\text{C}}^2 \left(\frac{r_{ij}}{r_{\text{cut}}} \right)^2 - c_{\text{C}}^0 \right\} \right], \tag{2.105}$$

$$\Phi_{\text{LJ}}(r_{ij}) = H(r_{\text{cut}} - r_{ij}) \cdot 4\varepsilon_{ij} \left[\left(\frac{\sigma_{ij}}{r_{ij}} \right)^{12} - \left(\frac{\sigma_{ij}}{r_{ij}} \right)^6 + \left\{ c_{\text{LJ}}^2 \left(\frac{r_{ij}}{r_{\text{cut}}} \right)^2 - c_{\text{LJ}}^0 \right\} \right], \tag{2.106}$$

$$\begin{aligned} c_{\text{LJ}}^2 &= 6 \left(\frac{\sigma_{ij}}{r_{\text{cut}}} \right)^{12} - 3 \left(\frac{\sigma_{ij}}{r_{\text{cut}}} \right)^6, \\ c_{\text{LJ}}^0 &= 7 \left(\frac{\sigma_{ij}}{r_{\text{cut}}} \right)^{12} - 4 \left(\frac{\sigma_{ij}}{r_{\text{cut}}} \right)^6, \end{aligned} \tag{2.107}$$

$$\begin{aligned} c_{\text{C}}^2 &= \frac{1}{2}, \\ c_{\text{C}}^0 &= \frac{3}{2}. \end{aligned} \tag{2.108}$$

Heaviside step function H_{cut} is defined as follows

$$H_{\text{cut}}(r) = \begin{cases} 0, & r < 0 \\ 1, & r \geq 0 \end{cases}. \tag{2.109}$$

It is a common practice to set r_{cut} to 2.5σ or 3σ in systems consisting of only L-J particles. Because the Coulomb potential is also cut-off in this work, the cut-off distance is set to $r_{\text{cut}} = 1.5$ nm $\approx 5\sigma_{\text{O}}$ to partly account for its long-range tail. This still results in some undesirable effects such as lower interfacial tensions, but since the essential phenomena such as surface tension dependence on temperature remain unchanged,[51] and exactly reproducing physical properties is not the objective of this work, it is deemed sufficient.

Equation 2.106 is integrated as described in Section 2.2.4 to also produce a cut-off version of the potential wall

$$\Phi_{\text{W}}(d_{ij}) = H(r_{\text{cut}} - d_{ij}) \cdot \frac{4\pi\varepsilon_{ij}}{r_0^2\sqrt{3}} \left[\left\{ \frac{2}{5} \left(\frac{\sigma_{ij}}{d_{ij}} \right)^{12} - \left(\frac{\sigma_{ij}}{d_{ij}} \right)^6 \right\} d_{ij}^2 - c_{\text{W}}^4 d_{ij}^4 + c_{\text{W}}^2 d_{ij}^2 - c_{\text{W}}^0 \right]. \tag{2.110}$$

The coefficients in Eq. 2.110 are as follows

$$
\begin{aligned}
c_{\mathrm{W}}^{4} &= \frac{1}{r_{\mathrm{cut}}^{2}} \left\{ 6 \left(\frac{\sigma_{ij}}{r_{\mathrm{cut}}} \right)^{12} - 3 \left(\frac{\sigma_{ij}}{r_{\mathrm{cut}}} \right)^{6} \right\}, \\
c_{\mathrm{W}}^{2} &= 14 \left(\frac{\sigma_{ij}}{r_{\mathrm{cut}}} \right)^{12} - 8 \left(\frac{\sigma_{ij}}{r_{\mathrm{cut}}} \right)^{6}, \\
c_{\mathrm{W}}^{0} &= r_{\mathrm{cut}}^{2} \left\{ \frac{42}{5} \left(\frac{\sigma_{ij}}{r_{\mathrm{cut}}} \right)^{12} - 6 \left(\frac{\sigma_{ij}}{r_{\mathrm{cut}}} \right)^{6} \right\}.
\end{aligned}
\tag{2.111}
$$

2.8.2 Boundary conditions

2.8.2.1 periodic boundary conditions

Periodic boundary conditions are used to construct an infinite latticed that replicates the simulation system throughout space. Identical imaginary cells surround the basic simulation cell. Figure 2.17 shows the concept in two-dimensional space. A particle interacts with image particles in neighboring cells in addition to particles in its own cell. Consequently, if a particle leaves a cell by passing the boundary, an identical counterpart enters from the opposing side. In effect, a simulation of infinitively repeated system is conducted with the calculation cost of one cell. To avoid interacting with several image counterparts of the same particle, basic cell dimensions must be larger than $2r_{\mathrm{cut}}$.

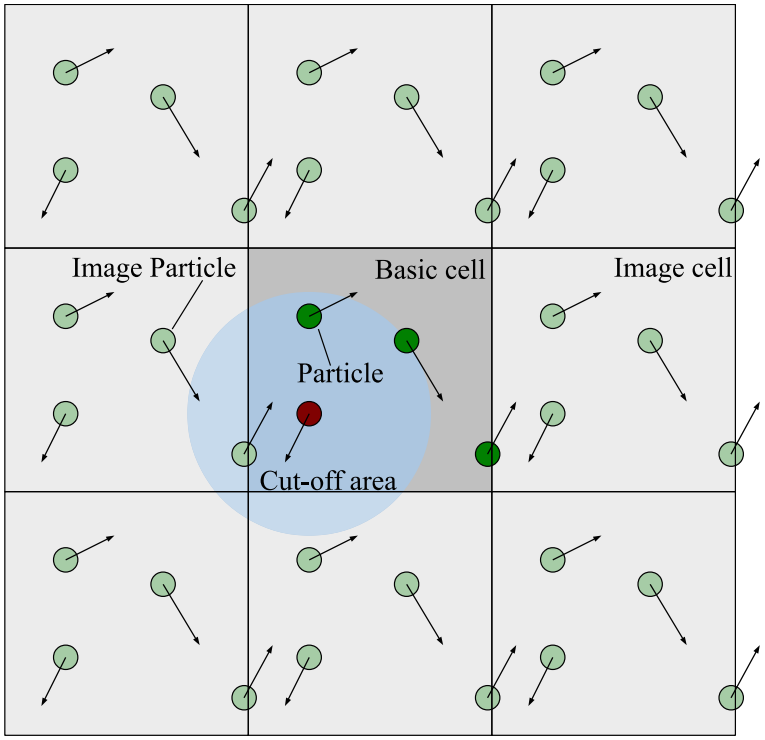

Figure 2.17: Concept of periodic boundary conditions.

2.8.2.2 mirror boundary conditions

Mirror boundary conditions are used as a simple method to prevent particles from wandering outside the calculation cell. The basic premise is shown in Fig. 2.18: once a particle has crossed the mirror boundary, the sign of the velocity component perpendicular to the boundary plane is reversed, thus forcing the particle to return into the calculation cell. Only the total energy of the system is preserved, so this method is not fit for systems where boundary conditions have a great effect. In this work mirror boundary conditions are used only at the boundary facing a vapor phase, where intermolecular interaction is scarce and boundary effect is thought to be negligible.

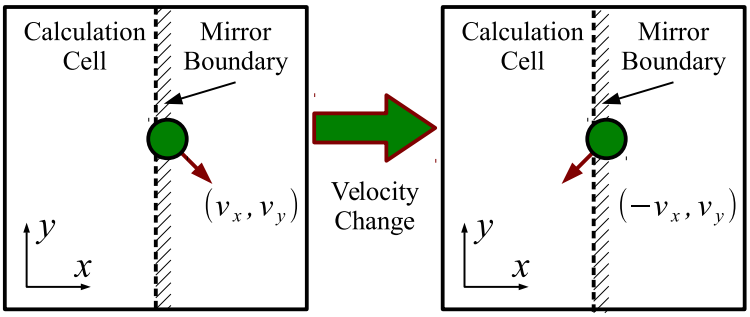

Figure 2.18: Concept of mirror boundary conditions.

2.8.3 Book-keeping

With only using a potential implementing cut-off, there is still a need to calculate the distance of every combination of two sites and check if they are within the cut-off distance at every time step. To avoid this, the book-keeping method is also used. The basic premise is to have a list of nearby site pairs. Upon list creation, all sites within distance of $r_{\text{cut}} + \Delta r_{\text{cut}}$ are included with a margin Δr_{cut} so that the list creation is not mandatory at every time step. During the potential and force calculations, only sites inside pairs in the list are considered, thus saving considerable time. If the maximum absolute displacement among all sites after the previous list creation goes over $\frac{\Delta r_{\text{cut}}}{2}$ the whole list is updated. The margin Δr_{cut} is a parameter between 0.01 and 0.1 nm that is determined before calculation.

In case of a system with pressure control as described in Sections 2.4.3 and 2.4.4, the volume of the calculation system itself changes, thus the distance between particles whose interaction crosses over periodic boundary conditions can change even if the particles themselves do not move. There is no need for special treatment for the case when the system volume is larger than when the list was created, since particle distances can only get larger. On the other hand, if the system volume is smaller than that at the list creation, the maximum possible distance decrease between particles due to volume change is either

$$\sqrt{\left(l^{x(0)}\right)^2 + \left(l^{y(0)}\right)^2 + \left(l^{z(0)}\right)^2} - \sqrt{(l^x)^2 + (l^y)^2 + (l^z)^2} \tag{2.112}$$

for bulk pressure control scheme or

$$l^{\alpha(0)} - l^{\alpha} \tag{2.113}$$

for one-dimensional local pressure control scheme, where l^x, l^y and l^z are the calculation cell dimensions, l^α is the cell dimension of the pressure control direction, and the "(0)" superscript denotes the dimension values at the time of list creation. The value of Equation 2.112 or 2.113 is added to the maximum absolute displacement among interaction sites upon deciding the need for the list update.

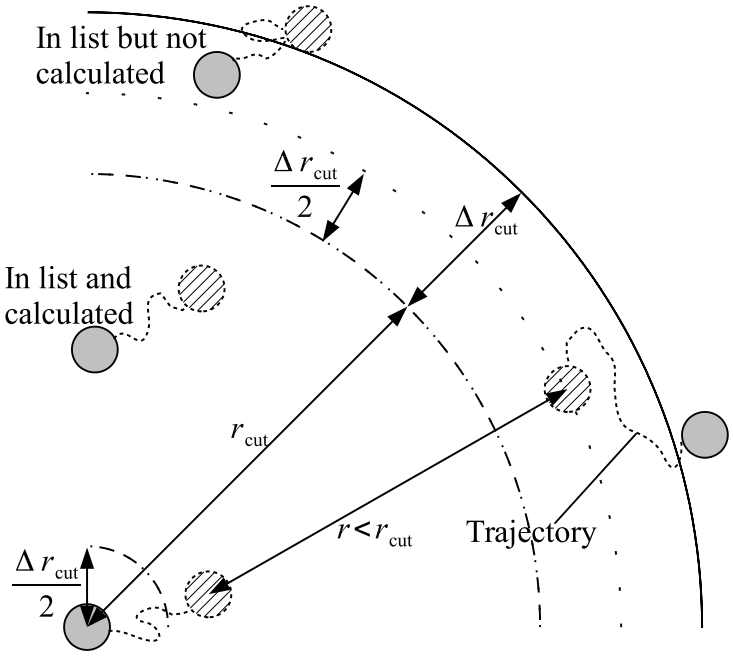

Figure 2.19: Concept of book-keeping method.

3

WATER-ALCOHOL MIXTURE DROPLETS

3.1 Simulation System and Conditions

Creation procedures of simulation systems of water-methanol and water-IPA droplets on a solid surface are described in this section. Essentially, an equilibrium system of a water droplet on a solid surface is created at first, and water-alcohol droplet systems are then created by mixing in alcohol molecules into the previously created water droplet.

3.1.1 Water droplet on a solid surface

As a first step, an equilibrium water droplet system at a constant temperature is created. A cubic lattice consisting of 4000 randomly positioned water molecules is constructed as shown in Fig. 3.1. The periodic boundary conditions are set in all directions with cell dimensions set to $9 \times 3.047 \times 9$ nm^3. The cell dimensions are chosen to produce a droplet with the largest possible diameter, while preventing particles from interacting with multiple images of same particles over the periodic boundaries. It has been suggested that in finite-size interfaces the liquid-vapor interfacial tension increases due to capillary waves,[52,53] and this has been investigates and confirmed for both L-J liquid[54,55] and water systems.[56] Based on those works, the size of y-dimension is large enough to make the effects negligible and it was verified that setting a larger y-dimension does not influence droplet wettability dramatically. Any possible discrepancies in interfacial tensions are also eliminated by using similar dimensions in later systems as well. The simulation is carried out using the SPC/E[36] potential for interaction between water molecules using simple velocity scaling at every 50 steps to maintain a steady temperature at 298.15 K. The time step is set to $h = 1$ fs and the total simulation is

continued for 1 ns. It can be easily seen from Fig. 3.1 that molecules successfully form a quasi-two-dimensional droplet after the equilibration.

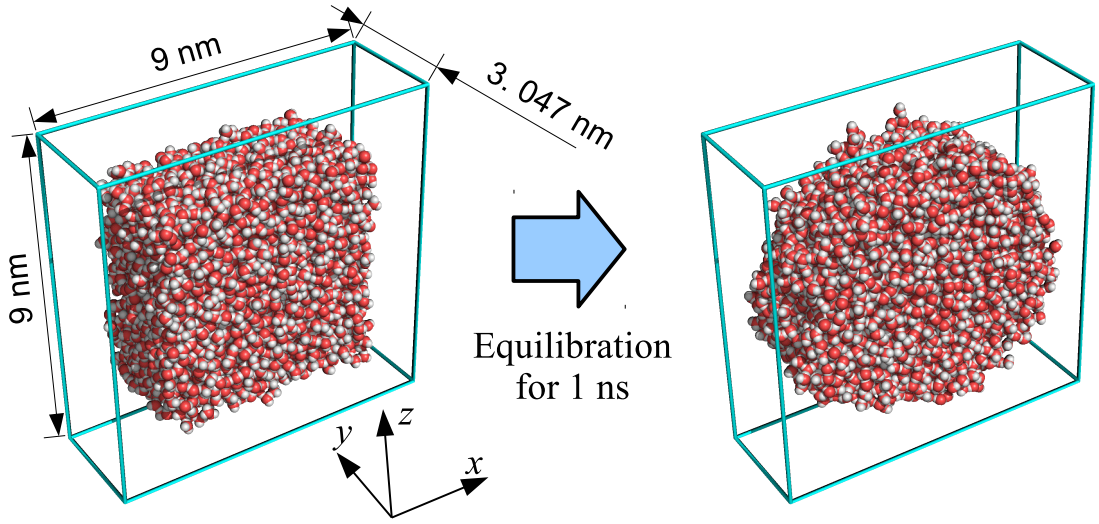

Figure 3.1: Construction of a quasi-two-dimensional liquid droplet.

As a second step, using the final state of the previous equilibration, the system dimensions are expanded to $30.226 \times 3.047 \times 30$ nm^3, and a solid surface with three atom layers forming an fcc (111) lattice is added at the bottom of the calculation cell as shown in Fig. 3.2. Each solid layer contains 1386 atoms, making 4158 surface atoms in total. The liquid droplet is moved so that its center of mass would be at 5 nm distance from the bottom of the calculation cell. Periodic boundaries are imposed in lateral x- and y-directions and mirror boundary is imposed at the top of the calculation cell in the z-direction. This simulation is run with the Langevin temperature control exerted on the second layer of the solid surface, and this maintains the temperature of the whole system at 298.15 K. This equilibration run is continued for 4 ns at a time step of $h = 1$ fs. The time step is chosen so that there would be no temperature gradient inside an equilibrated droplet on a solid surface, and a suitable equilibration time is determined from the density distributions of the droplet at various simulation points. Because the droplet is placed close enough for solid-liquid interactive forces to take place, the droplet is attracted to the solid surface and forms a droplet in full contact with the solid surface by the end of the equilibration as shown in Fig. 3.2.

After the equilibration, simulation are continued for 8 ns under the same conditions and temporal average within this period is used for the analysis of density, contact angle and surface pressure.

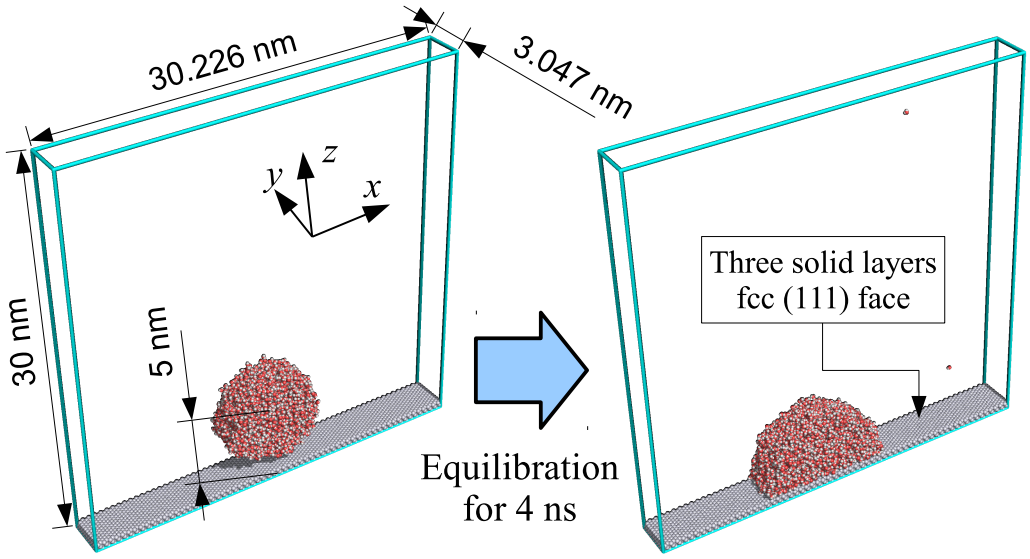

Figure 3.2: Construction of droplet on a solid surface system.

3.1.2 Water-alcohol droplet on a solid surface

As a first step, equilibrium methanol or IPA droplets of various sizes are created in the same manner as the single-component water droplet described in the previous section and shown in Fig. 3.1. The OPLS-UA[37,38] potential is used for methanol and IPA molecules. All calculation conditions are identical to those used for single-component water droplet, except for the equilibration times, which are 450 ps and 300 ps for methanol and IPA, respectively.

In the second step, the equilibrated system containing a water droplet in contact with a solid surface from the previous section and shown in Fig. 3.2 is used. The equilibrated alcohol droplets are positioned at the center of this system with an initial downward velocity set to 10 m/s as illustrated in Fig. 3.3. All simulation conditions are identical to those used in the previous section for the system in Fig. 3.2, except for the equilibration time, which is set to 8 ns because more time is needed for the systems to reach a chemical equilibrium and produce consistent density distributions. The compositions of these systems are shown in Tables 3.1 and 3.2, where methanol and IPA mass fractions, f_{MeOH} and f_{IPA} respectively, are also provided.

Table 3.1: Compositions of water-methanol mixture droplets.

MeOH mass fraction, f_{MeOH} (%)	8	15	21	26	31	35
# of water molecules	4000	4000	4000	4000	4000	4000
# of MeOH molecules	200	400	600	800	1000	1200

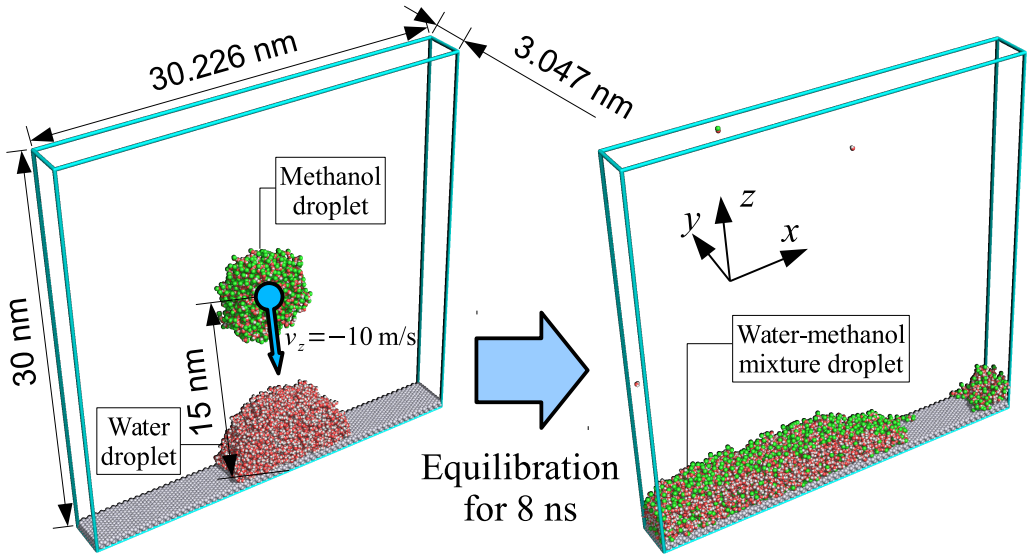

Figure 3.3: Construction of a water-methanol mixture droplet. Water-IPA droplets are constructed in the same way.

Table 3.2: Compositions of water-IPA mixture droplets.

IPA mass fraction, f_{IPA} (%)	8	14	20	25	29
# of water molecules	4000	4000	4000	4000	4000
# of IPA molecules	100	200	300	400	500

After the equilibration, simulations are continued for 8 ns and the temporal average within this period is used for the analysis of density, contact angle and surface pressure.

3.2 General Tendencies and Density Distributions

3.2.1 Water droplet on a solid surface

A snapshot of a droplet on a solid surface is displayed in the left panel of Fig. 3.4. Water molecules form a hemispherical shape on the solid surface and have a contact angle of about 90 degrees. Almost no molecules can be seen in the vapor phase in the snapshot, and indeed the amount of evaporated water molecules is low. The two-dimensional density distribution of water molecules around the center of mass of the droplet is shown in the right panel of Fig. 3.4. It is clear that a constant bulk density exists inside the droplet, therefore the behavior of micro-scale droplets is thought to be realised to some extent in this work. A great increase in water density can be observed at the solid surface. This shows that an adsorption layer is formed over the whole solid-

liquid interface. A closer look shows that at least two more layers of increased density follow the first adsorption layer, though they are not as distinct as the adsorption layer.

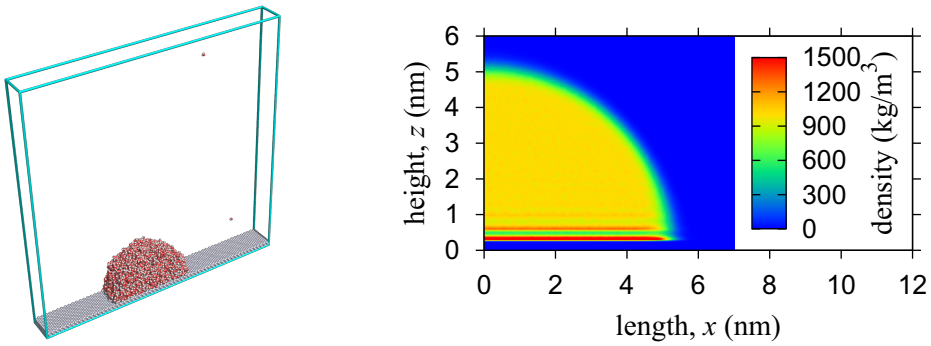

Figure 3.4: (Left) snapshot and (right) two-dimensional density distribution of water droplet on a solid surface.

3.2.2 Water-alcohol droplet on a solid surface

Snapshots and density distributions of the water-methanol and water-IPA mixture droplet systems after equilibration are shown in Figs. 3.5 to 3.10 and Figs. 3.11 to 3.15, respectively. Symmetric density distributions are separately displayed for liquid, water and alcohol, from which the heterogeneous mixing feature can be clearly observed.

3.2.2.1 water-methanol droplet on a solid surface

From the overall snapshots shown in Figs. 3.5 to 3.10, apparent contact angles change dramatically with the increase of methanol fraction f_{MeOH}, and thus wettability shows a noticeable increase. It is also interesting to note that molecules seen in the vapor phase are almost exclusively methanol. This happens because methanol molecules are more volatile, and also because methanol molecules have a stronger tendency to gather at the solid-vapor interface than water molecules, thus they are more exposed to the vapor phase.

In addition, changes in the droplet composition are also apparent. With a low methanol concentration of $f_{\mathrm{MeOH}} = 8\ \%$ shown in Fig. 3.5, methanol molecules have the highest concentration at the three-phase interface line and tend to gather mostly at the solid-liquid interface and to a lesser extent at the liquid-vapor interface. The preference to gather at the three-line interface indicates that in addition to two-phase interfacial tensions, line tension also changes due to alcohol additives, although this does not have

any influence on wettability because the droplets are quasi-two-dimensional. At a higher methanol concentration of $f_{\mathrm{MeOH}} = 15$ % in Fig. 3.6, more methanol molecules extend to the solid-liquid and liquid-vapor interfaces and a solid-liquid mono-layer starts to be formed. This mono-layer is apparently fully formed at $f_{\mathrm{MeOH}} = 21$ % shown in Fig. 3.7. At high concentrations of $f_{\mathrm{MeOH}} \geq 26$ % shown in Figs. 3.8 to 3.10, large amounts of methanol molecules diffuse into the droplet bulk, showing good solubility. On the other hand, no methanol molecules can be observed at the solid-vapor interface even at the highest concentration of $f_{\mathrm{MeOH}} = 35$ % shown in Fig. 3.10. This hints that there is no methanol saturation in the droplet yet, and mixture droplets at even higher concentrations are possible.

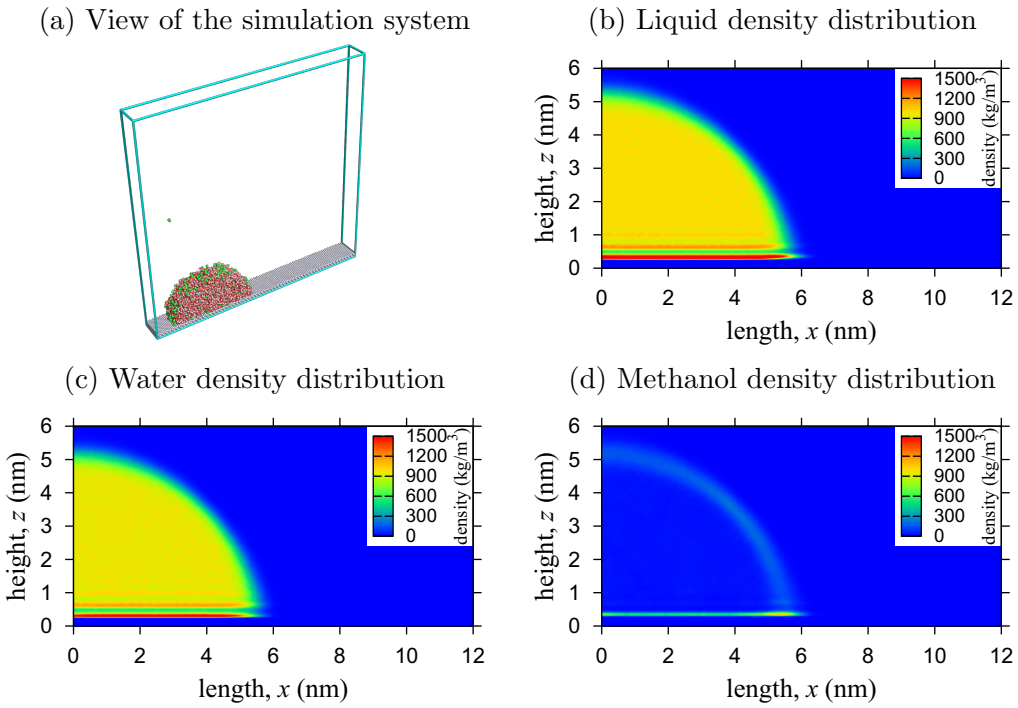

Figure 3.5: Snapshot and two-dimensional density distributions of water-methanol mixture droplet at $f_{\mathrm{MeOH}} = 8$ %.

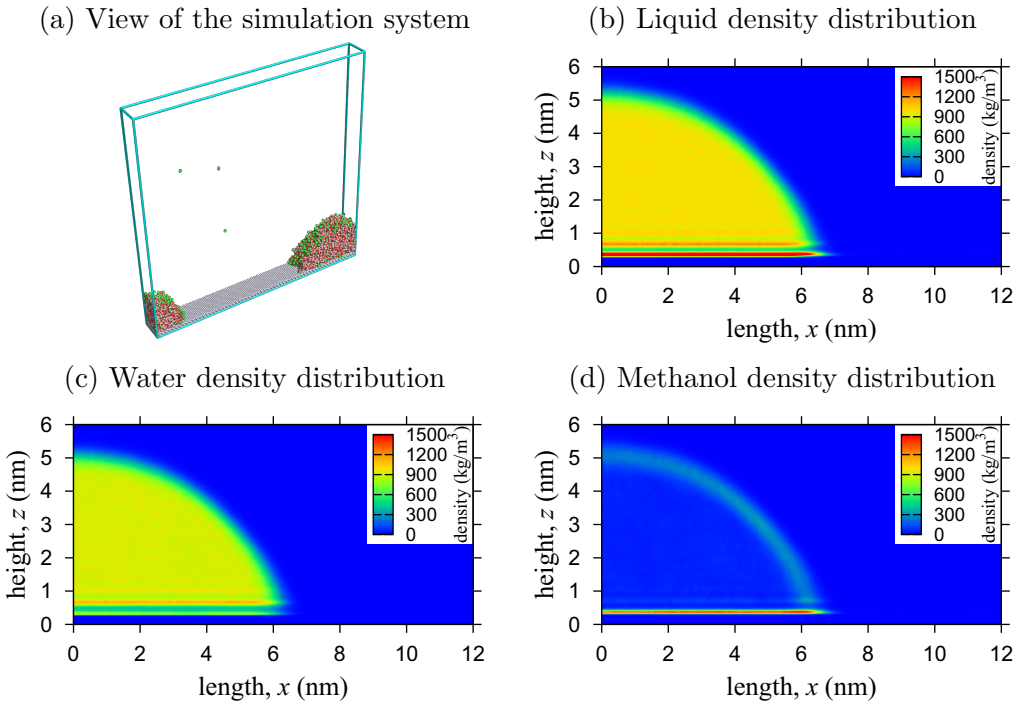

Figure 3.6: Snapshot and two-dimensional density distributions of water-methanol mixture droplet at $f_{\mathrm{MeOH}} = 15$ %.

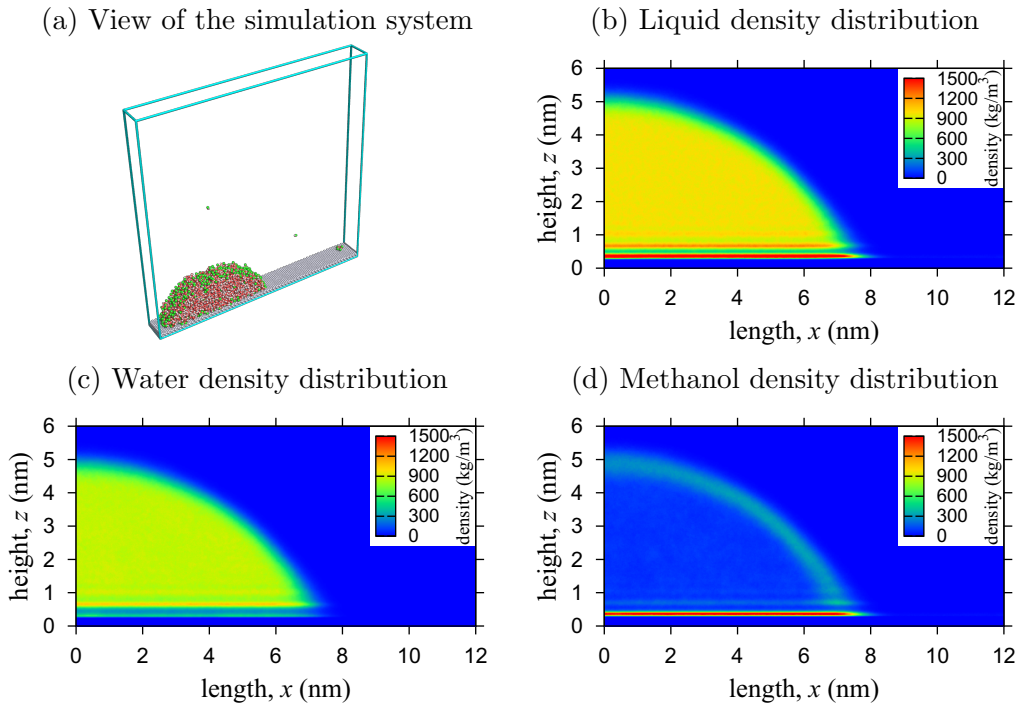

Figure 3.7: Snapshot and two-dimensional density distributions of water-methanol mixture droplet at $f_{\mathrm{MeOH}} = 21$ %.

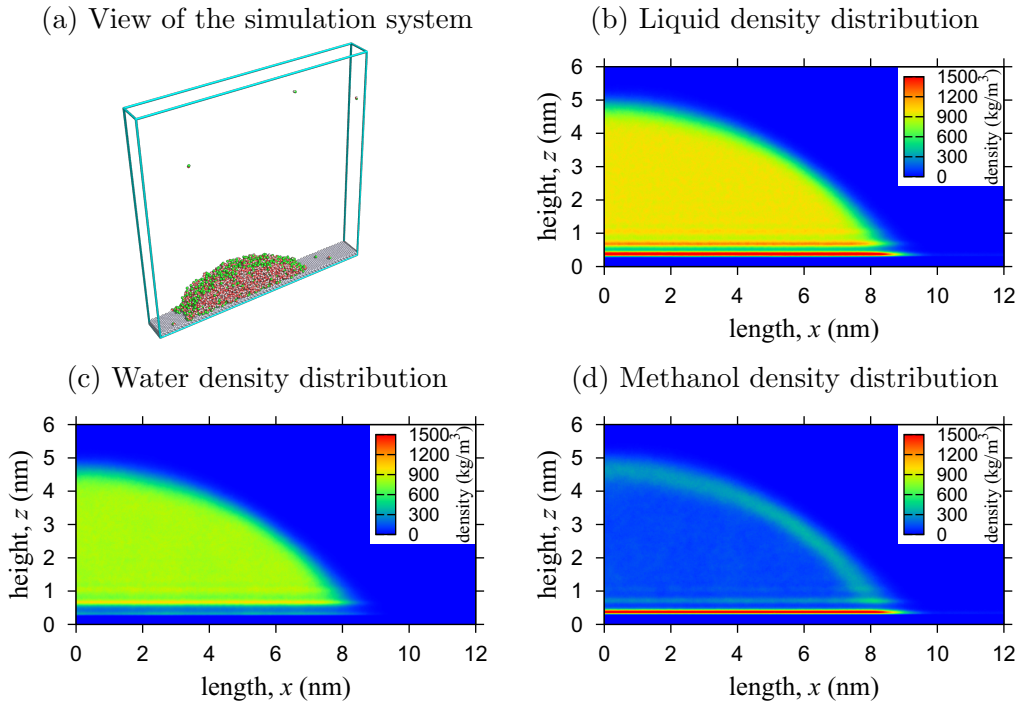

Figure 3.8: Snapshot and two-dimensional density distributions of water-methanol mixture droplet at $f_{\mathrm{MeOH}} = 26$ %.

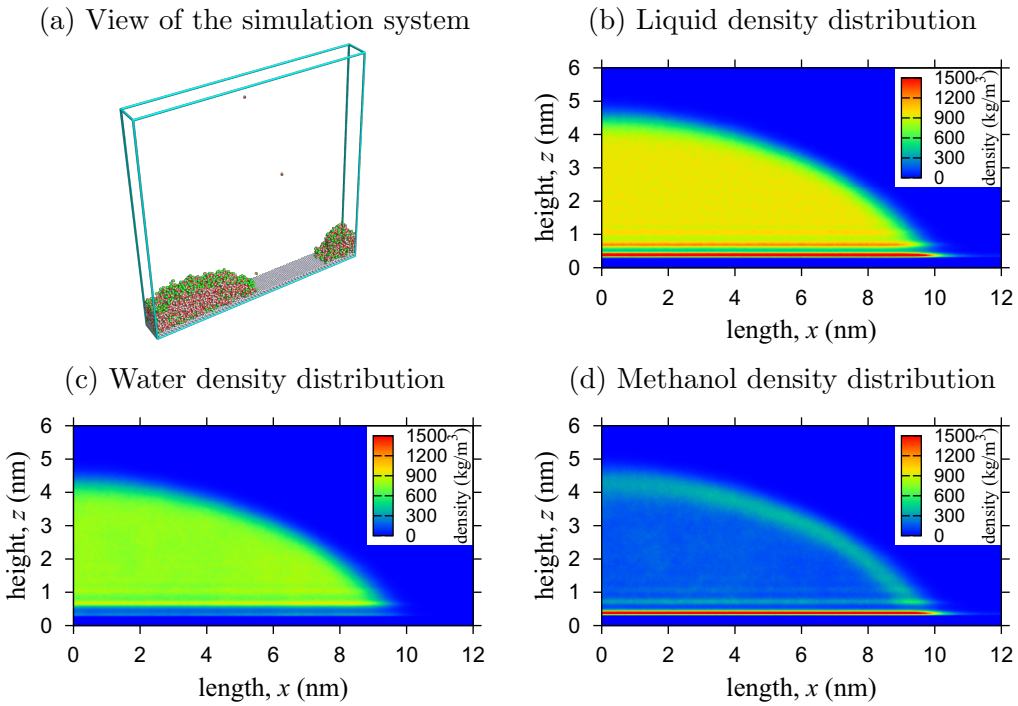

Figure 3.9: Snapshot and two-dimensional density distributions of water-methanol mixture droplet at $f_{\mathrm{MeOH}} = 31$ %.

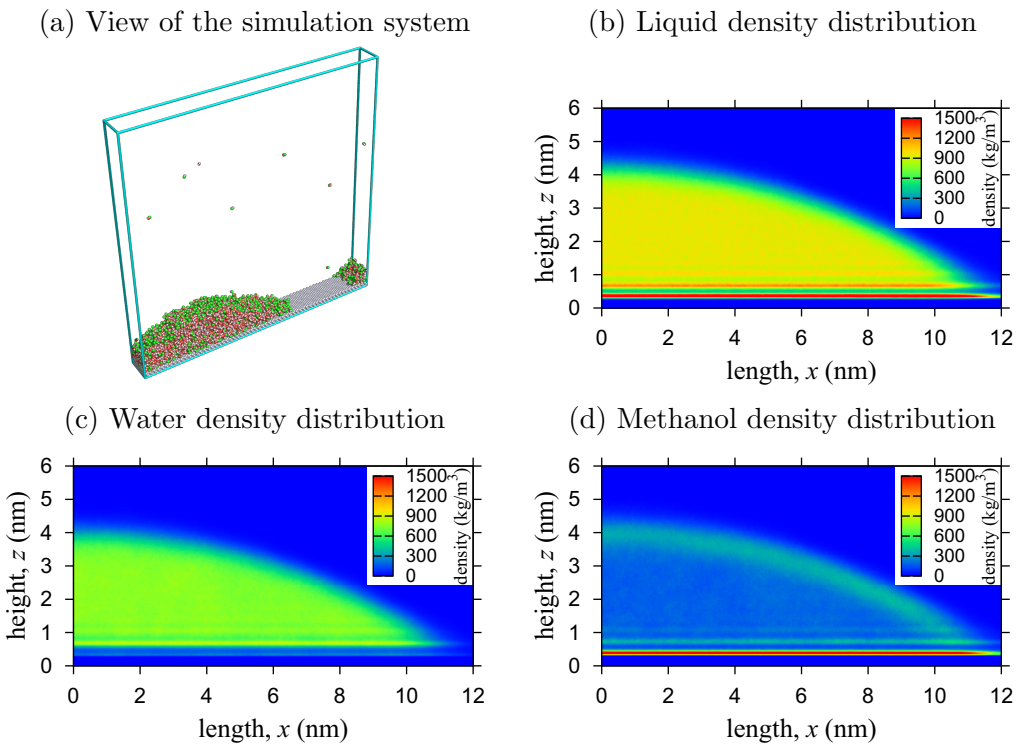

Figure 3.10: Snapshot and two-dimensional density distributions of water-methanol mixture droplet at $f_{\mathrm{MeOH}} = 35$ %.

3.2.2.2 water-IPA droplet on a solid surface

From the overall snapshots shown in Figs. 3.11 to 3.15, it is observed that apparent contact angles change greatly with the increase of IPA fraction f_{IPA}, and wettability shows a substantial increase as with water-methanol droplets. Molecules in the vapor phase are almost exclusively IPA because of higher volatility and due to a tendency to cover liquid-vapor interfaces, which is also similar to water-methanol droplet systems.

The system with a low IPA concentration of $f_{\mathrm{IPA}} = 8$ % shown in Fig. 3.11, has IPA molecules gathering at solid-liquid and solid-vapor interfaces, and this feature is similar to the water-methanol mixture system with a low methanol concentration shown in Fig. 3.5. However, the tendency to gather at the three-phase interface line is much stronger for IPA molecules. In addition, an IPA mono-layer can be observed partly extending from the three-phase interface towards the solid-liquid interface. At higher IPA concentrations of $f_{\mathrm{IPA}} \geq 14$ % in Figs. 3.13 to 3.15, more alcohol molecules gather at the solid-liquid and liquid-vapor interfaces and a distinct IPA mono-layer is formed at the solid-liquid interface. It is remarkable that even at very high concentrations IPA molecules do not diffuse inside the bulk, but rather begin to cover the solid-vapor interface as can be observed in Fig. 3.15, thus creating a very different system compared to that of water-methanol mixture droplets.

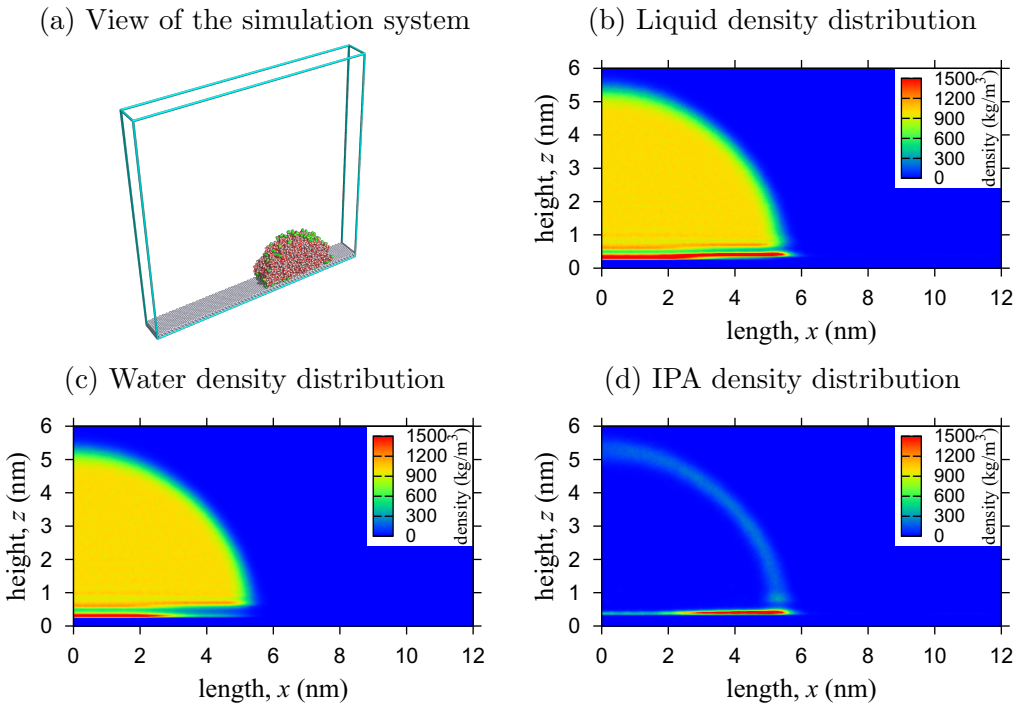

Figure 3.11: Snapshot and two-dimensional density distributions of water-IPA mixture droplet at $f_{\mathrm{IPA}} = 8$ %.

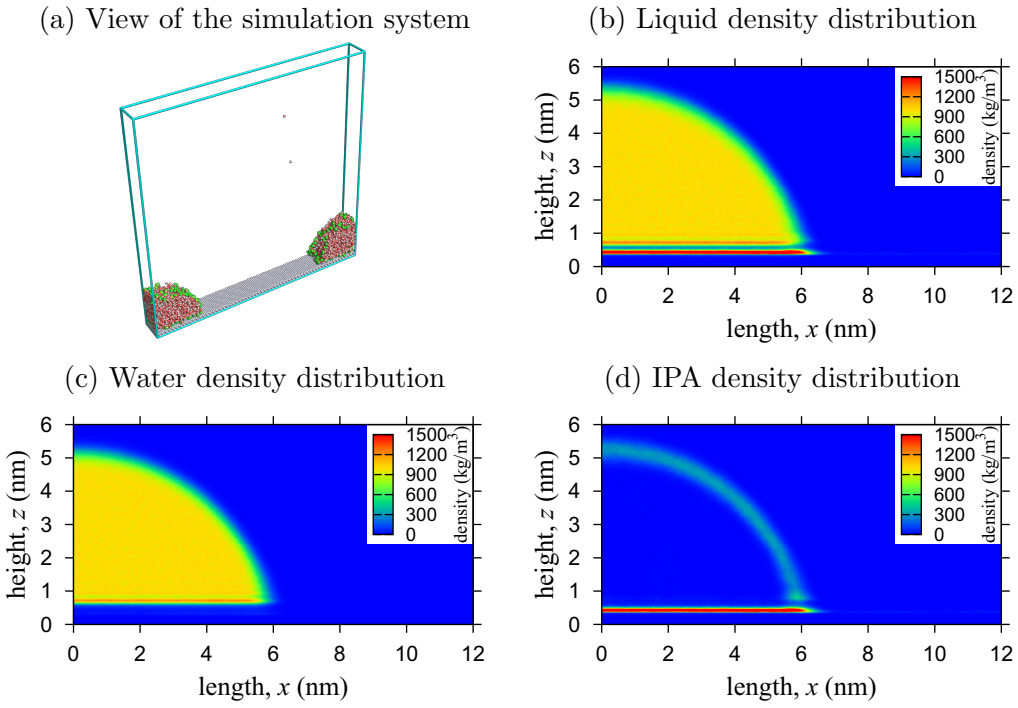

Figure 3.12: Snapshot and two-dimensional density distributions of water-IPA mixture droplet at $f_{\mathrm{IPA}} = 14$ %.

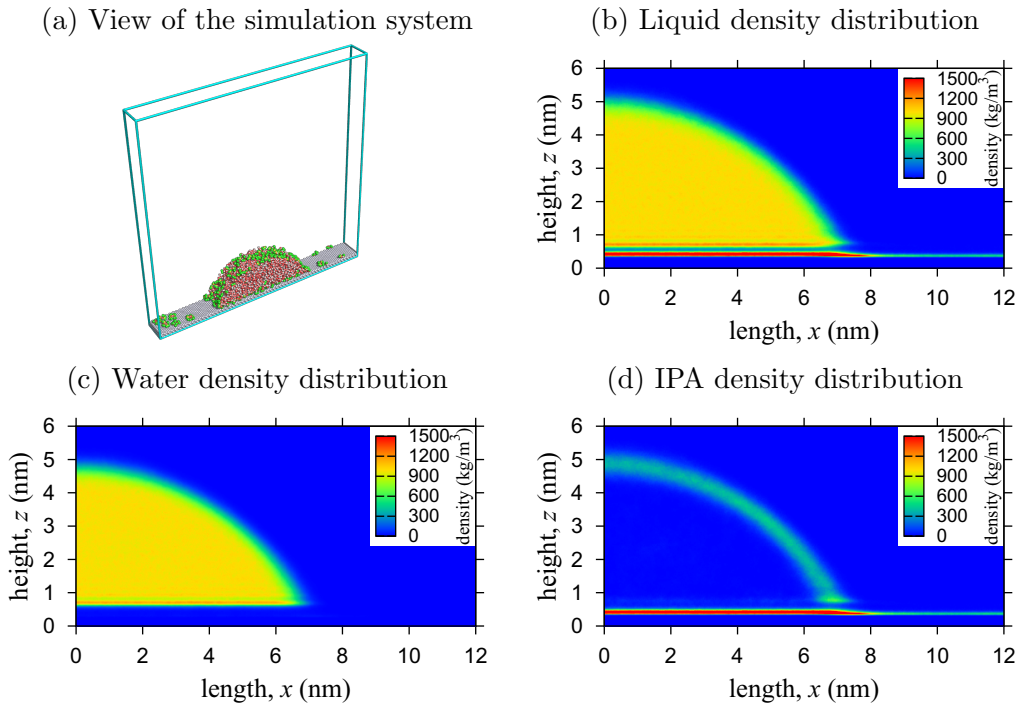

Figure 3.13: Snapshot and two-dimensional density distributions of water-IPA mixture droplet at $f_{\mathrm{IPA}} = 20$ %.

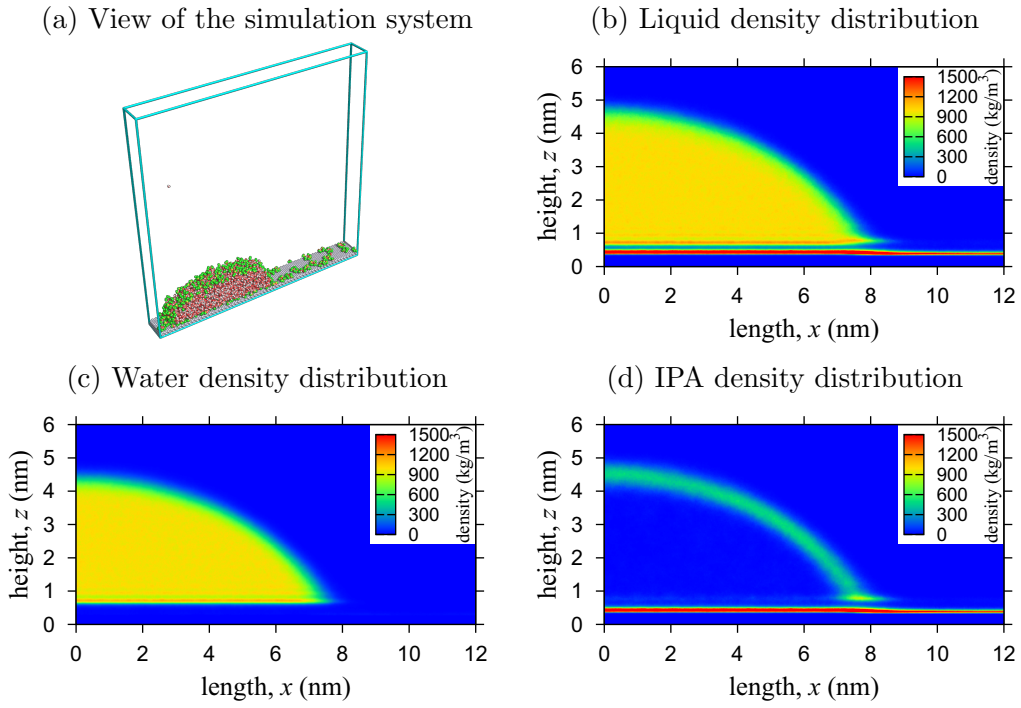

Figure 3.14: Snapshot and two-dimensional density distributions of water-IPA mixture droplet at $f_{\mathrm{IPA}} = 25$ %.

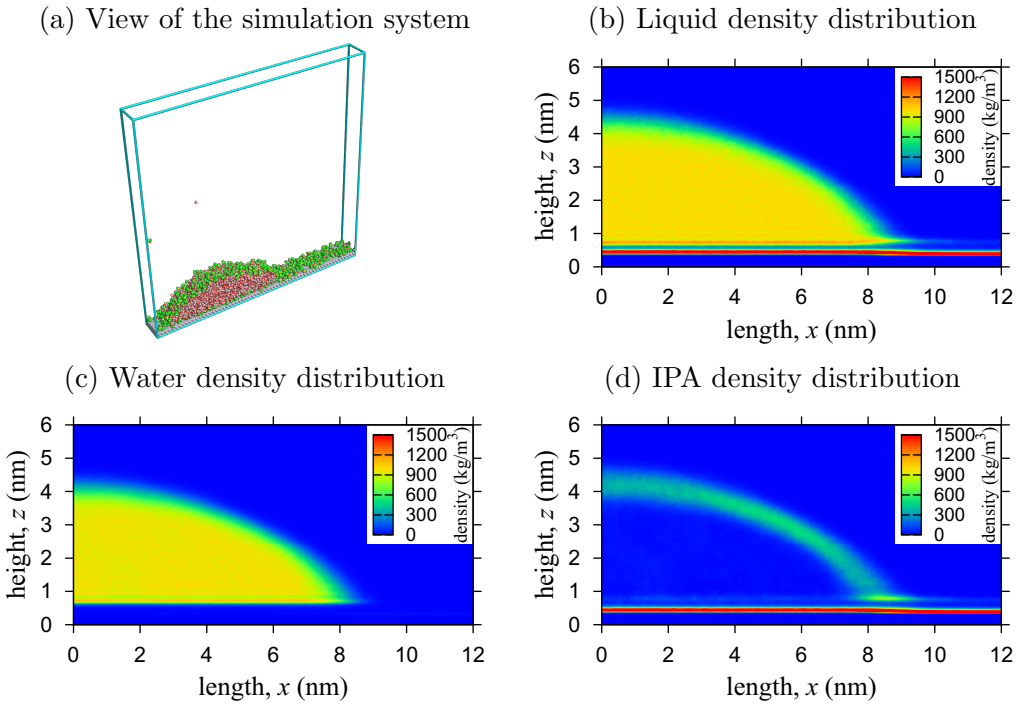

Figure 3.15: Snapshot and two-dimensional density distributions of water-IPA mixture droplet at $f_{\mathrm{IPA}} = 29$ %.

3.3 Contact Angles

An apparent contact angle is evaluated by fitting a circle to a density contour line in liquid-vapor interface region away from the three-phase interface and measuring its angle against a plane elevated above the equilibrium position of the topmost solid surface layer. In other words, the "macroscopic" contact angle and not that of the adsorption layer at the three-phase interface is measured, as was discussed in Section 2.5.5. The density and elevation values are 745 kg/m^3 and 0.365 nm for water-methanol, and 876 kg/m^3 and 0.294 nm for water-IPA droplets, respectively. These density and elevation values are obtained in quasi-one-dimensional systems as discussed in detail later in Section 4.5, in which the positions of solid-liquid and liquid-vapor interfaces are determined from the balance of force and moment due to pressure tensor distribution.[48] The relation between alcohol mass fraction in mixture droplets and the cosine of their contact angle θ is illustrated in Fig. 3.16 for both water-methanol and water-IPA droplets. An obvious increase in wettability with smaller contact angle is observed with increasing alcohol fractions in both water-methanol and water-IPA mixture droplets. The density distributions discussed in the previous Section 3.2.2.2 suggest that the change in contact angle is not simply due to a decrease in liquid-vapor surface tension, but also due to a significant change in the solid-liquid interfacial energy. Both water-methanol and water-IPA droplets mostly show a substantial increase in $\cos\theta$ with the increase of alcohol fractions f_{MeOH} and f_{IPA}, however, the increase seems almost linear for water-methanol systems, while water-IPA systems show a more irregular behavior. Specifically, $\cos\theta$ at an IPA mass fraction of $f_{\mathrm{IPA}} = 8$ % changes very little from that at $f_{\mathrm{IPA}} = 0$ %. This is thought to be because the IPA mono-layer is only formed in proximity to the three-phase interface and there is very little amount of IPA molecules in liquid-vapor and solid-vapor interfaces. Once the IPA mono-layer is formed, however, any extra IPA molecules are free to occupy other interfaces and influence wettability. Because of this, both methanol and IPA molecules seem to enhance wettability to similar amounts at larger mass fractions, although IPA starts to show signs of saturation at higher fractions of $f_{\mathrm{IPA}} > 20$ %.

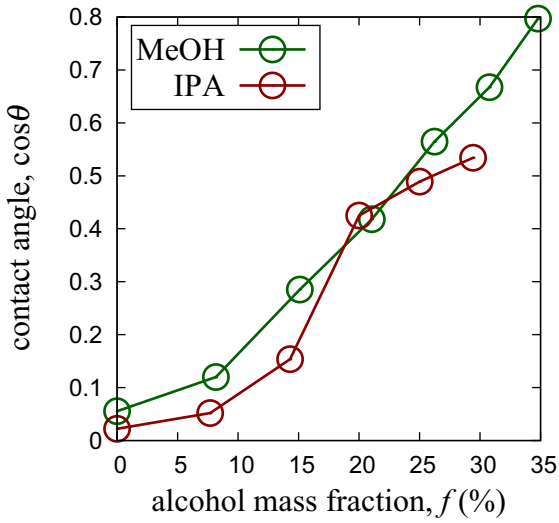

Figure 3.16: Relation between the cosine of contact angle of water-alcohol mixture droplet and alcohol mass fraction.

*Reprinted with permission from "D. Surblys, Y. Yamaguchi, K. Kuroda, M. Kagawa, T. Nakajima and H. Fujimura, The Journal of Chemical Physics, 140, 034505 (2014)". Copyright 2014, American Institute of Physics.

3.4 Surface Pressure Distribution

Normal pressure exerted onto the solid surface by the droplet is evaluated in this section. Specifically, the pressure acting upon a virtual plane parallel to the solid surface set between the solid surface and droplet is calculated. The position of the virtual plane is set at an elevation of 0.59 nm above the bottom solid surface layer, so that no particles pass across it. This height is approximately 0.14 nm above the top layer. The virtual plane is divided into regions with a width of $\frac{5\sqrt{3}}{2}r_0 \approx 1.2$ nm to account for the surface lattice periodicity and provide a smooth distribution.

The surface pressure distribution for the water droplet system is displayed in Fig. 3.17. Three data points nearest to the droplet center show a high pressure of about 10 MPa, which is thought to be the Laplace pressure described in Section 2.5.2. The pressure steeply drops and becomes negative in the vicinity of the contact line, meaning that the surface is being pulled upwards to the droplet. This can be related to the vertical component of the liquid-vapor interfacial tension, which is not accounted by Young's equation discussed in Section 2.5.4, although no quantitative evaluation has been done. Pressure at $x \geq 7$ nm reflects the vapor pressure and is very small due to the lack of liquid molecules in the vapor phase.

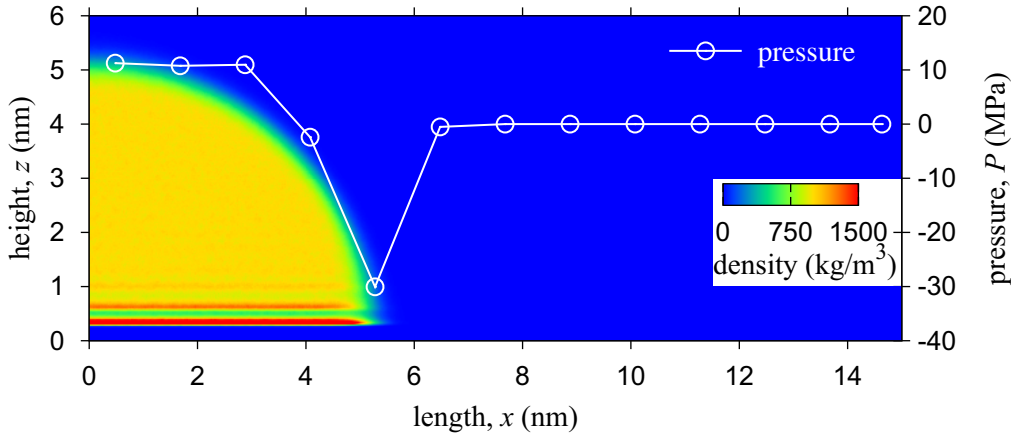

Figure 3.17: Distribution of the normal pressure exerted on the surface in a water droplet system. The density distribution of the liquid molecules is also provided for clarity.

The surface pressure distributions for water-methanol and water-IPA droplet systems are provided in Figs. 3.18 and 3.19, respectively. A general trend can be seen that at greater alcohol mass fractions, the Laplace pressure is reduced and the absolute

value of the negative pressure peak at the contact line is also reduced. Possible causes of this are increase of the droplet radius, decrease of the contact angle and decrease of the liquid-vapor interfacial tensions, and this will be discussed in Section 4.4.

The Laplace pressure plotted against alcohol fraction is shown in Fig. 3.20, where the Laplace pressure is calculated by averaging the data points inside the liquid bulk for every droplet. The vapor pressure is assumed to be zero in all cases. A linear relation can be seen between alcohol mass fraction f and Laplace pressure ΔP for both water-methanol and water-IPA droplets, and the two lines are remarkably similar. This hints that both methanol and IPA molecules have similar effect on the droplet interfaces, which would be in accordance with their similar effect on the contact angle seen in Fig. 3.16. This is rather surprising, considering the great difference in the alcohol distributions inside the mixture droplets.

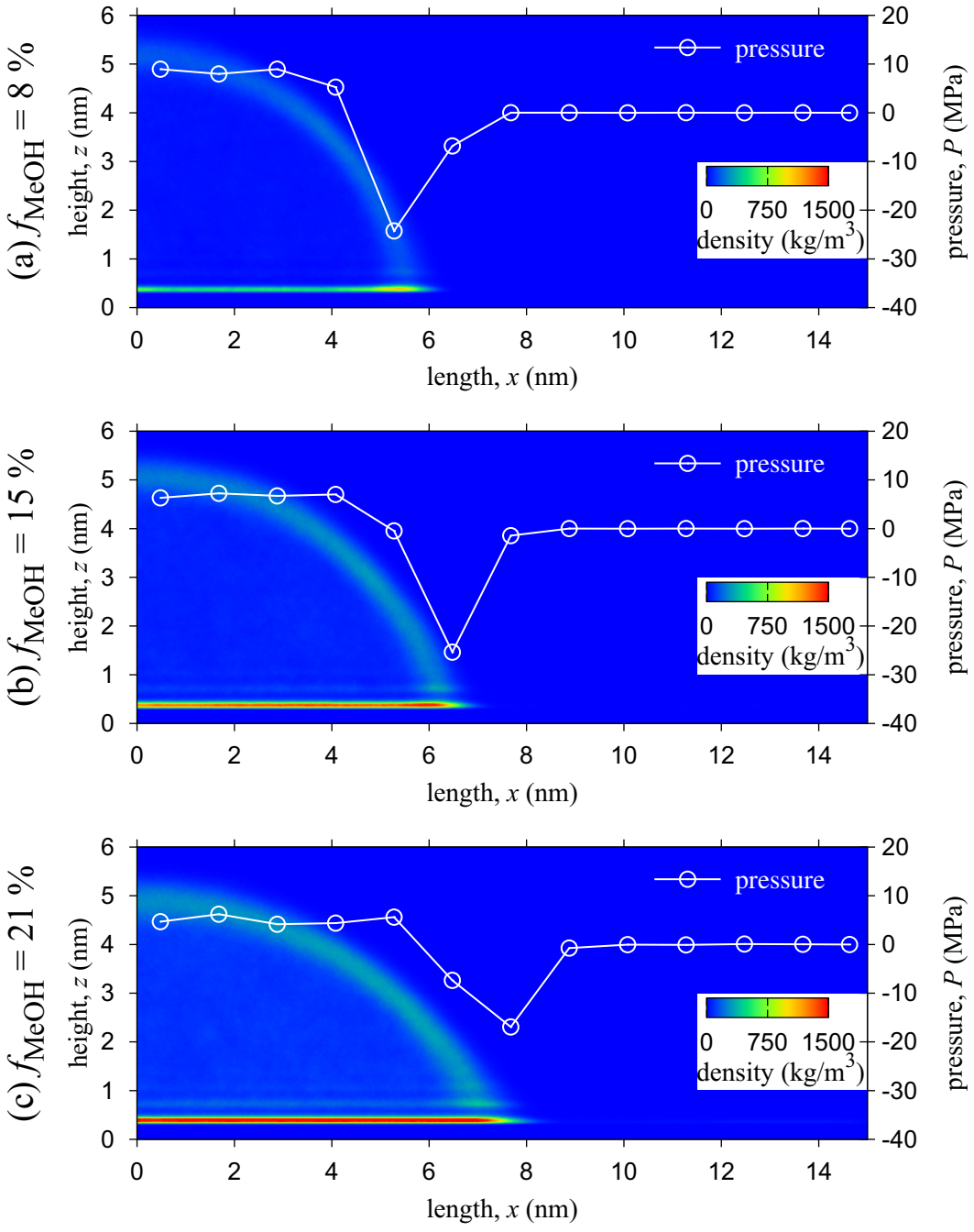

Figure 3.18: Distributions of the normal pressure exerted on the surface in water-methanol systems. The density distributions of the alcohol molecules are also provide for clarity (continue).

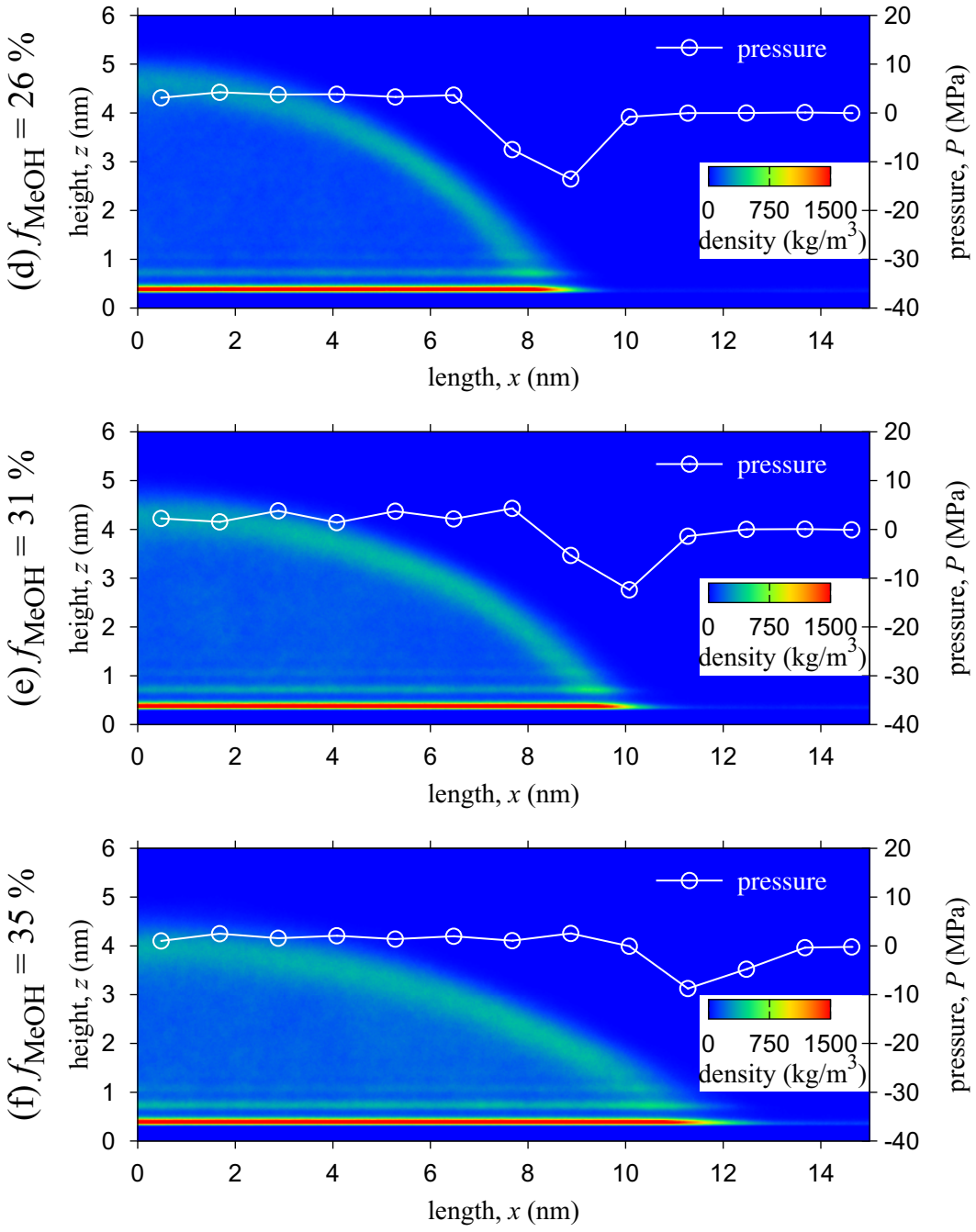

Figure 3.18: (Continued) distributions of the normal pressure exerted on the surface in water-methanol systems. The density distributions of the alcohol molecules are also provide for clarity.

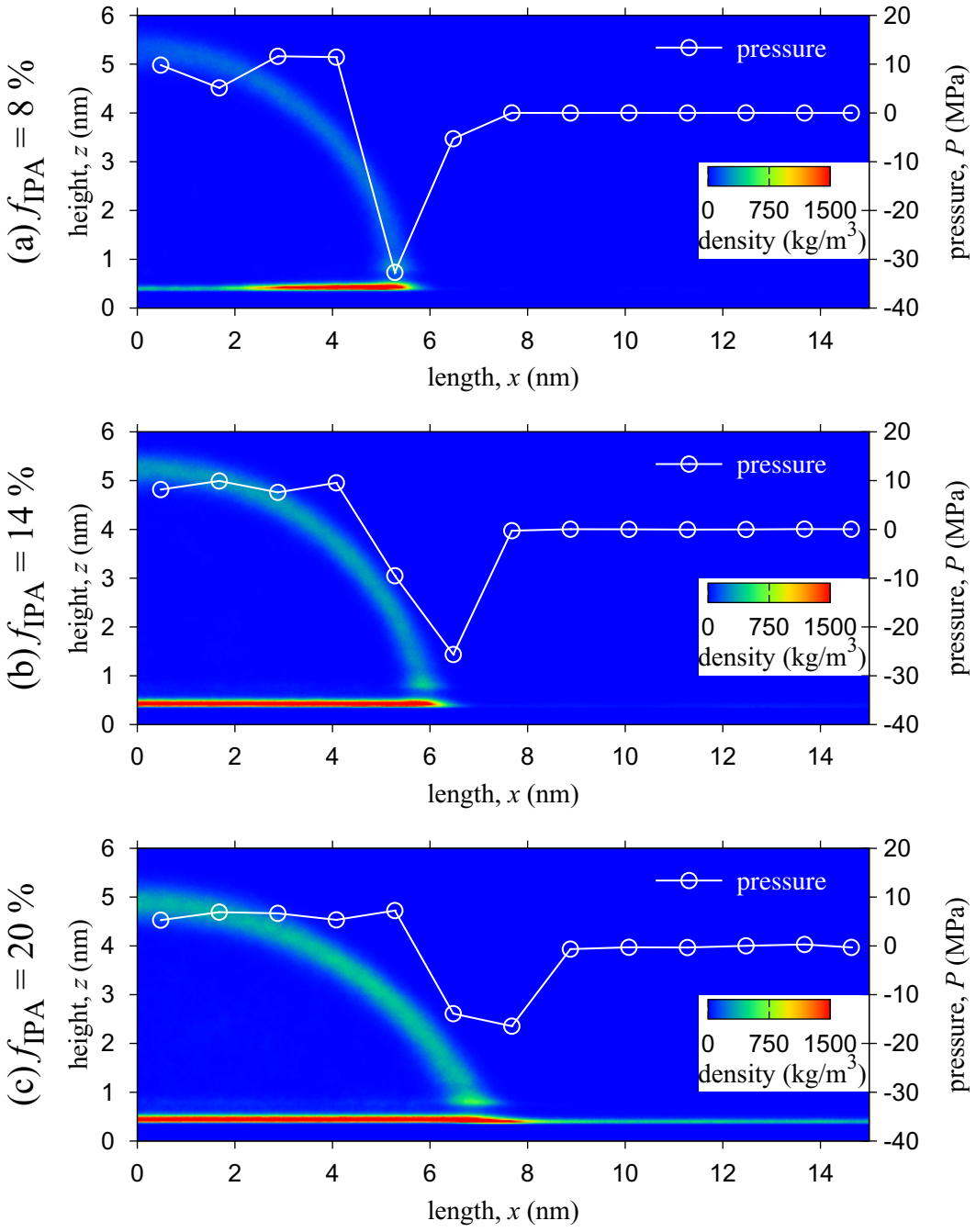

Figure 3.19: Distributions of the normal pressure exerted on the surface in water-IPA systems. The density distributions of the alcohol molecules are also provide for clarity (continue).

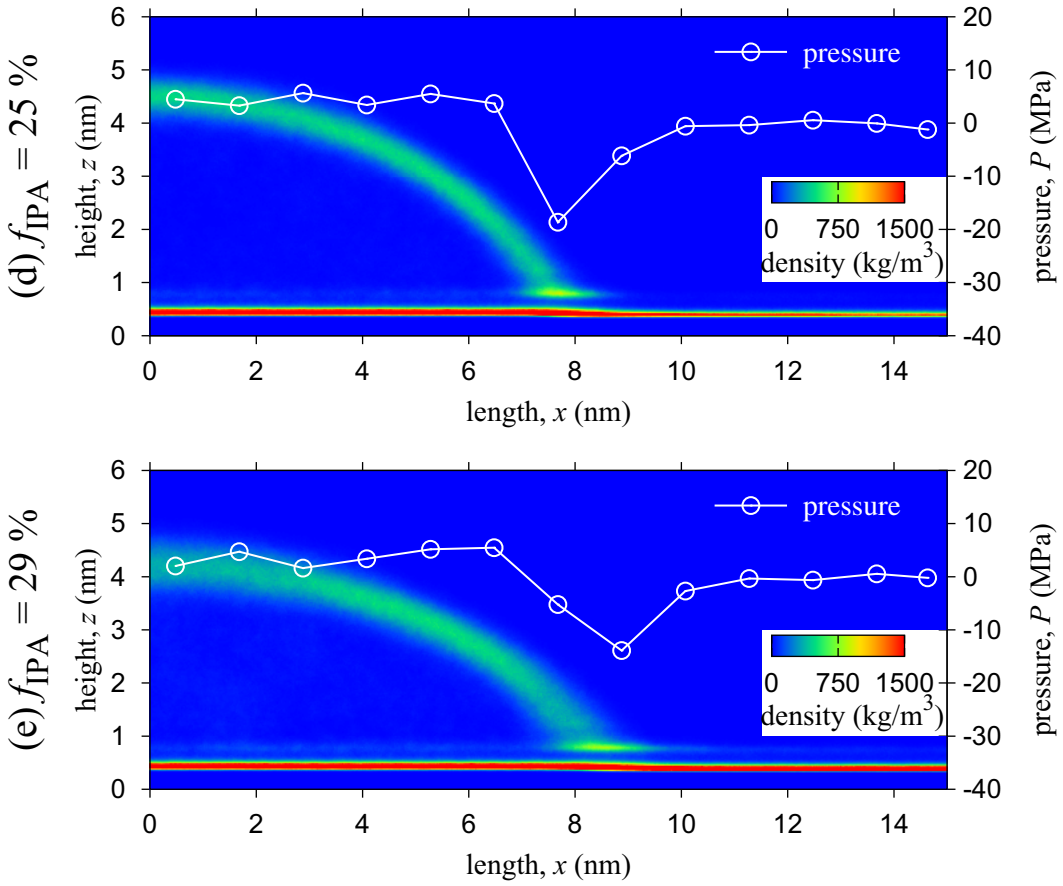

Figure 3.19: (Continued) distributions of the normal pressure exerted on the surface in water-IPA systems. The density distributions of the alcohol molecules are also provide for clarity.

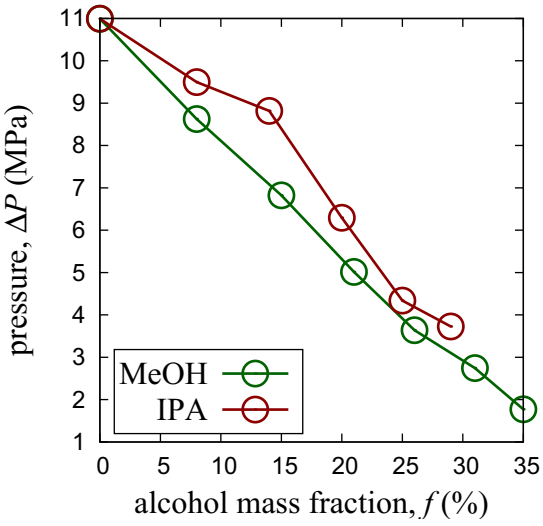

Figure 3.20: Laplace pressure inside droplets.

4

QUASI-ONE-DIMENSIONAL SYSTEMS

Calculation of interfacial tensions is performed in this chapter. The wettability of water and water-alcohol mixture droplets in the previous Chapter 3 is expressed in a very visible and easily understandable way, but it is a non-trivial task to extract interfacial tensions. One of the reasons is that the hemicylindrical droplet shape with a curved surface makes it difficult to directly calculate interfacial properties. To solve this problem, another set of systems which contain only planar interfaces is used.

4.1 Simulation System and Conditions

4.1.1 Systems with solid-liquid and liquid-vapor interfaces

The simulation systems used to investigate solid-liquid and liquid-vapor interfaces are constructed in two steps as shown in Fig. 4.1.

As a first step, a combination of water and alcohol molecules is randomly positioned at cubic lattice points as shown in the left side of Fig. 4.1. Water-methanol and water-IPA compositions are shown in Tables 4.1 and 4.2 and three single-component systems consisting of 1800 water, 800 methanol and 500 IPA molecules are also created. The initial calculation cell dimensions are set to $3.358 \times 3.047 \times 18$ nm^3, and periodic boundary conditions are set in all directions. As with the droplet systems, the cell dimensions are chosen to produce a liquid membrane with the greatest possible thickness, while preventing particles from interacting with multiple images of same particles over the periodic boundaries. For the first equilibration, the system temperature is maintained at 298.15 K using simple velocity scaling. Systems consisting of single-component liquid molecules are equilibrated for 3 ns, while all the other water-alcohol systems are

Table 4.1: Compositions of quasi-one-dimensional systems for water-methanol.

# of water molecules	1800	1800	1800	1800	1800	1800
# of MeOH molecules	100	200	300	400	500	600

Table 4.2: Compositions of quasi-one-dimensional systems for water-IPA.

# of water molecules	1800	1800	1800	1800	1800	1800
# of IPA molecules	50	60	70	80	90	100

equilibrated for 4 ns. The time step is set to $h = 2$ fs for all systems to reduce the calculation cost, because we are not interested in their properties at this point. The equilibration eventually produces a membrane as seen in Fig. 4.1.

As the second and final equilibration step, dimensions for the systems equilibrated in the first step are extended to $3.358 \times 3.047 \times 21$ nm^3, and a solid surface with three atom layers forming an fcc (111) lattice is added at the bottom of the calculation cell, while a mirror boundary condition is set at the top. Each solid layer contains 154 atoms, making 462 surface atoms in total. In addition, the liquid film is set to have a 20 m/s downward velocity as shown in Fig. 4.1. No velocity scaling takes place, and temperature of the system is maintained at 298.15 K using the Langevin temperature control method exerted on the surface particles in the second layer. The equilibration run with a time step of $h = 1$ fs is carried out for 4 ns in the case of systems with single-component liquid films, and for 8 ns and 16 ns for water-IPA and water-methanol systems, respectively. As with the droplet systems, the time step is set so that no temperature gradient would exist in equilibrated systems, while suitable equilibration times are determined to produce equilibrated systems with consistent density distributions.

The average of 8 ns simulation after the equilibration is used for the analysis of solid-liquid and liquid-vapor interfaces.

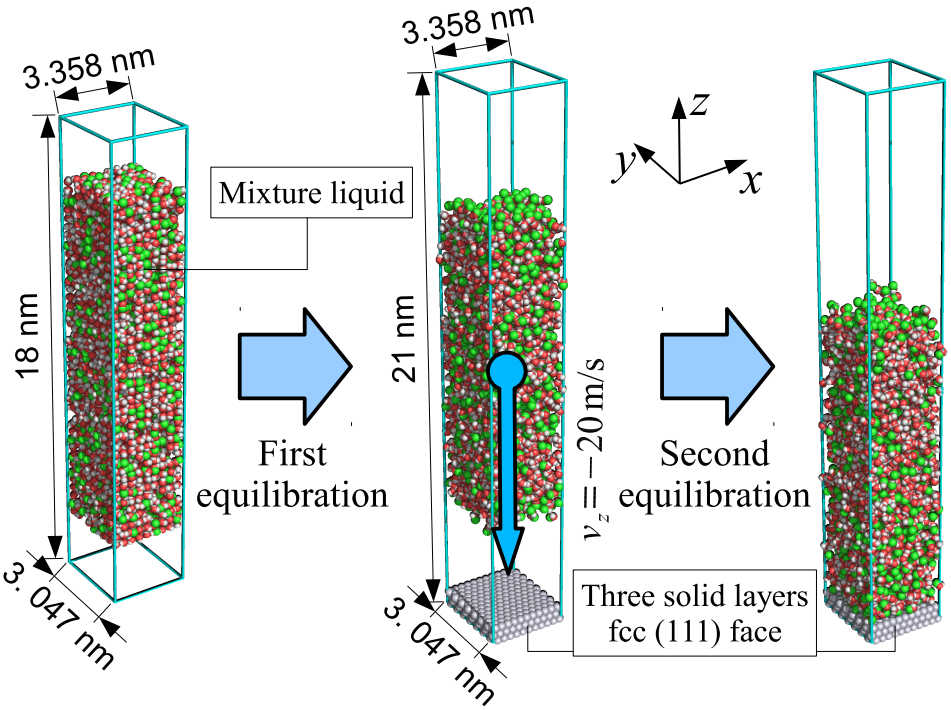

Figure 4.1: Construction process of the simulation systems used for analysis of solid-liquid and liquid-vapor interfaces.

4.1.2 Water-IPA systems with a solid-vapor interface

In water-IPA droplet systems, IPA molecules have a strong tendency to moisten the solid-liquid interface at high concentrations as can be especially clearly observed in Figs. 3.14 and 3.15, while this is not observed in water-methanol droplets. The solid surface area of simulation systems described in the previous section is too small to express the complicated network among the IPA molecules, therefore a bigger simulation system is needed to correctly evaluate the solid-vapor interface. The system used to evaluate solid-vapor interface is displayed in Fig. 4.2, where the number of IPA molecules is set to either 25, 50, 75, 100, 150, 200, 250 or 300, creating nine distinct systems. These numbers were chosen to cover the density range of solid-liquid interfaces of Chapter 3 and no water molecules are included here because the number of water molecules at solid-liquid interfaces there is minuscule. Calculation conditions other than the composition of liquid molecules, i.e. control temperature, interaction with non-polarized solid surface and boundary conditions, are kept unchanged. The systems created this way are equilibrated for 1 ns with $h = 1$ fs time step, which is the same as single-component liquid films in the previous section, although much shorter equilibration times would have been sufficient. After the equilibration, simulations are continued for 4 ns under the same conditions and temporal average within this period is used for the analysis of density and solid-vapor interfacial tensions.

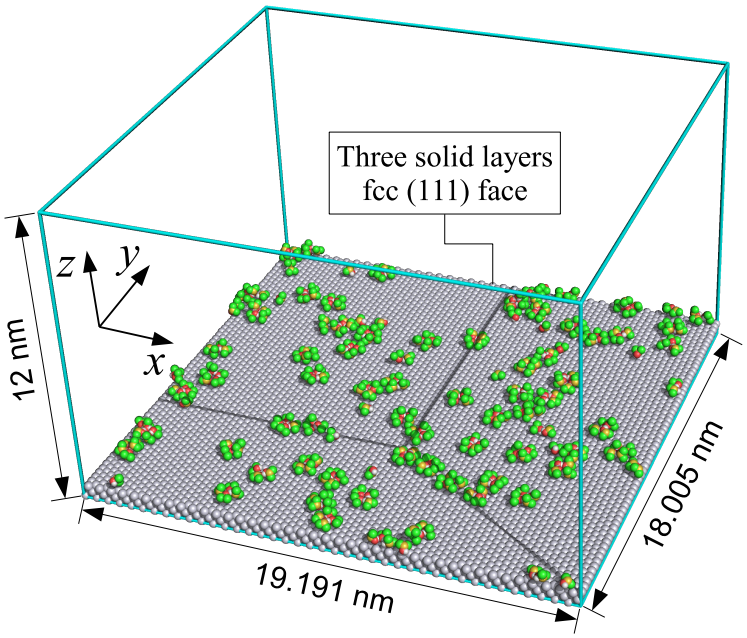

Figure 4.2: Snapshot of a simulation system used to evaluate solid-vapor interfacial tension for IPA molecules.

4.2 Density and Pressure Distribution of Systems with Solid-Liquid and Liquid-Vapor Interfaces

The density and pressure distributions are investigated in this section for systems such as displayed in Fig. 4.1, which contain flat solid-liquid and liquid-vapor interfaces.

The method described in Section 2.4.2 is used to calculate the local pressure tensor. Pressure in the z-direction is set to be the normal pressure $P^N = P^{zz}$, and pressure in the x- and y-directions is set to be the tangential pressure $P^T = \frac{1}{2}\left(P^{xx} + P^{yy}\right)$, where the average of pressure in x- and y- directions is taken to reduce the numerical error of the tangential pressure. Interaction between solid and liquid particles is only taken into account for calculating the normal pressure. It has been shown by Nijmeijer and van Leeuwen[19] that solid-liquid interaction does not contribute to the tangential pressure when the surface structure is periodic, and it is assumed that this is also applicable to this research, as the thermal vibrations in the solid surface are relatively small.

Firstly, one-dimensional density and local pressure distributions along the z-direction of single-component water, methanol and IPA layers are displayed in Fig. 4.3. The normal pressure P^N shown in the left panels of Fig. 4.3 is mostly constant. This is fully expected, since in case of hydrostatic equilibrium, normal pressure must remain unchanged in the whole system as already stated in Section 2.5.1. In addition, it is clear that normal and tangential pressures become equal in the liquid bulk, therefore the thickness of the liquid layers is regarded to be enough and liquid-vapor and solid-liquid interfaces are far enough from each other. It is also notable that the overall pressure of the system is very low because of low saturated vapor pressure, and there are few molecules in the vapor phase. Unlike the normal pressure, the tangential pressure P^T varies largely at liquid-vapor and solid-liquid interfaces, meaning that substantial interfacial tensions exist. By comparing the density and pressure distributions in the right and left panels of Fig. 4.3, it is easy to notice that the tangential tension varies only at the regions where there is also a change in density. This is by no means a coincidence, as a variation in density is highly related to interfacial tensions as also discussed by Nijmeijer and van Leeuwen.[19] This explains the oscillatory nature of the tangential pressure at the solid-liquid interface, where the density distribution also changes in an oscillatory manner. It is interesting to note that the change in the tangential pressure is mostly the same regardless of the liquid type, except for the absolute values of the peaks, which reflect the difference in the interfacial tension values.

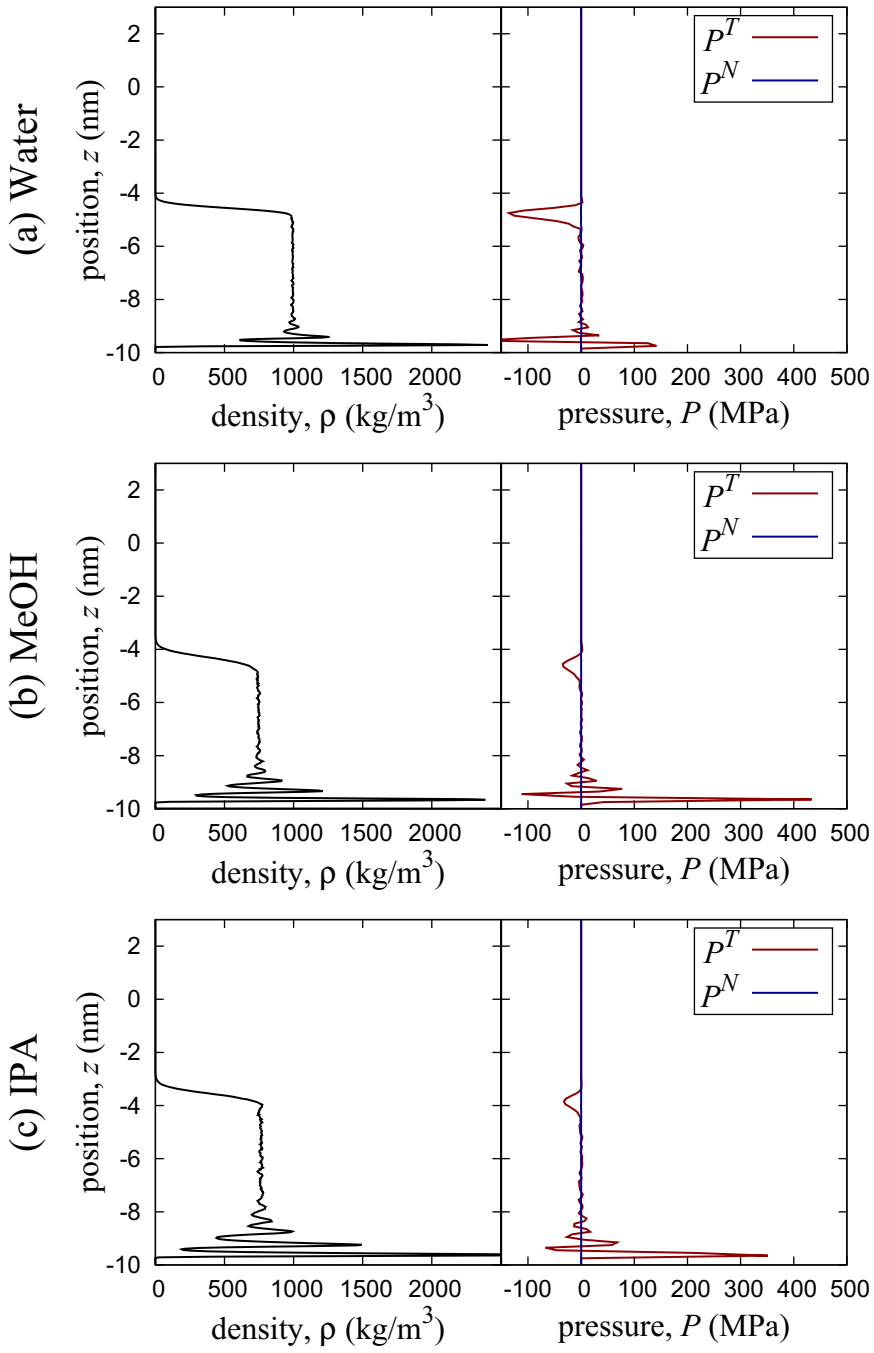

Figure 4.3: Density and pressure distributions of single-component layers, composed of either 1800 water, 800 methanol or 500 IPA molecules.

Density and local pressure distributions along the z-direction for water-methanol and water-IPA liquid layers on a solid surface are displayed in Fig. 4.4 through Fig. 4.7.

Methanol molecules show good solubility as seen in all density graphs in Figs. 4.4 and 4.5. On the other hand, IPA molecules show a higher preference to concentrate at the interfaces, and a noticeable bulk diffusion is only present at systems with a large number of IPA molecules as can be observed in the left panel of Fig. 4.7 (b, c). This difference between methanol and IPA is also present in the droplet systems and can be clearly seen by comparing water-methanol and water-IPA droplets with high alcohol concentrations in Figs. 3.9 and 3.15: methanol molecules diffuse inside the droplet bulk, while IPA molecules prefer to moisten the solid-vapor interface.

The apparent features of the local pressure distributions of water-alcohol mixtures do not differ much from those of single-component layers: the tangential pressure has a negative peak at the liquid-vapor interface and oscillates at the solid-liquid interface. A closer inspection, however, seems to indicate that there is less oscillation in tangential pressure at the solid-liquid interfaces of water-IPA mixtures shown in Figs. 4.6 and 4.7 than water-methanol mixture shown in Figs. 4.4 and 4.5. This is thought to be because IPA molecules only create a single mono-layer at the solid-liquid interface for most mixtures, while methanol molecules create several layers. This causes a greater density oscillation in water-methanol systems, which leads to a greater tangential pressure oscillation at the solid-liquid interface.

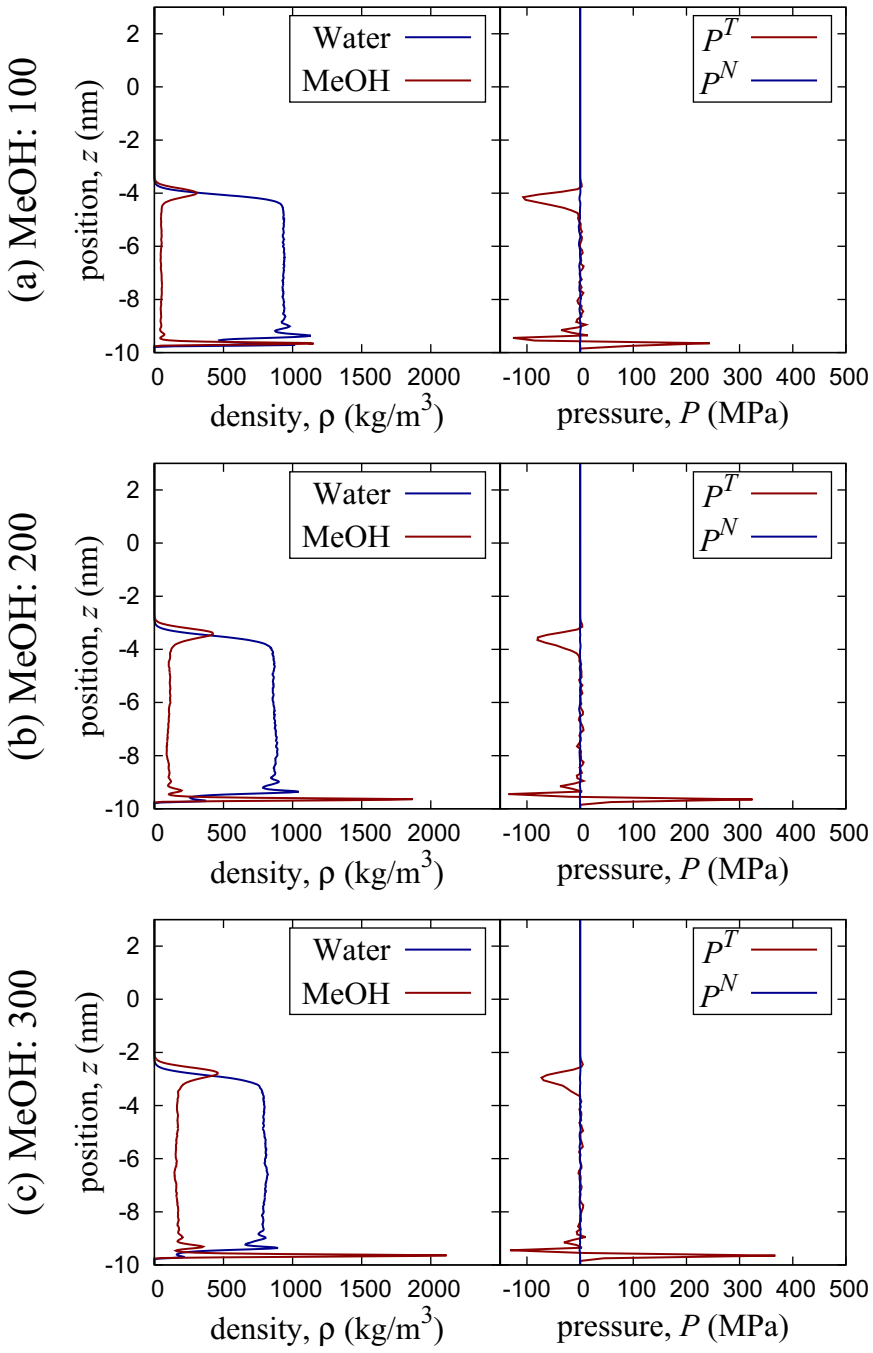

Figure 4.4: Density and pressure distributions of water-methanol mixture layers in systems composed of 1800 water and 100, 200 or 300 methanol molecules.

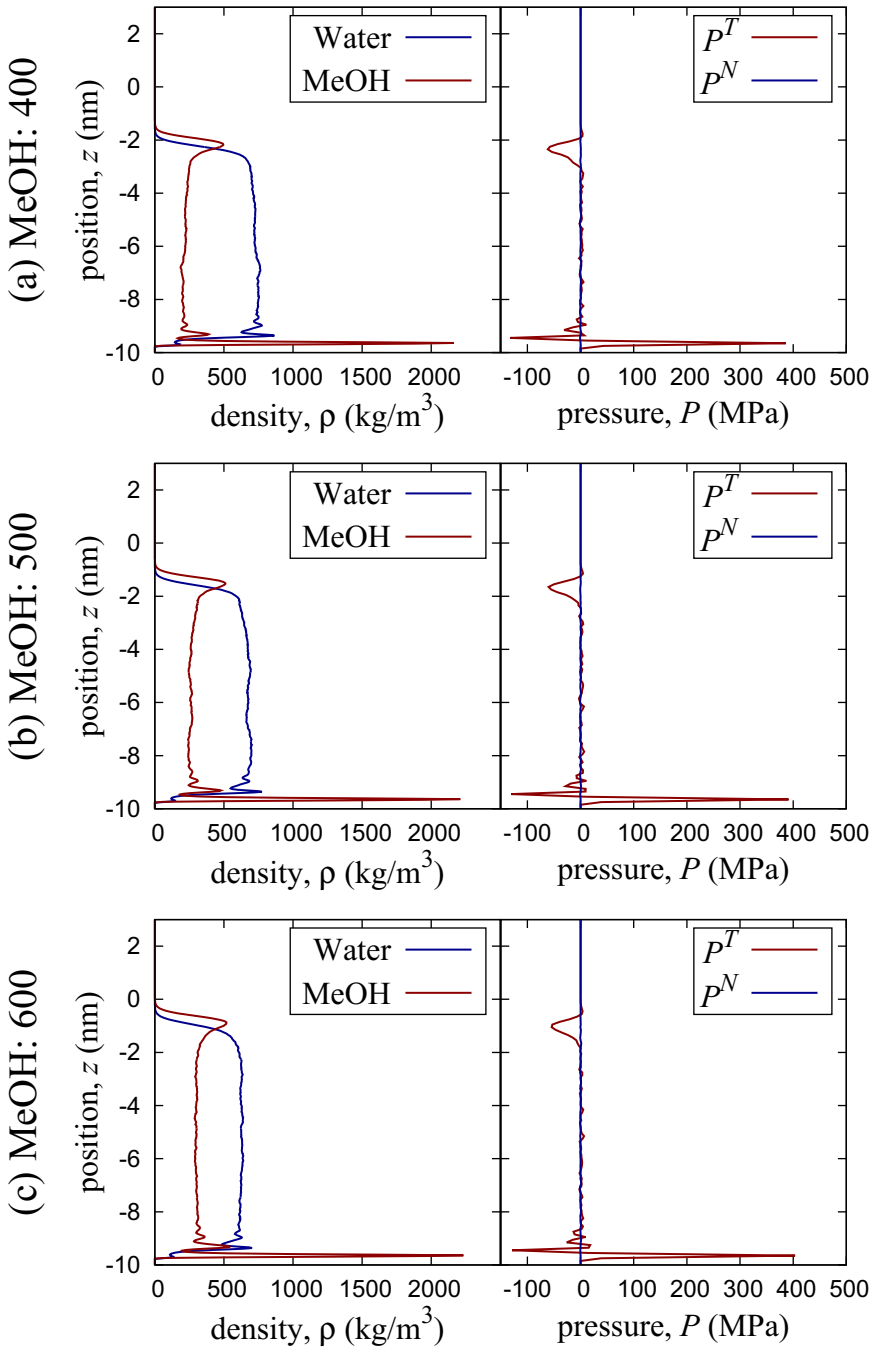

Figure 4.5: Density and pressure distributions of water-methanol mixture layers in systems composed of 1800 water and 400, 500 or 600 methanol molecules.

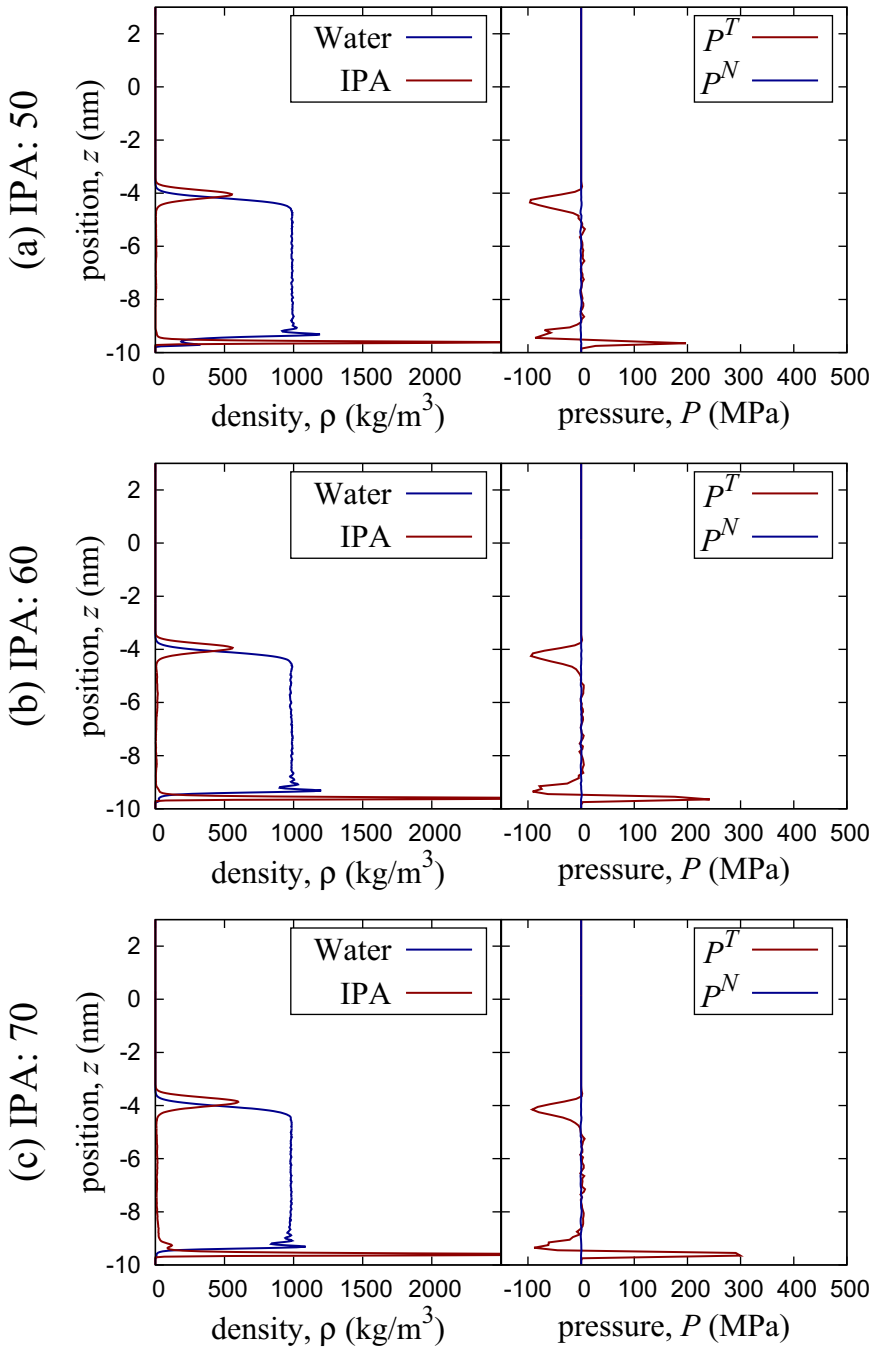

Figure 4.6: Density and pressure distributions of water-IPA mixture layers in systems composed of 1800 water and 50, 60 or 70 IPA molecules.

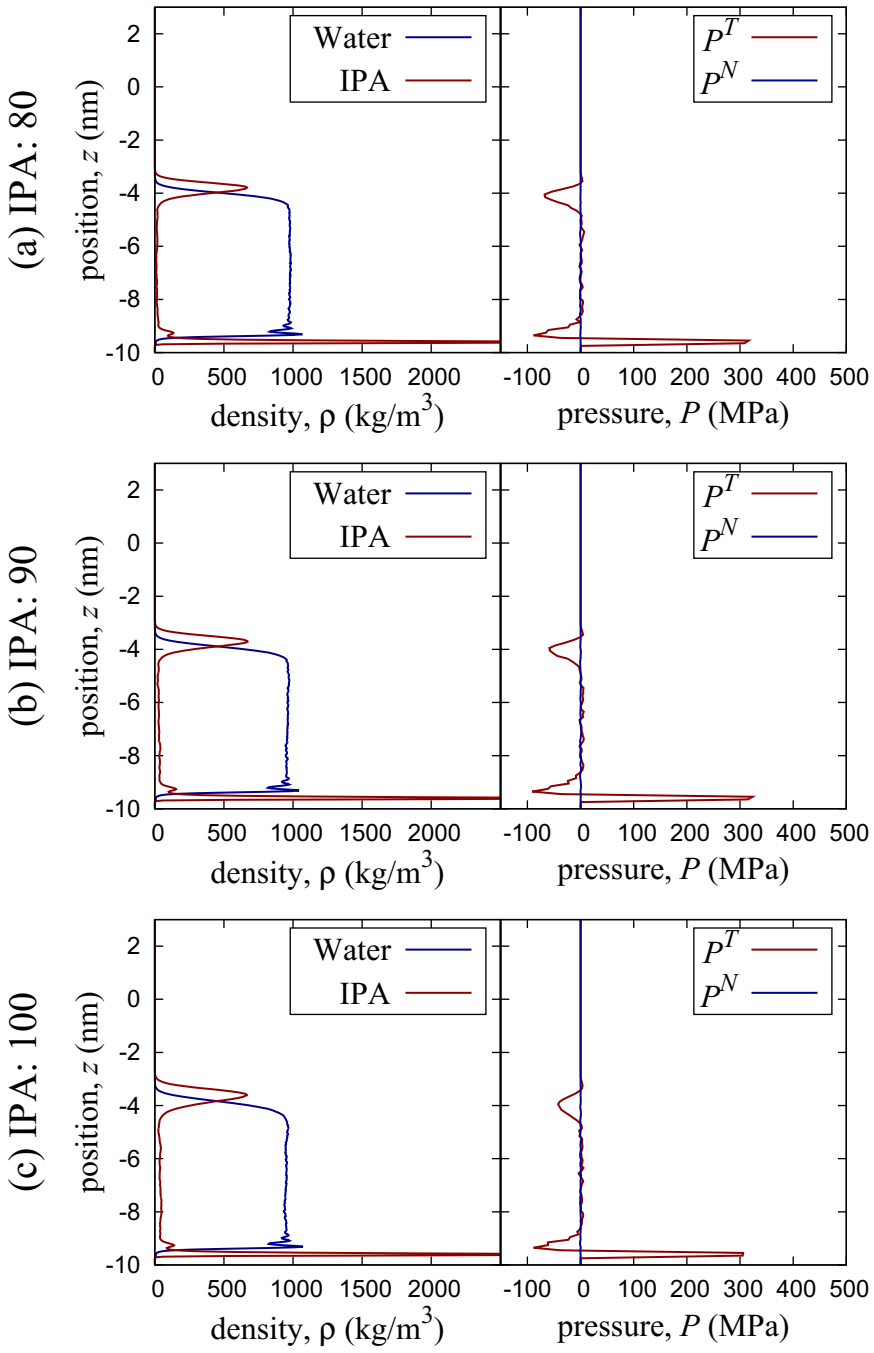

Figure 4.7: Density and pressure distributions of water-IPA mixture layers in systems composed of 1800 water and 80, 90 or 100 IPA molecules.

4.3 Molecular Orientations

In this section, molecular orientations are investigated at the solid-liquid and liquid-vapor interfaces for systems such as in Fig. 4.1.

The angles between the z-axis and two different bonds are selected for each molecule and their two-dimensional probability distributions are calculated. The selected angles are two $\angle\vec{n}^z$O–H for each hydrogen atom in a water molecule, $\angle\vec{n}^z$O–H and $\angle\vec{n}^z$O–CH_3 for a methanol molecule, and $\angle\vec{n}^z$O–H and $\angle\vec{n}^z$O–CH for an IPA molecule, where $\vec{n}^z$ is the unit vector to $+z$ direction. Because systems in Fig. 4.1 are quasi-one-dimensional, the molecular orientations are axially symmetric in regards to the z-axis, thus two variables are enough to fully describe the three-dimensional orientation of rigid molecules.

Even completely isotropic distribution of a single unit vector would not produce an uniform probability, but be proportional to the sine of the angle, because more states can be occupied at angles closer to 90 degrees. To remove this bias, an unweighted probability distribution made from isotropic molecular orientations is used to weight other probability distribution graphs. Isotropic molecular orientations are obtained by randomly generating 1×10^{10} uniform orientations for water and methanol, and 2×10^{10} uniform orientations for IPA molecules.

4.3.1 Single-component systems

The solid-liquid and liquid-vapor interface regions are determined from the density distribution graphs in Fig. 4.3. The density peak nearest to the solid surface is used to investigate the orientations in the solid-liquid interfaces and the liquid-vapor interfaces are set as -5.5 nm $\leq z \leq -4$ nm, -5 nm $\leq z \leq -3.5$ nm and -4.5 nm $\leq z \leq -2.5$ nm for single-component water, methanol and IPA systems, respectively.

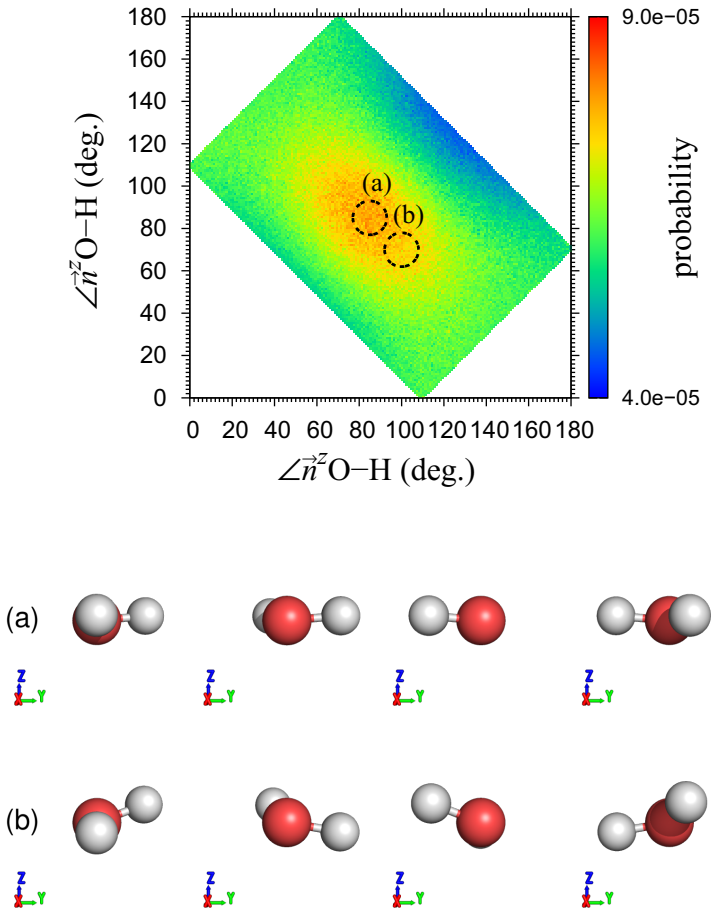

Figure 4.8: (Top) probability distribution of angular configurations in the liquid-vapor interface of single-component water system. (Bottom) molecular orientations seen from various angles corresponding to the areas marked in the probability distribution graph.

4.3.1.1 single-component water

The probability distribution graph of angular configurations in the liquid-vapor interface of single-component water system is shown in the top panel of Fig. 4.8. The angular distribution is spread out, with most probability in 60 deg. $\leq \angle\vec{n}^z$O–H$\leq$ 100 deg., corresponding to water molecules directing their O–H bonds almost parallel to the liquid-vapor interface, with hydrogen atoms pointing slightly to the vapor phase. Two preferable orientations are displayed in Fig. 4.8 (a, b). This would mean that the liquid-vapor interface is slightly polarized outwards, which is in accordance with a previous research.[57]

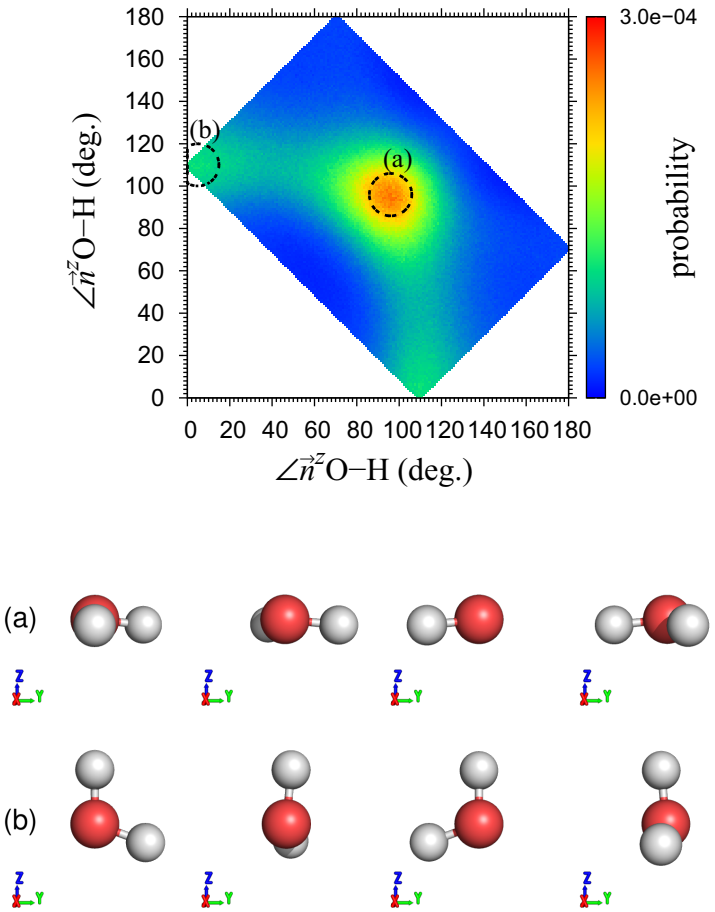

Figure 4.9: (Top) probability distribution of angular configurations in the density peak nearest to the solid-liquid interface of single-component water system. (Bottom) molecular orientations seen from various angles corresponding to the areas marked in the probability distribution graph.

The probability distribution graph of angular configurations in the density peak nearest to the solid surface of single-component water systems is shown in the top panel of Fig. 4.9. Unlike that of the liquid-vapor interface in Fig. 4.8, molecules in this region are much more strongly oriented, although this has much to do with the fact that Fig. 4.8 also includes bulk information. Most orientations are close to that shown in Fig. 4.9 (a) and slightly downward polarized. It is also clear that a small fraction of molecules direct their hydrogen atom upward from the solid surface to create an orientation similar to Fig. 4.9 (b). This can be interpreted as either trying to create hydrogen bond with above positioned molecules, or trying to mitigate the downward polarization caused by the dominant orientation. The orientations shown in Fig. 4.8 (a) and Fig. 4.9 (a) are almost a mirror image of each other in regards to the xy-plane

and might suggest that solid-liquid and liquid-vapor interfaces are similar structurally, and that the non-polar solid surface only creates density oscillation at the solid-liquid interface.

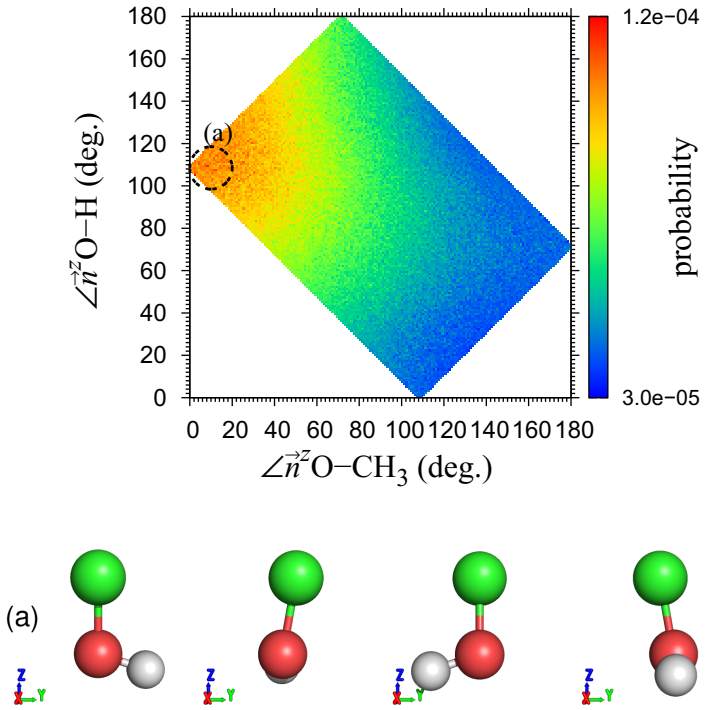

Figure 4.10: (Top) probability distribution of angular configurations in the liquid-vapor interface of single-component methanol system. (Bottom) molecular orientations seen from various angles corresponding to the area marked in the probability distribution graph.

4.3.1.2 single-component methanol

The probability distribution graph of angular configurations in the liquid-vapor interface of single-component methanol system is shown in the top panel of Fig. 4.10. The probability distribution is highly biased and there is only one dominating orientation where the methyl groups are directed to the vapor phase as shown in Fig. 4.10 (a). This happens because the hydroxyl groups are directed to the liquid bulk to create hydrogen bonds. Although the hydrogen atoms are directed towards the liquid bulk, the liquid-vapor interface is still upward polarized similarly to the liquid-vapor interface of single-component water shown in Fig. 4.8, because the methyl groups also have a positive charge.

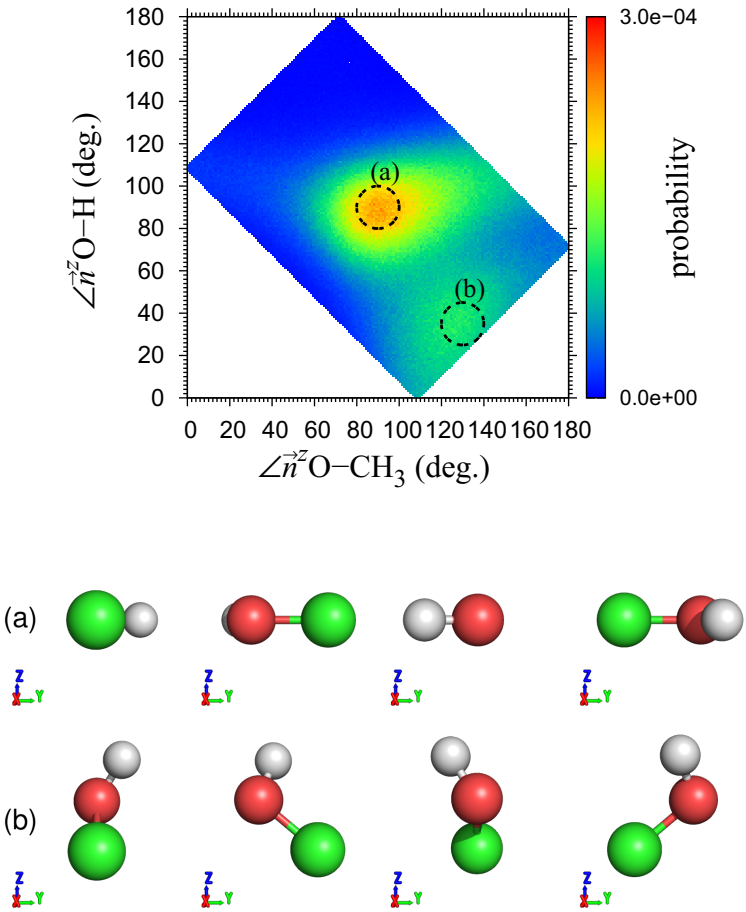

Figure 4.11: (Top) probability distribution of angular configurations in the density peak nearest to the solid-liquid interface of single-component methanol system. (Bottom) molecular orientations seen from various angles corresponding to the areas marked in the probability distribution graph.

The probability distribution graph of angular configurations in the density peak nearest to the solid surface of single-component methanol systems is shown in the top panel of Fig. 4.11. Unlike in the liquid-vapor interface shown in Fig. 4.10, there are two distinguishable orientations, and neither one of them corresponds to one observed in the liquid-vapor interface. This contrasts with the similar orientations that were observed for water in liquid-vapor and solid-liquid interfaces in Figs. 4.8 and 4.9, and is thought to occur because there is only a single L-J interaction site in the SPC/E water model, therefore the solid surface has little effect on the molecular orientations, while there are two interaction sites in the OPLS-UA methanol model and thus molecular orientations are more easily affected. In the dominant orientation shown in Fig. 4.11 (a), methanol has both of its O–CH_3 and O–H bonds almost parallel to the solid-liquid interface. The

less dominant orientation is with the methyl group pointing towards the solid surface, whilst the hydrogen atom is directed upward. This allows the molecules to create hydrogen bonds with other molecules further inside the bulk.

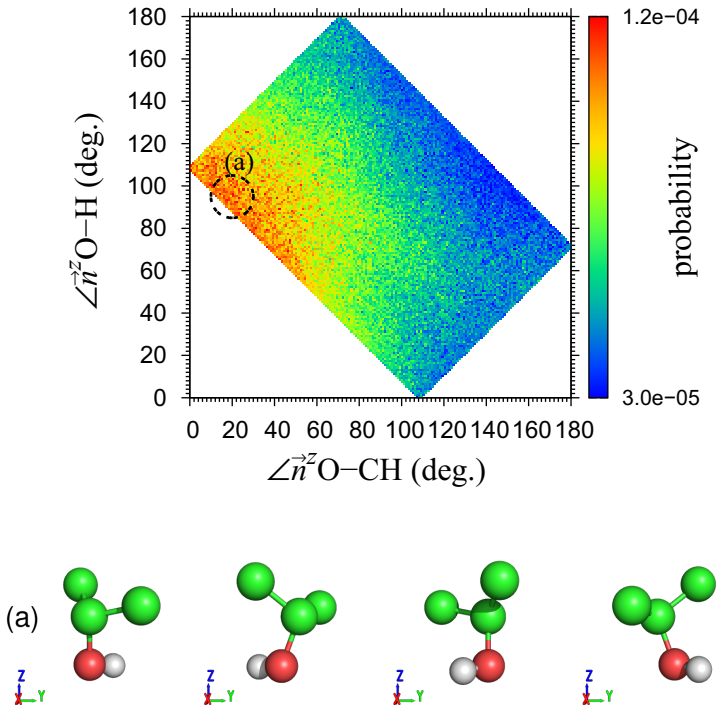

Figure 4.12: (Top) probability distribution of IPA trans conformer angular configurations in the liquid-vapor interface of single-component IPA system. (Bottom) molecular orientations seen from various angles corresponding to the area marked in the probability distribution graph.

4.3.1.3 single-component IPA

Because IPA liquid in this work is composed of a mixture of three conformers shown in Fig. 2.4, some extra steps must be taken for calculating the probability distribution of angular configurations. Most importantly, extra care should be taken when handling the gauche conformers shown in Fig. 2.4 (a), because unlike water and methanol molecules, IPA gauche conformer molecules do not have a plane of symmetry. Specifically, even the same $\angle\vec{n}^z$O–H and $\angle\vec{n}^z$O–CH values correspond to different orientations depending on if the O–CH and O–H bonds are positioned clockwise or counterclockwise in respect to the z-axis. To take this into account, $\angle\vec{n}^z$O–CH is given a negative value when O–H is positioned counterclockwise to O–CH. Because the two gauche conformers are mirror

images of each other and basically equivalent, their results are combined and shown as the distribution of the conformer corresponding to the right panel of Fig. 2.4 (a).

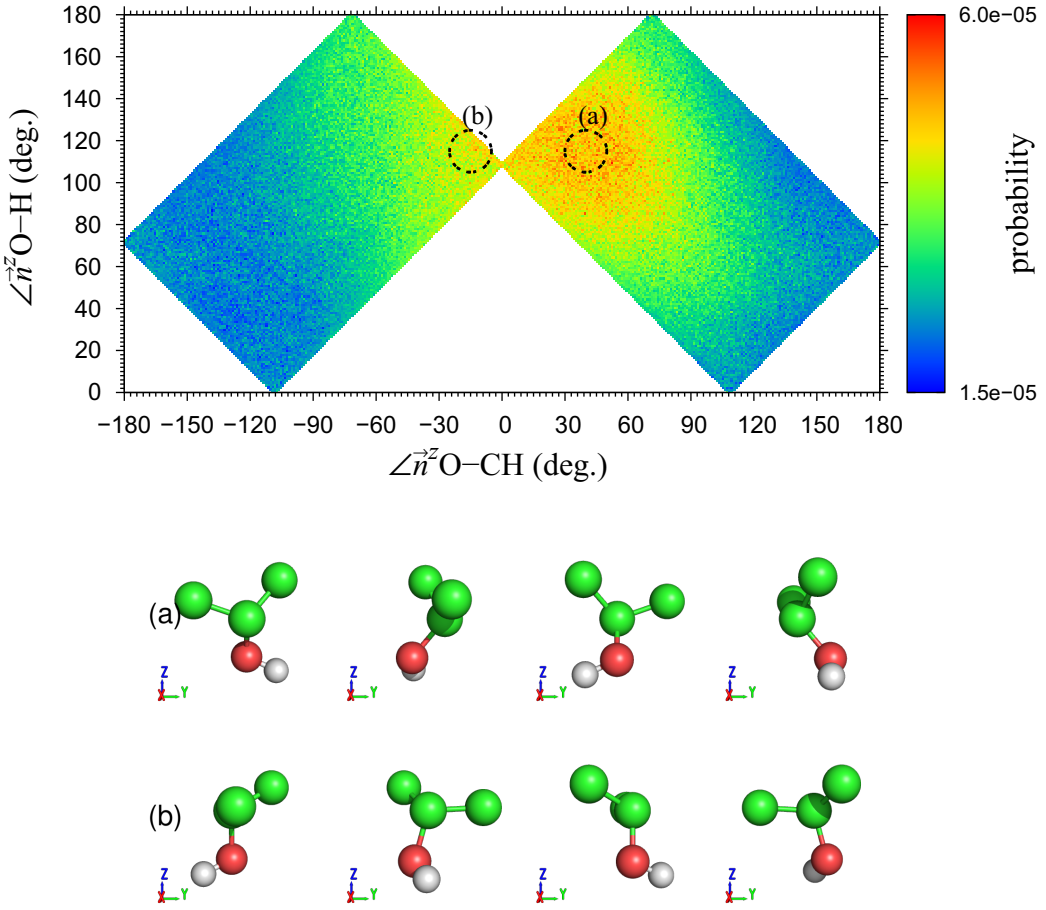

Figure 4.13: (Top) probability distribution of IPA gauche conformer angular configurations in the liquid-vapor interface of single-component IPA system. (Bottom) molecular orientations seen from various angles corresponding to the areas marked in the probability distribution graph.

The probability distribution graphs of angular configurations in the liquid-vapor interface of single-component IPA system are shown in the top panels of Figs. 4.12 and 4.13 for the trans and gauche conformers, respectively. Take note that because Fig. 4.12 does not make a distinction between the bond clockwiseness of the trans conformer, the probability density is roughly two times larger than that in Fig. 4.13 for the gauche conformer. In both of these graphs, the probabilities are highly biased and the main orientations illustrated in Figs. 4.12 (a) and 4.13 (a, b) have the methyl groups pointing upward to the vapor phase, which is comparable to that of the liquid-vapor interface of single-component methanol system shown in Fig. 4.10. There is also some upward

polarization due to a positive charge in the CH group, which is also comparable to what was observed for single-component methanol system. Therefore, it is safe to assume that the liquid-vapor interfaces of methanol and IPA are somewhat similar.

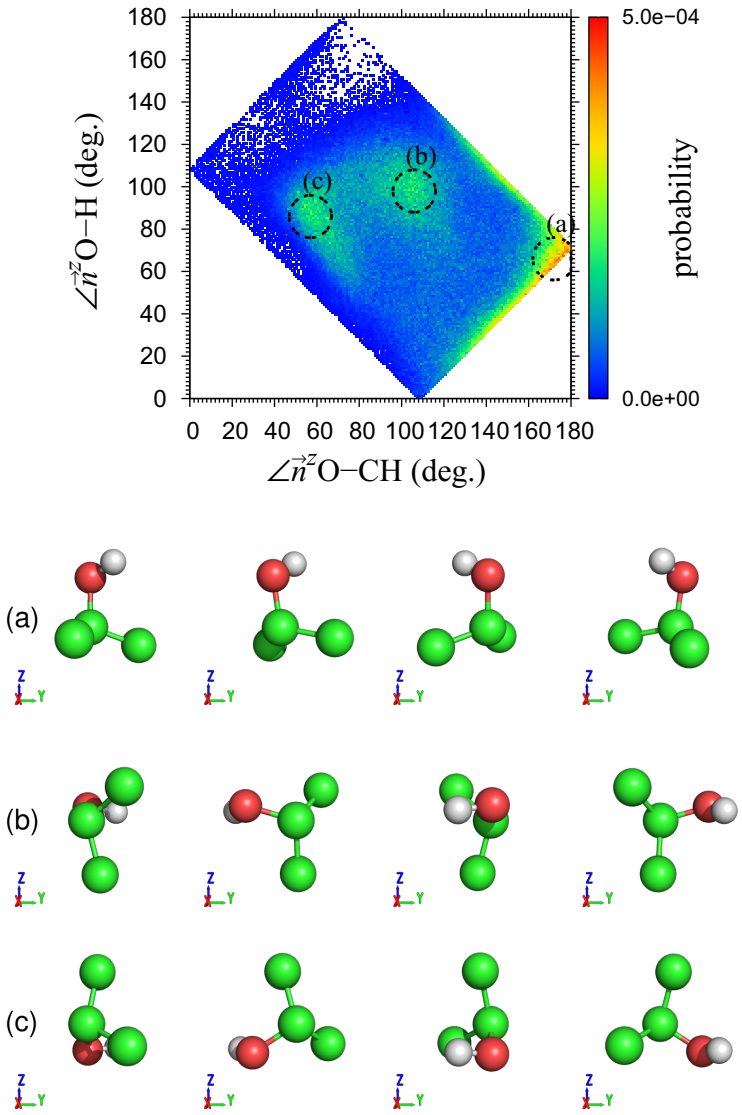

Figure 4.14: (Top) probability distribution of IPA trans conformer angular configurations in the density peak nearest to the solid-liquid interface of single-component IPA system. (Bottom) molecular orientations seen from various angles corresponding to the areas marked in the probability distribution graph.

The probability distribution graphs of angular configurations in the density peak nearest to the solid surface of single-component methanol systems are shown in the top panels of Figs. 4.14 and 4.15 for the trans and gauche conformers, respectively. Unlike for the liquid-vapor interface shown in Figs. 4.12 and 4.13, the trans and gauche

confronters appear to take different orientations, which are also different from what was observed in the case of methanol in Fig. 4.11. The trans conformer has a clear dominant orientation shown in Fig. 4.14 (a), where the methyl groups point downward to the solid surface and the hydroxyl groups point upward to the bulk. There are also less dominant orientations displayed in Fig. 4.14 (b, c), where one methyl group is pointing downward and the other upward, with the O–H bond more or less parallel to the interface. These orientations appear mostly separate from each other, with little interchange between the different states. On the other hand, the orientations of the gauche conformer displayed in Fig. 4.15 show a completely different situation. There appear to be numerous orientations, some of them illustrated in Fig. 4.15 (a, b, c, d, e), with transitional orientations of slightly lower probability interconnecting the dominant ones. The orientation with methyl groups pointing downward to the solid surface and hydroxyl groups pointing upward to the liquid bulk shown in Fig. 4.15 (a) appears to be slightly more dominant than the others, and this does somewhat correspond to the dominant orientation of the trans conformer in the same region displayed in Fig. 4.14 (a), but other orientations and the transition among them is unique to the gauche conformer. The position of the hydrogen atom is the only difference between the conformers, but it appears to be enough to cause vastly different interfacial structures, where the trans conformer seems to be more tightly constrained than the gauche one.

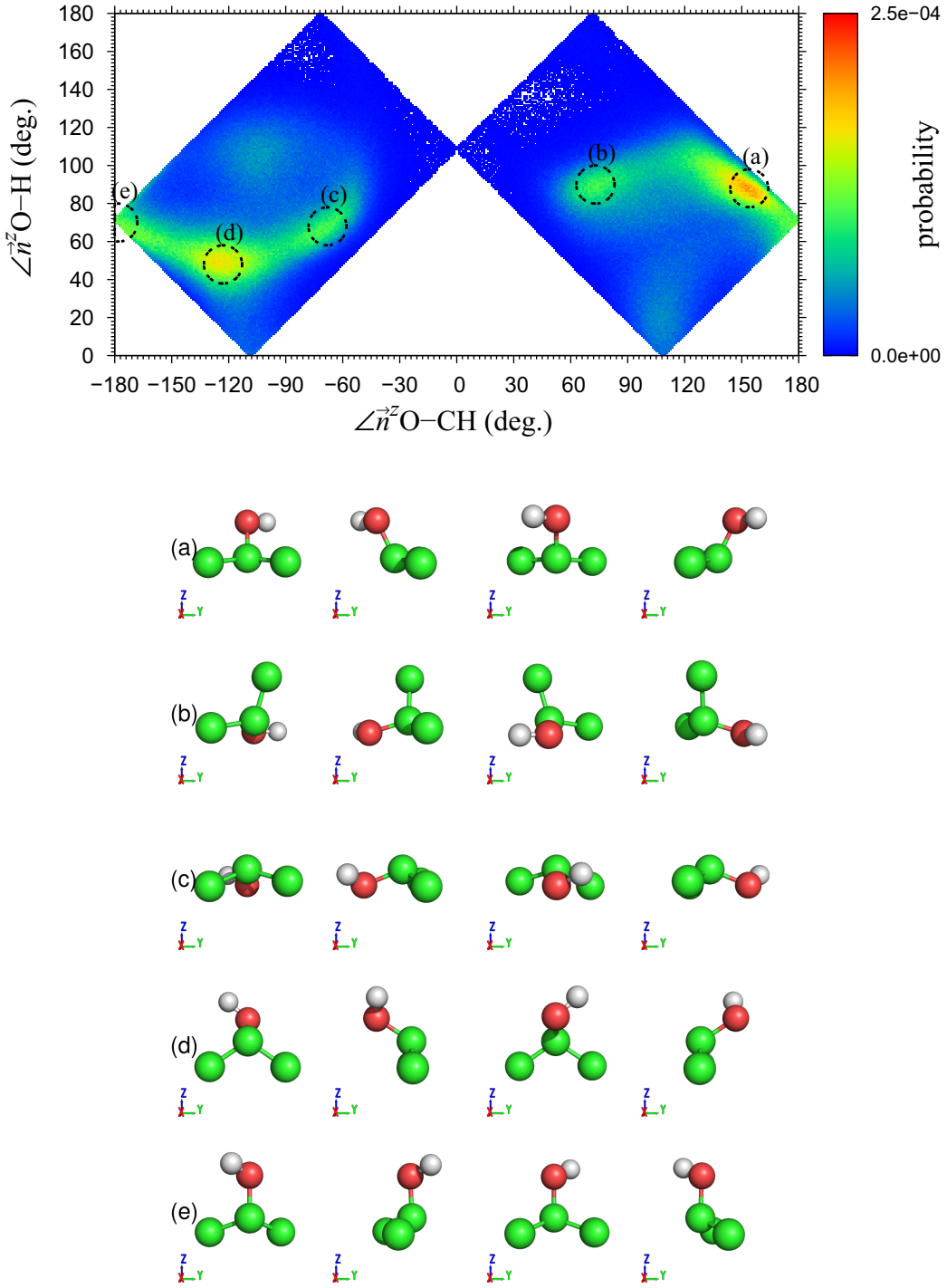

Figure 4.15: (Top) probability distribution of IPA gauche conformer angular configurations in the density peak nearest to the solid-liquid interface of single-component IPA system. (Bottom) molecular orientations seen from various angles corresponding to the areas marked in the probability distribution graph.

4.3.2 Water-methanol mixture

As with single-component systems in Section 4.3.1, the density distribution graphs in Figs. 4.4 and 4.5 are used to determine the regions to investigate the molecular orientations in solid-liquid and liquid-vapor interfaces. The density peak nearest to the solid surface is chosen as the region to investigate the solid-liquid interface. Take note that the density peaks for water and methanol are slightly misaligned, therefore the regions used for water and methanol molecular orientations are slightly different. The liquid-vapor region is chosen to fully enclose the methanol peak at the interface, and the same region is used for both water and methanol components.

The probability distribution graphs of water and methanol angular configurations in liquid-vapor interfaces of water-methanol mixture systems are shown in Figs. 4.16 and 4.17, respectively, where single-component graphs from Figs. 4.8 and 4.10 are also included for reference. As shown in Fig. 4.16, water does not show much change in its structure overall, and only a greater spreading in the water orientation distribution with the increase of methanol concentration is observed. This might be due to the fact that the liquid-vapor interface is primary covered with methanol molecules, therefore water orientations become closer to those in the bulk. It is interesting to note that at a very low methanol concentration shown in Fig. 4.16 (b), water appears to be more strongly oriented and polarized than that in the single-component system, although this is not certain due to different methods of selecting the analysis regions. Much greater change is observed in methanol orientations shown in Fig. 4.17, where the distribution becomes diffused with the increase of methanol concentration, although the dominant orientation shown in Fig. 4.10 (a) remains unchanged. This is thought to be due to the fact that the dominant orientation is advantageous in creating hydrogen bonds with the molecules inside the bulk, and therefore is more prominent when the bulk is mostly composed of water molecules, which can create more hydrogen bonds than methanol molecules.

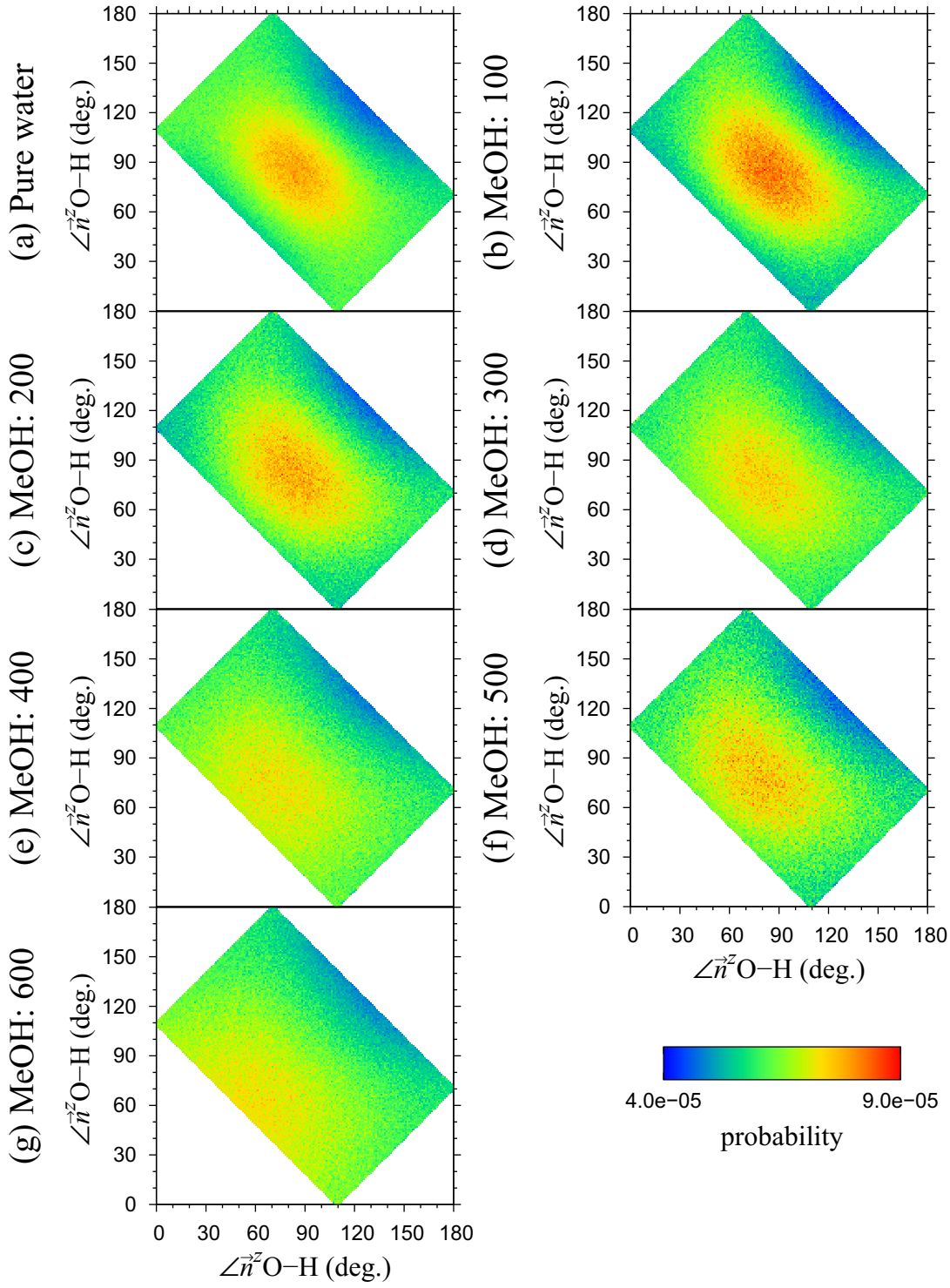

Figure 4.16: Probability distributions of water angular configurations in the liquid-vapor interface of water-methanol mixture systems. Single-component system is also included for reference.

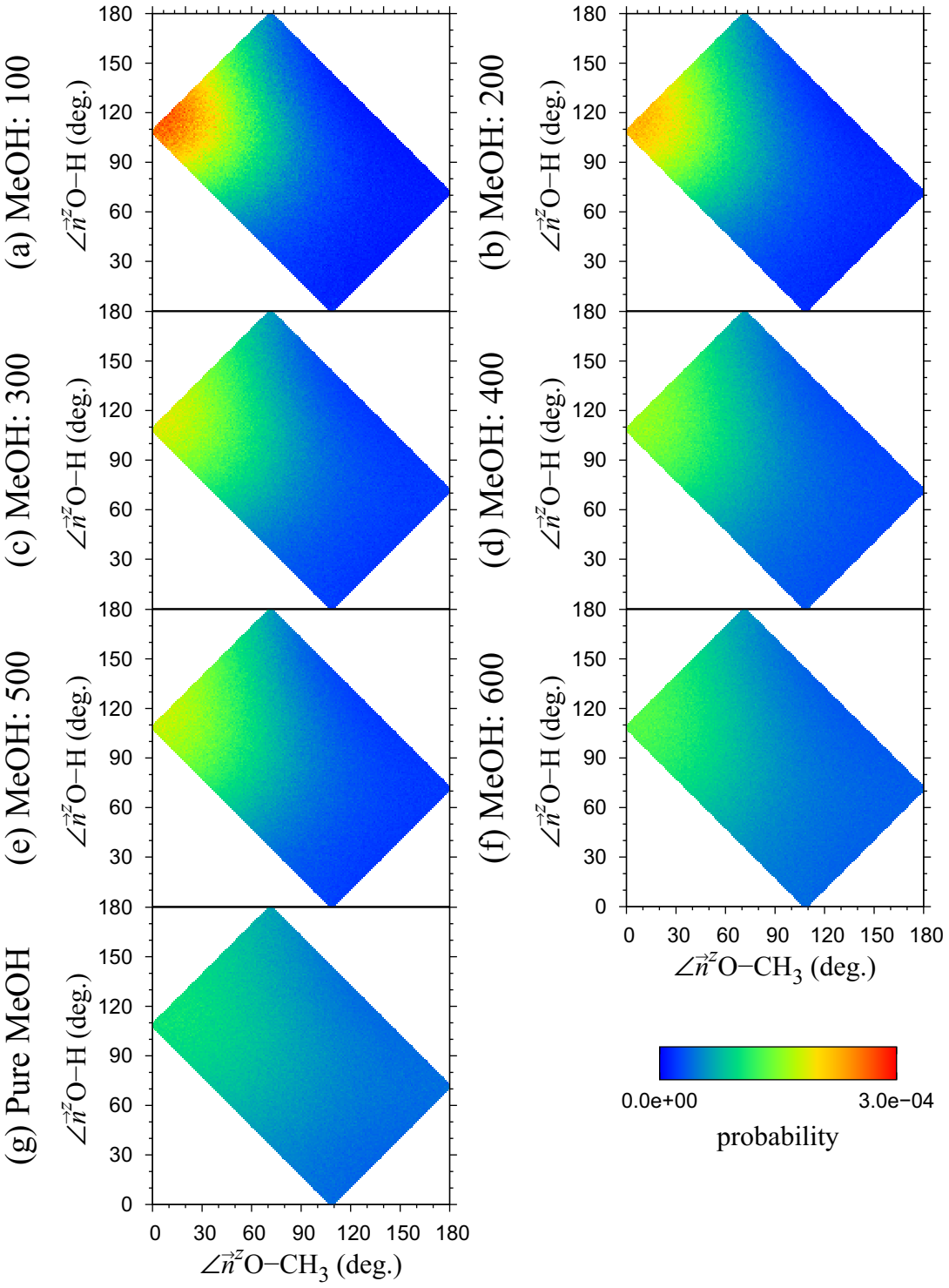

Figure 4.17: Probability distributions of methanol angular configurations in the liquid-vapor interface of water-methanol mixture systems. Single-component system is also included for reference.

The probability distribution graphs of water and methanol angular configurations are shown in Figs. 4.18 and 4.19, respectively, for the density peaks nearest to the solid surface where single-component graphs from Figs. 4.9 and 4.11 are also included for reference. Surprisingly, water displayed in Fig. 4.18 shows almost no change in orientations, even though there are very few water molecules in the first density peak at higher methanol concentrations as seen in Fig. 4.5. Thus it seems that water molecules themselves do not behave differently if water molecules are replaced with methanol at the solid-liquid interface. On the other hand, orientations of methanol molecules illustrated in Fig. 4.19 show a more distinct change. Overall, the same two orientations seen in single-component methanol system shown in Fig. 4.11 (a, b) are present, but all are equally dominant, except for the system with a very low methanol concentration shown in Fig. 4.19 (a) which is more similar to single-component methanol system. The existence of water molecules inside mixture systems allows the methanol molecules inside the first density peak to create more hydrogen bonds, therefore the orientation with the hydroxyl group pointing upward shown in Fig. 4.11 (b) is more suited for it and becomes more prominent. The unique feature seen in Fig. 4.19 (a) can be explained by an abundant amount of water molecules in the first density peak, as seen from the density distribution in the left panel of Fig. 4.4 (a), which would suggest that the extra hydrogen bonds are taken up by water molecules in the adsorption layer, therefore the change in methanol orientations is not as dramatic.

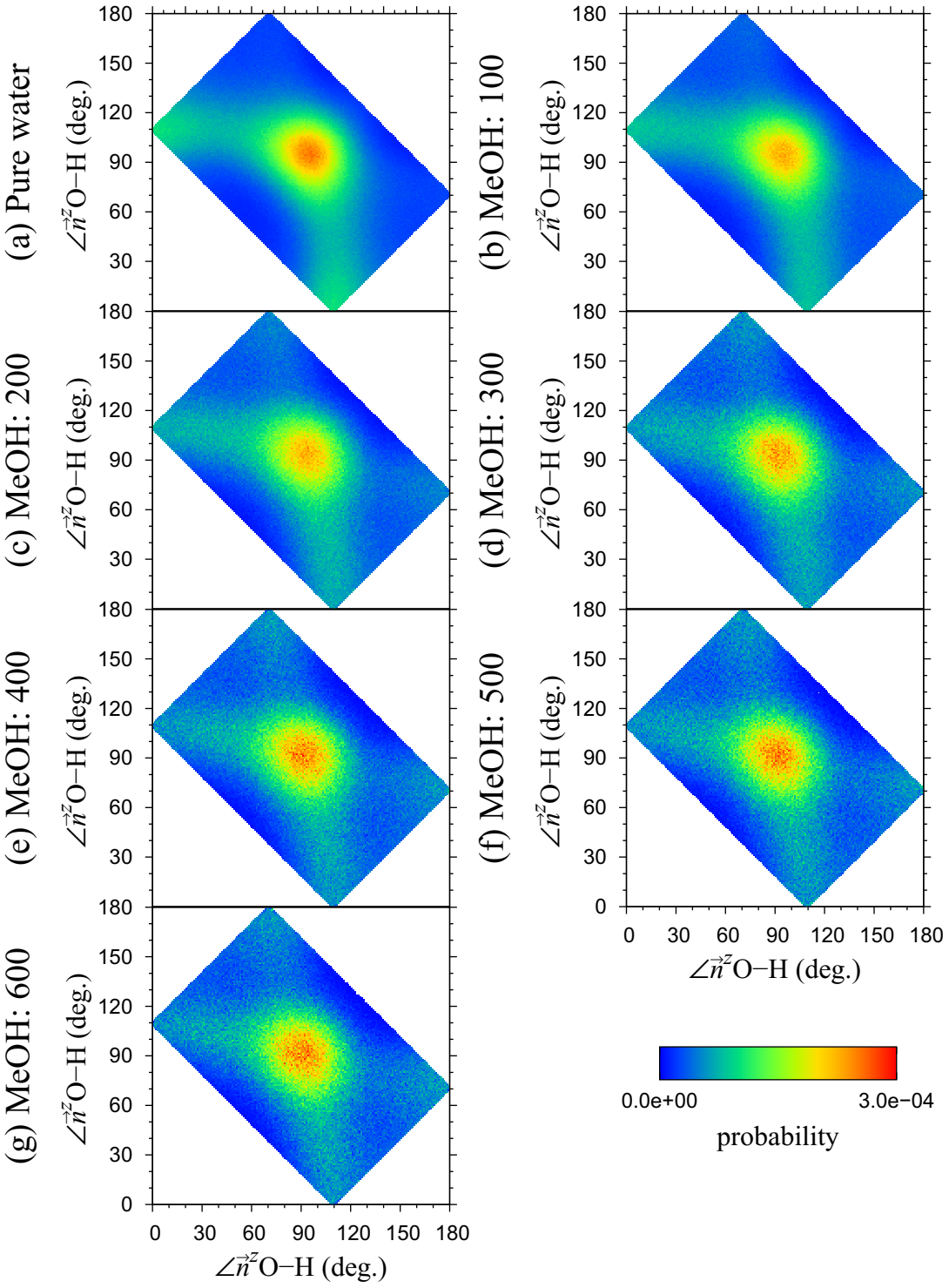

Figure 4.18: Probability distributions of water angular configurations in the density peak nearest to the solid-liquid interface of water-methanol mixture systems. Single-component system is also included for reference.

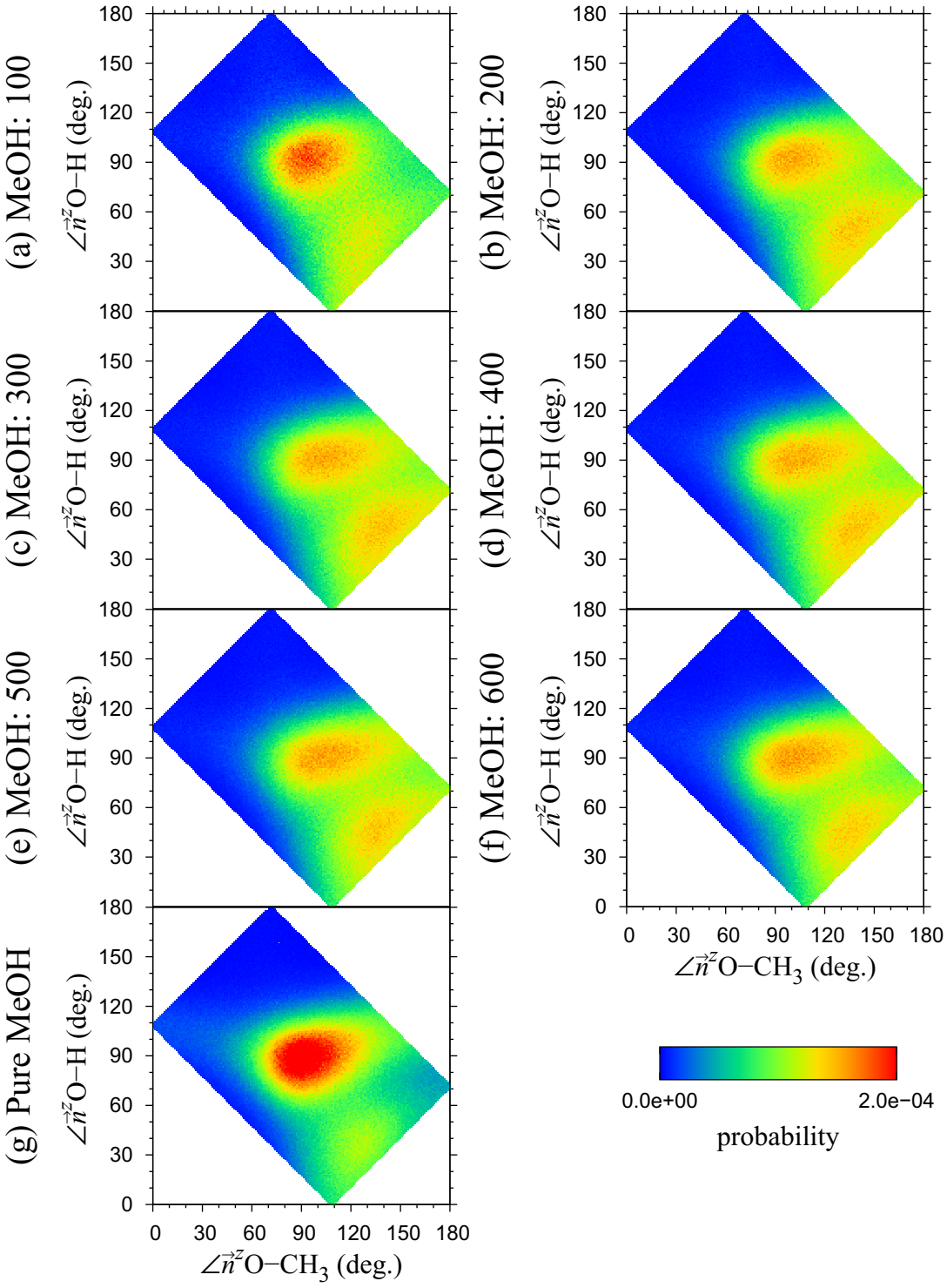

Figure 4.19: Probability distributions of methanol angular configurations in the density peak nearest to the solid-liquid interface of water-methanol mixture systems. Single-component system is also included for reference.

4.3.3 Water-IPA mixture

As with water-methanol systems in Section 4.3.2, the density distribution graphs in Figs. 4.6 and 4.7 are used to determine the regions to investigate the molecular orientations in solid-liquid and liquid-vapor interfaces. For the solid-liquid interface, the regions are chosen to encompass the first IPA density peaks at the solid-liquid interface. The molecular orientations of water are not investigated because no density peak exists as seen in Fig. 4.7. The liquid-vapor region is chosen to fully enclose the IPA peak at the liquid-vapor interface, and the same region is used for both water and IPA components.

The probability distribution graphs of angular configurations of water, IPA trans conformer and IPA gauche conformer in liquid-vapor interfaces of water-IPA mixture systems are shown in Figs. 4.20, 4.21 and 4.22, respectively, where single-component graphs from Figs. 4.8, 4.12 and 4.13 are also included for reference. As displayed in Fig. 4.20, water does not show much change in its structure overall and, similarly to that observed in water-methanol systems in Fig. 4.16, only a greater diffusion in the orientation distribution with the increase of IPA concentration is observed. It is interesting to note that in two systems shown in Fig. 4.20 (c, d), water appears to be more strongly oriented and polarized than that in any other systems, although it is difficult to say if it is indeed the case or this simply comes from the uncertainty in the methods of selecting the analysis regions. As with methanol in water-methanol systems in Fig. 4.17, much greater change is observed in IPA orientations as shown in Figs. 4.21 and 4.22, where orientations are diffused greatly with the increase of IPA concentration, although the dominant orientations remain unchanged. The same explanation can be given as that for the methanol molecules in the water-methanol mixture systems, i.e. greater amount of water molecules inside liquid bulk provides more hydrogen bonds, leading to stronger orientations.

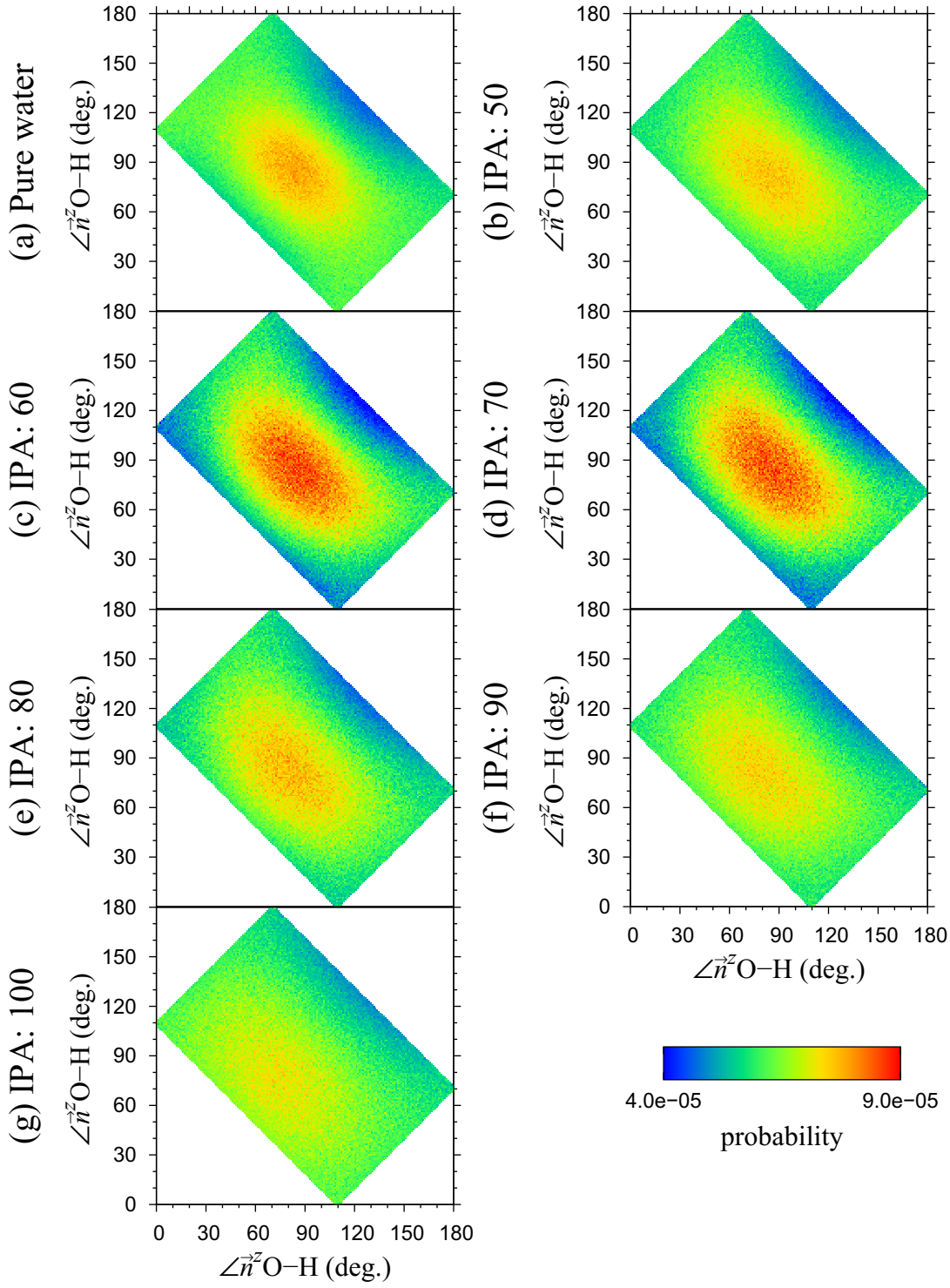

Figure 4.20: Probability distributions of water angular configurations in the liquid-vapor interface of water-IPA mixture systems. Single-component system is also included for reference.

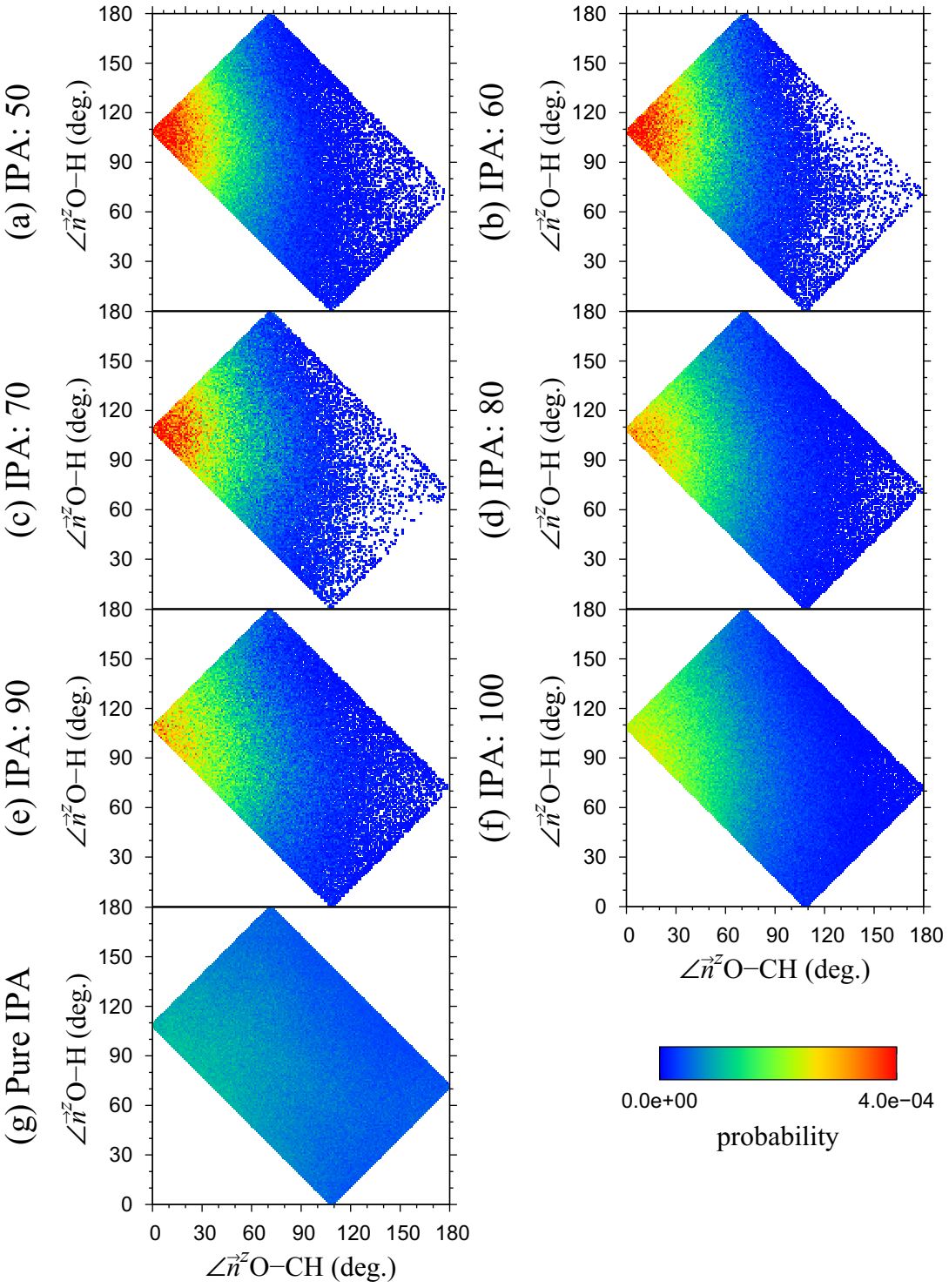

Figure 4.21: Probability distributions of angular configurations of IPA trans conformer in the liquid-vapor interface of water-IPA mixture systems. Single-component system is also included for reference.

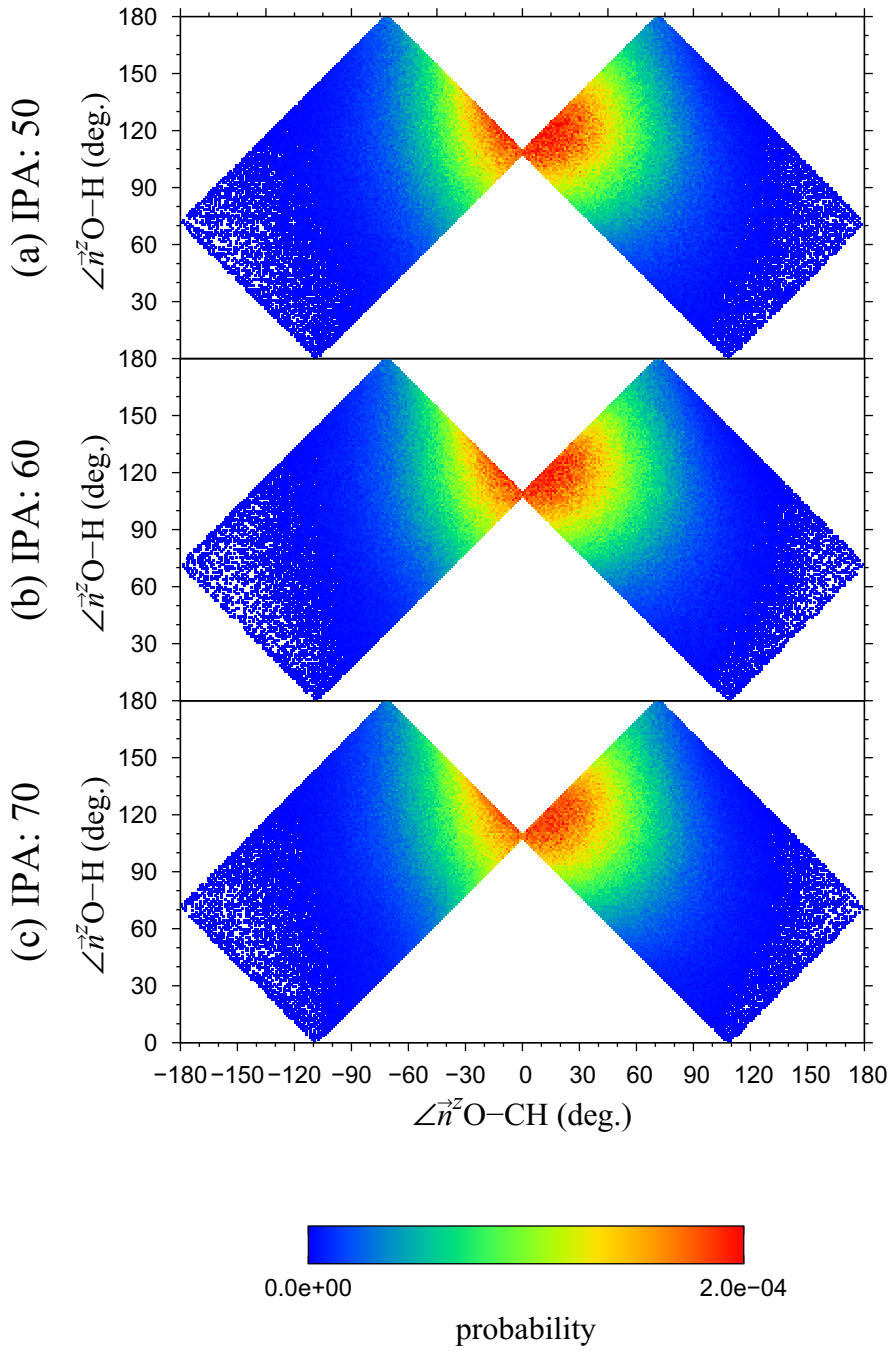

Figure 4.22: Probability distributions of angular configurations of IPA gauche conformer in the liquid-vapor interface of water-IPA mixture systems (continue).

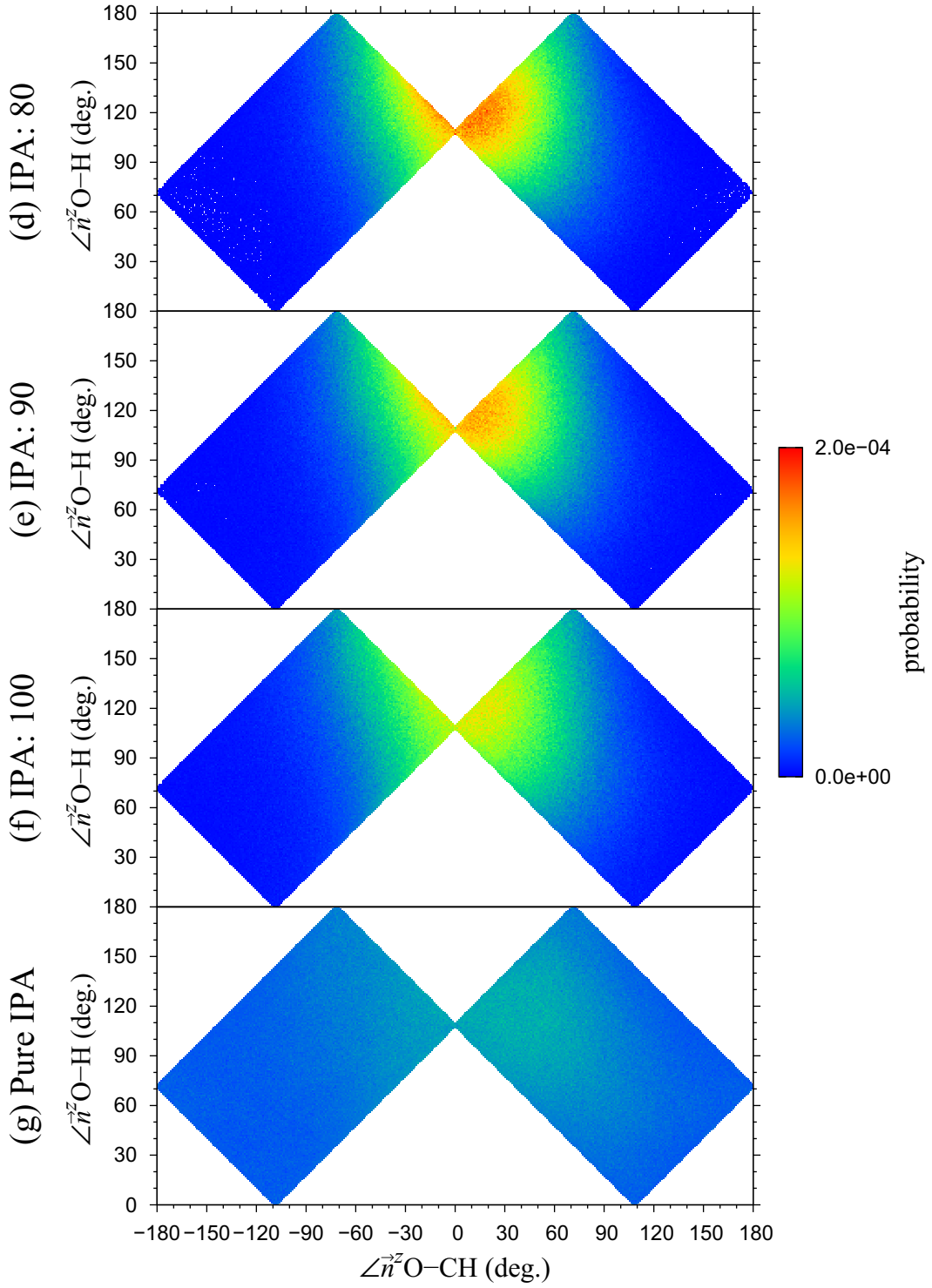

Figure 4.22: (Continued) probability distributions of angular configurations of IPA gauche conformer in the liquid-vapor interface of water-IPA mixture systems. Single-component system is also included for reference.

The probability distribution graphs of angular configurations of IPA trans and IPA gauche conformers in the density peaks nearest to the solid surface of water-IPA mixture systems are shown in Figs. 4.23 and 4.24, respectively, where single-component graphs from Figs. 4.14 and 4.15 are also included for reference. Observing the orientations of the trans conformer, it can be seen that only the dominant orientation from the single-component IPA system shown in Fig. 4.14 (a) remains visible, while the lesser ones shown in Fig. 4.14 (b, c) are no longer prominent. On the other hand, in the case of the gauche conformer, the dominating orientation changes from Fig. 4.15 (a, b) in single-component IPA to Fig. 4.15 (e) inside water-IPA mixture, where there are also seemingly less transitional states between the various orientations. The dominant orientations of both conformers have the methyl groups pointing downward to the solid surface, and hydroxyl groups pointing upward to the liquid bulk, implying eagerness to create hydrogen bonds with water molecules positioned above them, and resulting in much stronger orientations than in single-component systems. On the other hand, the strength of orientations appears at the same level for different IPA concentrations. This is related to the fact that the IPA molecules in the analysed systems do not diffuse into the bulk, and thus, a change in concentration mostly implies only the increase of molecules inside the interfaces, leaving the bulk consisting of mostly water molecules.

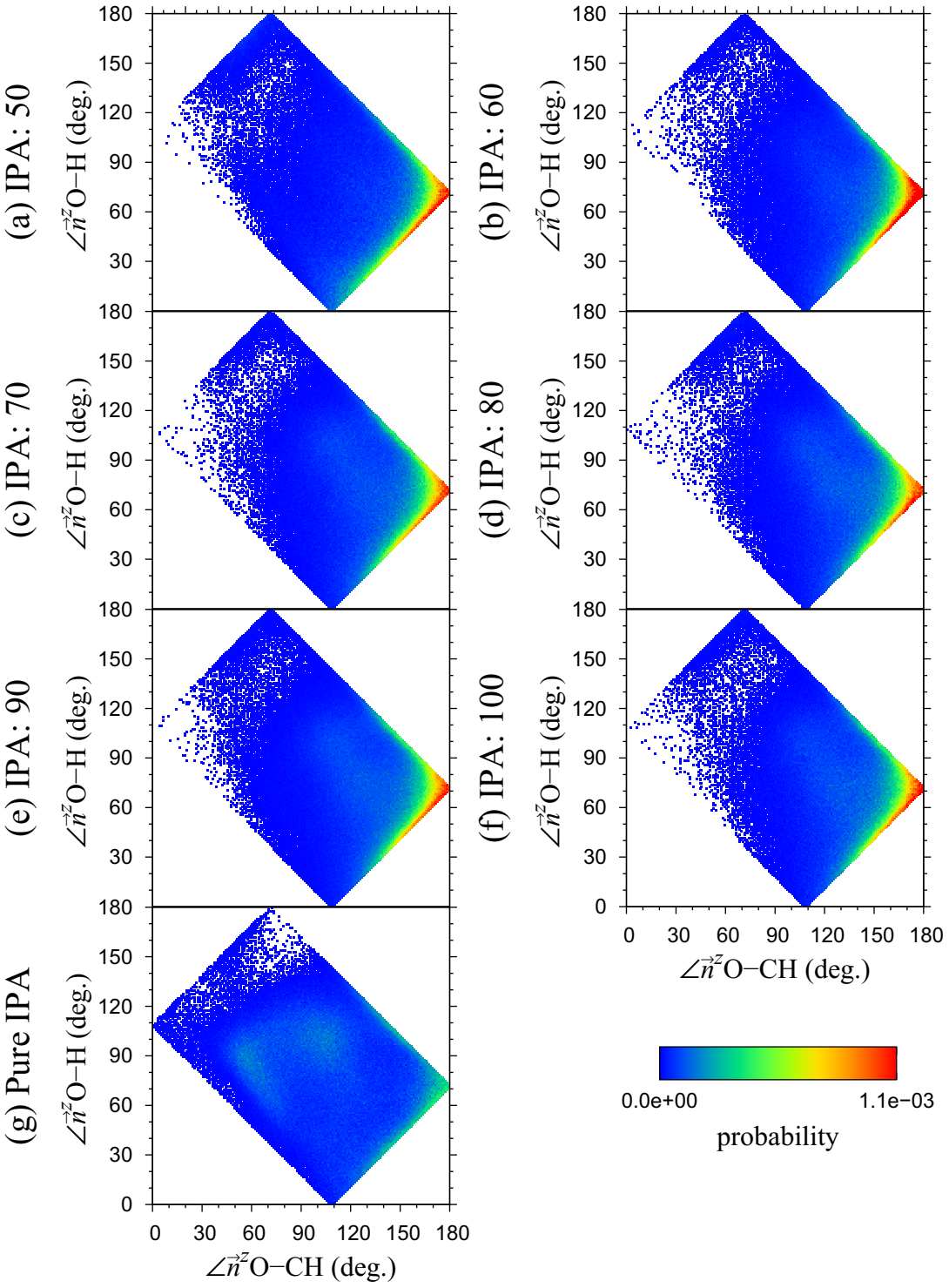

Figure 4.23: Probability distributions of angular configurations of IPA trans conformer in the density peak nearest to the solid-liquid interface of water-IPA mixture systems. Single-component system is also included for reference.

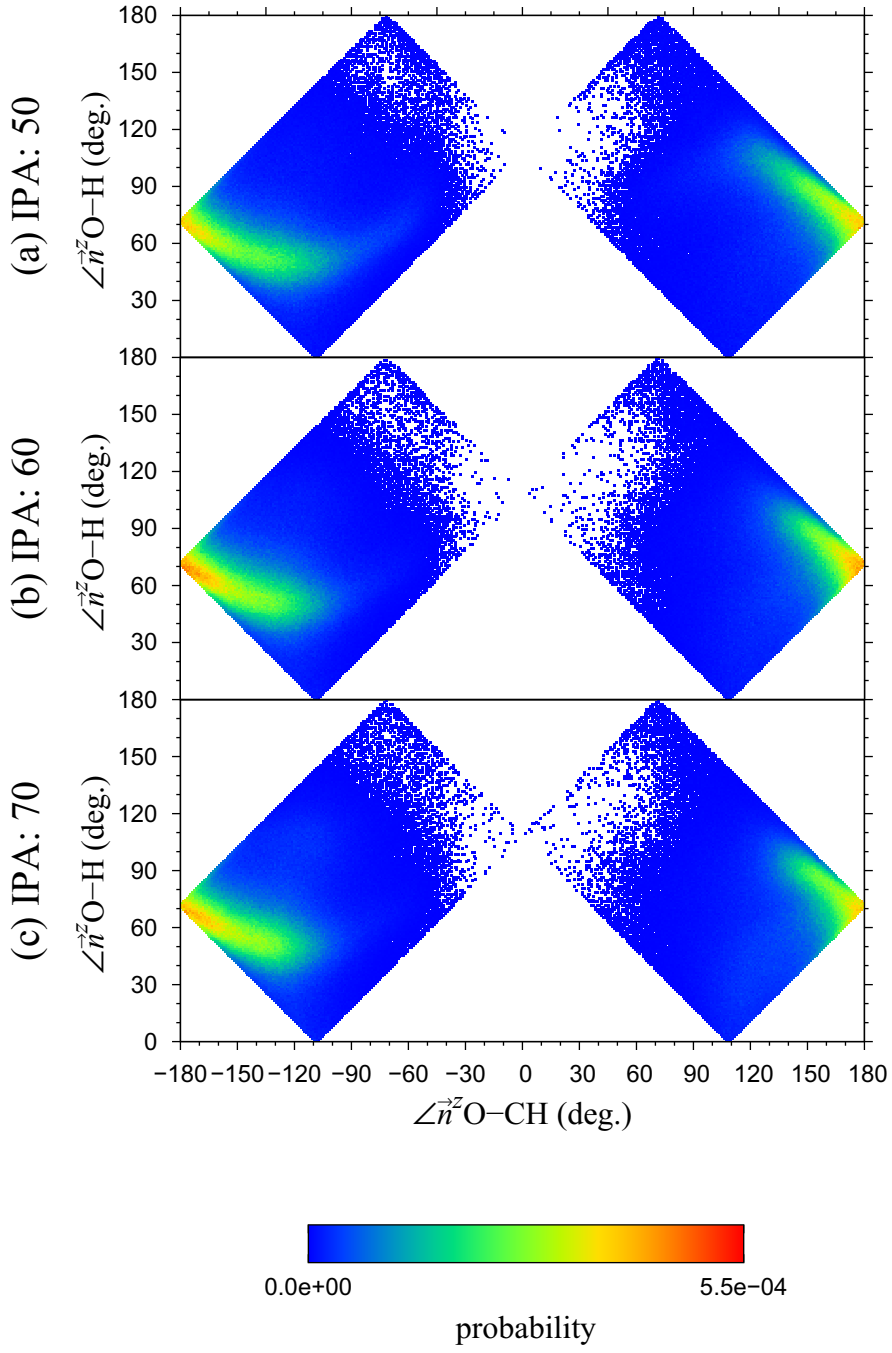

Figure 4.24: Probability distributions of angular configurations of IPA gauche conformer in the density peak nearest to the solid-liquid interface of water-IPA mixture systems (continue).

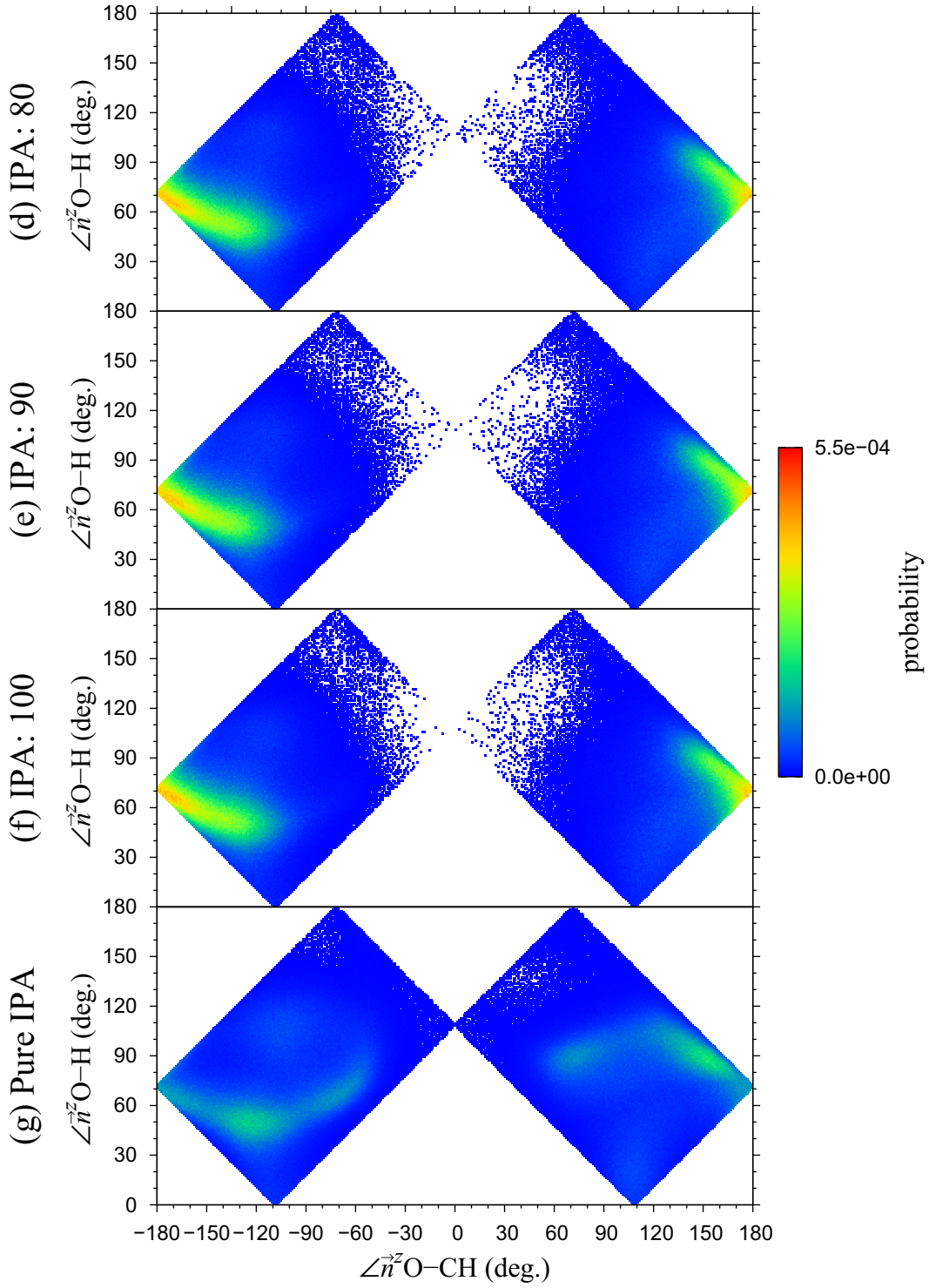

Figure 4.24: (Continued) Probability distributions of angular configurations of IPA gauche conformer in the density peak nearest to the solid-liquid interface of water-IPA mixture systems. Single-component system is also included for reference.

4.4 Interfacial Tensions

Interfacial tensions are calculated from the difference between normal and tangential pressures, using the method described in Section 2.5.1.

4.4.1 Systems with solid-liquid and liquid-vapor interfaces

Because there are two two-phase interfaces in the simulation systems containing solid-liquid and liquid-vapor interfaces as shown in Fig. 4.1, it is necessary to define interface regions. The interface regions are chosen to encompass the areas with density or pressure change and to be bounded at a position where tangential pressure P^T becomes equal to normal pressure P^T, i.e. where pressure becomes isotropic, so that the resulting interfacial tensions are not dependent on the exact boundary conditions.

While methanol fraction inside liquid bulk f^{bulk}_{MeOH} was proved to be a sufficient parameter to determine the state of each interface, relative IPA adsorption was chosen to express the state of each interface for water-IPA mixture droplets, because the IPA molecules do not diffuse into droplet bulk as shown in the density distribution in Figs. 4.6 and 4.7 and its fraction inside liquid bulk is not an appropriate parameter to express the interface state. The relative IPA adsorption for an interface between α and β phases $\Gamma^{\alpha\beta}_{\mathrm{IPA}}$ against an arbitrary Gibbs dividing surface is given by

$$\Gamma^{\alpha\beta}_{\mathrm{IPA}} = N^{\alpha\beta}_{\mathrm{IPA}} - N^{\alpha\beta}_{\mathrm{water}} \frac{n^{\beta}_{\mathrm{IPA}} - n^{\alpha}_{\mathrm{IPA}}}{n^{\beta}_{\mathrm{water}} - n^{\alpha}_{\mathrm{water}}}, \tag{4.1}$$

where n and N are number density and surface excess per unit area for each substance in each phase. Relative adsorption is an invariant independent of the location of the Gibbs dividing surface. Relative methanol adsorption $\Gamma^{\alpha\beta}_{\mathrm{MeOH}}$ can also be defined in an identical manner.

Solid-liquid and liquid-vapor interfacial tensions γ^{sl} and γ^{lv} for water-methanol and water-IPA mixtures are displayed in Figs. 4.25 and 4.27, in which methanol bulk fraction f^{bulk}_{MeOH} and relative IPA adsorption Γ_{IPA} at each interface are respectively adopted as parameters. Interfacial tension data for water-methanol mixtures in Fig. 4.25 is also displayed in Fig. 4.26, where relative methanol adsorption Γ_{MeOH} at each interface is used as parameter for easier comparison with water-IPA systems. The change of $\gamma^{sl}_{\mathrm{MeOH}}$, $\gamma^{lv}_{\mathrm{MeOH}}$ and $\gamma^{lv}_{\mathrm{IPA}}$ respectively shown in Figs. 4.26 (a), (b) and Fig. 4.27 (b) is gradual and each seems to approach the value of single-component alcohol at higher solvent amounts. The graphs of liquid-vapor interfacial tensions in Figs. 4.26 (b) and 4.27 (b) in particular are very linear, while the same water-methanol mixture data in Fig. 4.25 (b),

where methanol bulk fraction f_{MeOH}^{bulk} is used as a parameter, shows a clearly non-linear relation. This suggest that there is a linear relationship between the interfacial tension and the relative adsorption amount and indeed, interfacial tension can be expressed as a linear combination of surface free energy, chemical potential and relative adsorption amount as shown by Equation 2.70 in Section 2.5.3. Therefore, although in Section 4.3 it was shown that with larger alcohol concentrations the probability of dominating molecular orientations of alcohol molecules at interfaces greatly decreases as illustrated in Fig. 4.17 for methanol and Figs. 4.21 and 4.22 for IPA, this does not seem to have a noticeable effect on the liquid-vapor interfacial tensions.

Unlike other interfaces, a very steep decrease in the solid-liquid interfacial tension $\gamma_{\mathrm{IPA}}^{sl}$ of water-IPA mixture is observed in Fig. 4.27 (a), and this is thought to be due to the formation of a complete IPA mono-layer at the solid-liquid interface. This is also thought to be the reason why several data points seem to concentrate in close proximity at high relative adsorption of $\Gamma_{\mathrm{IPA}}^{sl} \geq 3.5$ nm^{-2}. The IPA mono-layer at the solid-liquid interface saturates at $\Gamma_{\mathrm{IPA}}^{sl} \geq 3.5$ nm^{-2} and any extra alcohol molecules are forced to occupy other interfaces and phases. This can be readily observed as solid-vapor interface moistening in Figs. 3.14 and 3.15 and as IPA diffusing into bulk in Fig. 4.7 (b, c), while no such behaviour is observed in water-methanol mixtures investigated in this work. Molecular orientations investigated in Section 4.3 show that although the structure of this IPA mono-layer is different from the adsorption layer of single-component IPA systems, it remains mostly unchanged and independent of IPA concentration as illustrated in Figs. 4.23 and 4.24. The density distribution graph of the water-IPA mixture system with the lowest IPA adsorption amount shown in Fig. 4.4 (a) is the only one with a considerable amount of water molecules inside the first density peak from the solid surface, therefore it appears that the IPA mono-layer has a distinct effect on the interfacial tension only when there are almost no water molecules remaining inside it.

The cause and meaning of the negative values of solid-liquid interfacial tensions in Figs. 4.25 (a), 4.26 (a) and 4.27 (a) should be addressed here. The interaction between solid particles is modeled with the harmonic potential shown in Equation 2.21, in which the interaction pairs are prescribed a priori to connect the nearest neighbors and potential energy is set to be zero at the equilibrium distance. Because of this, the total potential energy of the solid surface without thermal vibrations placed in vacuum is zero, and solid bulk has no energetic advantage over surface in this model, even though the particles at the surface have less interaction pairs than those in the bulk. If liquid

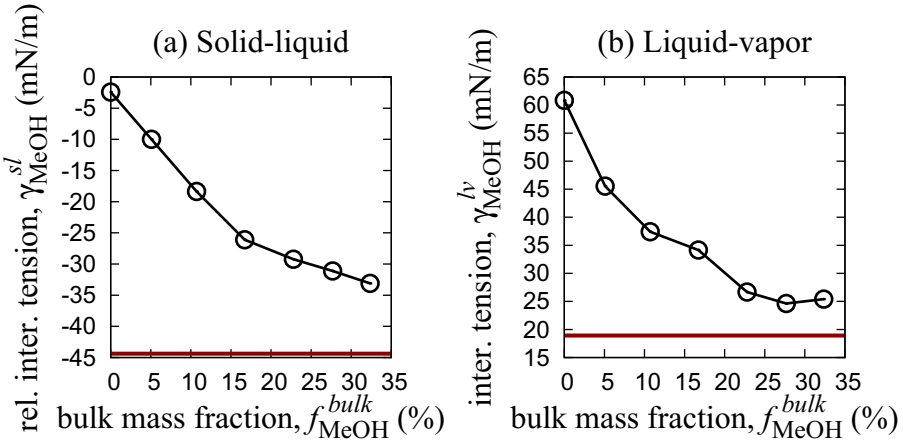

Figure 4.25: Dependence of solid-liquid and solid-vapor interfacial tensions for water-methanol mixtures on methanol bulk fraction evaluated in quasi-one-dimensional systems. Red horizontal lines show the values of single-component methanol. Note that the values provided for the solid-liquid interface are relative to that of solid-vacuum.

*Reprinted with permission from "D. Surblys, Y. Yamaguchi, K. Kuroda, M. Kagawa, T. Nakajima and H. Fujimura, The Journal of Chemical Physics, 140, 034505 (2014)". Copyright 2014, American Institute of Physics.

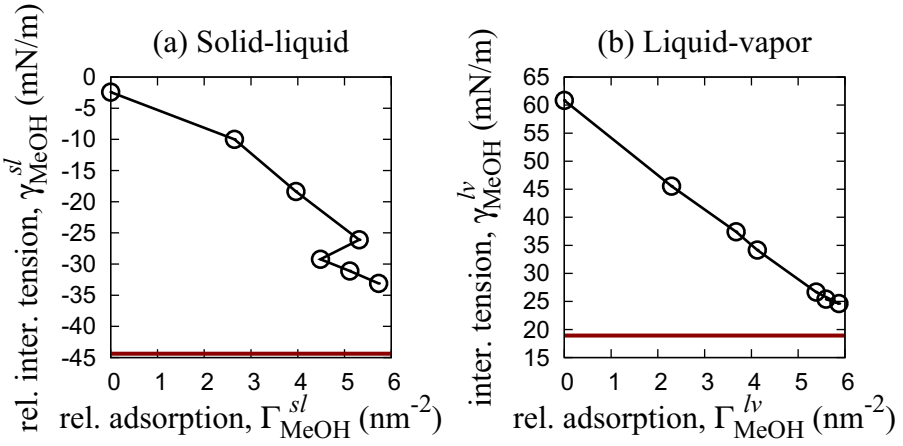

Figure 4.26: Dependence of solid-liquid and solid-vapor interfacial tensions in water-methanol mixtures on the relative methanol adsorption at each interface evaluated in quasi-one-dimensional systems. Red horizontal lines show the values of single-component methanol. Note that the values provided for the solid-liquid interface are relative to that of solid-vacuum.

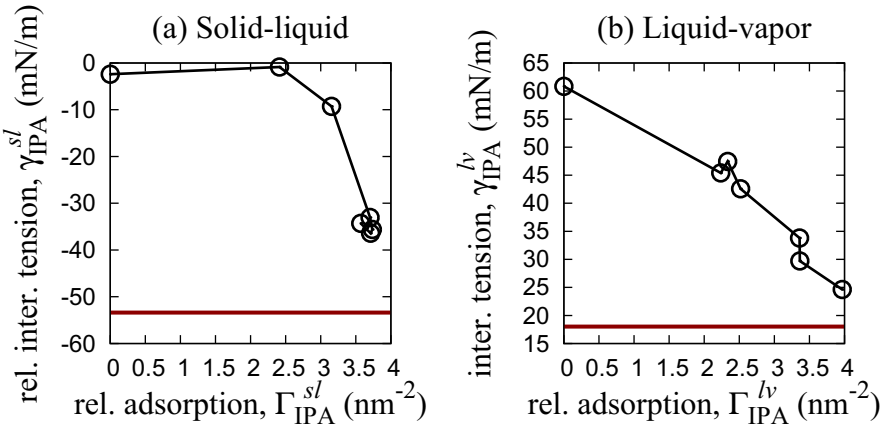

Figure 4.27: Dependence of solid-liquid and liquid-vapor interfacial tensions in water-IPA mixtures on the relative IPA adsorption at each interface evaluated in quasi-one-dimensional systems. Red horizontal lines show the values of single-component IPA. Note that the values provided for the solid-liquid interface are relative to that of solid-vacuum. *Reprinted with permission from "D. Surblys, Y. Yamaguchi, K. Kuroda, M. Kagawa, T. Nakajima and H. Fujimura, The Journal of Chemical Physics, 140, 034505 (2014)". Copyright 2014, American Institute of Physics.

molecules are adsorbed onto this solid surface, the total potential energy will become negative, since the L-J potential used for solid-liquid interactions has a negative well. This means that the solid-liquid and solid-vapor interfacial tensions calculated by the Bakker's equation in this and the next sections are relative to that of solid-vacuum. Since only the difference of the solid-liquid and solid-vapor interfacial tensions is needed, as shown in the Young's Equation 2.73, relative values are enough. On the other hand, the liquid-vapor interfacial tensions calculated by the Bakker's equation are absolute and always positive.

As a final note, the issue of inconsistencies in Figs. 4.26 (a) and 4.27 (b) should be addressed. For the solid-liquid interface graph of water-methanol systems in Fig. 4.26 at high methanol concentrations, the alcohol molecules at interfaces and that inside liquid bulk increase at a similar rate, producing close relative adsorption values for different systems. Because of this, mass fraction inside liquid bulk f^{bulk}_{MeOH} is used for water-methanol systems in later sections, although it should be possible to produce a smoother graph by increasing the number of data samples. The liquid-vapor interface graph of water-IPA systems in Fig. 4.27 (b) exhibits rougher curves than other graphs. This is a consequence of IPA molecules preferring to remain at the interfaces, being represented by a mixture of three rigid isotopes, and being larger than methanol ones. Because of this, it is thought that the liquid-vapor interface tends to remain at certain

local configurations. This might also explain why a stronger polarization of water molecules in liquid-vapor interfaces was observed in the two systems corresponding to Figs. 4.20 (c) and (d), which was inconsistent with other systems, although it is uncertain if these differences are related to change in interfacial tensions. Therefore even the sampling of several nanoseconds might not be enough to obtain a statistically reliable ensemble average.

4.4.2 Systems with solid-vapor interfaces

Because there is only one solid-vapor interface in the simulation system as seen from Fig. 4.2, the interface boundary is taken over the whole system. Since almost no molecules exist in the vapor phase, relative adsorption amount $\Gamma^{sv}_{\mathrm{IPA}}$ is calculated by simply dividing the number of IPA molecules by the cross-sectional area.

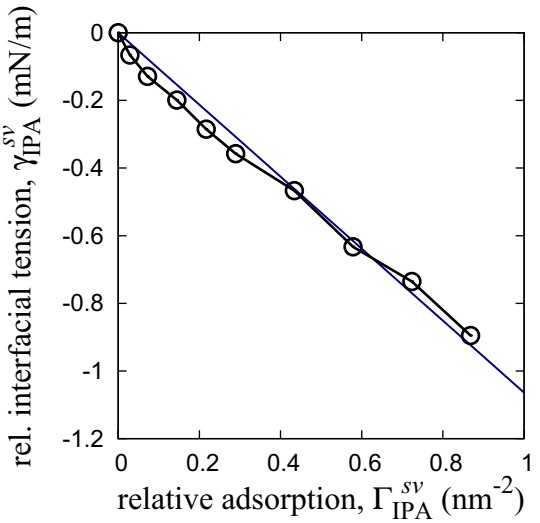

Figure 4.28: Dependence of solid-vapor interfacial tension on the relative IPA adsorption amount, evaluated in quasi-one-dimensional systems. A linear fitting is displayed with a blue line, where the fitting function is $\gamma^{sv} = \zeta \cdot \Gamma^{sv}_{\mathrm{IPA}}$ with $\zeta = -1.06 \times 10^{-21}$ [N · m]. Note that the values provided for the solid-vapor interface are relative to that of solid-vacuum. *Reprinted with permission from "D. Surblys, Y. Yamaguchi, K. Kuroda, M. Kagawa, T. Nakajima and H. Fujimura, The Journal of Chemical Physics, 140, 034505 (2014)". Copyright 2014, American Institute of Physics.

Solid-vapor interfacial tension for IPA molecules $\gamma^{sv}_{\mathrm{IPA}}$ plotted against IPA adsorption amount $\Gamma^{sv}_{\mathrm{IPA}}$ is shown in Fig. 4.28, with the cause and meaning of the negative tension values given in the previous section. A linear relationship clearly exists showing that the interfacial tension is proportional to the amount of IPA molecules at the solid-vapor interface. This would mean that droplet wettability would become worse if there was no change in the interfacial tensions of other interfaces. However, as can be confirmed in Fig. 4.27, changes in solid-liquid and liquid-vapor interfacial tensions are much greater, and this means that solid-vapor interface has hardly any effect on the mixture-droplet wettability. Because in water-methanol droplet systems, there are even less molecules in the solid-vapor interfaces as seen in Figs. 3.5 through 3.10, the solid-vapor interface is not investigated for methanol molecules and solid-vapor interfacial tension is considered to be always $\gamma^{sv}_{\mathrm{MeOH}} = 0$.

4.5 Force Balance at Interfaces

The positions of solid-liquid and liquid-vapor interfaces are calculated in this section using the method described in Section 2.6.

For solid-liquid interface, its position is expressed as the distance from the topmost solid surface layer, and the obtained values are displayed in Fig. 4.29. Systems with the number of alcohol molecules above 200 for water-methanol, and with that above 60 for water-IPA show similar solid-liquid interface positions of 0.2 nm $\leq Z^{sl} \leq$ 0.4 nm and do not vary significantly. On the other hand, water-methanol systems containing 100 and 200 alcohol molecules show much smaller values, while for water-IPA systems containing 50 and 60 alcohol molecules the interface positions become negative, i.e. below the solid surface. This is clearly unphysical and turned out to be due to the calculation error caused by the roughness of tangential pressure P^T distribution as seen in Figs. 4.4 through 4.7. The calculations concerning the balance of force, and therefore interfacial tension, are not affected by this, because only the integrated value is used as shown in Equations 2.66 and 2.80, and any roughness is cancelled out. This is not true for the balance of moment however, because the integration of the tangential pressure P^T is weighted with the z-coordinate as shown in Equation 2.81, and the jaggedness is no longer cancelled out and results in calculation error. This error is more apparent for systems containing interfacial tensions with small absolute values, which prevents obtaining reliable results for systems containing small amounts of alcohol molecules. Because of this, only consistent data circled in red in Fig. 4.29 obtained from systems with larger numbers of alcohol molecules is adopted to estimate the interface position used to measure the contact angles in Section 3.3.

For liquid-vapor interface, liquid density at the interface position was chosen because the resulting values are not dependent on the system dimensions. The densities at liquid-vapor interface for both water-methanol and water-IPA mixtures are displayed in Fig. 4.30. Remarkably, water-IPA mixtures in Fig. 4.30 (b) show very consistent density values, while the values for water-methanol mixtures in Fig. 4.30 (a) appear very inconsistent and sporadic. Specifically, water-methanol systems containing 400 and 500 alcohol molecules show unnaturally low densities. Since the absolute values of liquid-vapor interfacial tensions decrease with the increase in alcohol molecules, as discussed in Section 2.5, the error coming from roughness also increases, and the values change greatly depending on the integration region. The inconsistencies in water-methanol systems are thought to be a result of improperly chosen boundary conditions. By assuming that the density values of water-methanol at the solid-liquid interface are

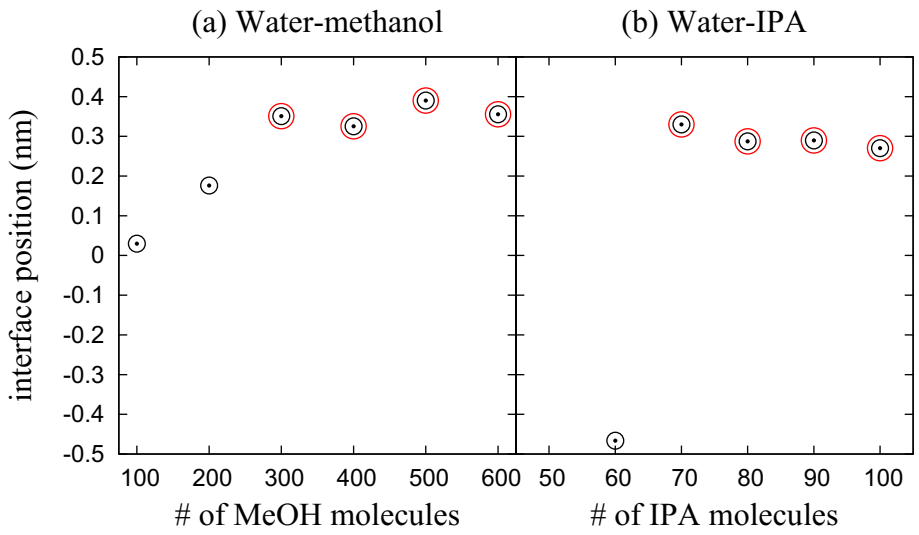

Figure 4.29: Solid-liquid interface positions for quasi-one-dimensional (a) water-methanol and (b) water-IPA mixture systems. The calculated interface position at the water-IPA mixture system with 50 IPA molecules is $Z^{sl} = -4.1$ nm, but is not displayed in order to maintain clarity. The average interface position used in Section 3.3 is calculated from the data points circled in red.

similar to those of water-IPA systems, the water-methanol systems containing 200 and 300 alcohol molecules were chosen to estimate the average density, while all data points were used for water-IPA systems. Although this obviously does not give a statistically reliable value, the chosen density of the liquid-vapor interface has a much smaller effect on the apparent contact angle than the elevation of the solid-liquid interface, therefore the introduced error is not considered to be substantial.

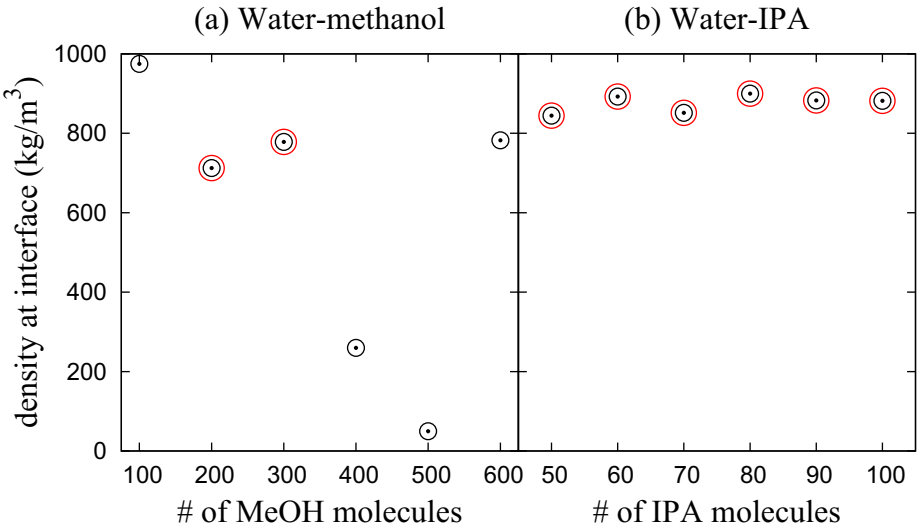

Figure 4.30: Liquid densities at liquid-vapor interfaces for quasi-one-dimensional (a) water-methanol and (b) water-IPA mixture systems. The average density at the interface position used in Section 3.3 is calculated from the data points circled in red.

5

SYSTEMS USED FOR THERMODYNAMIC INTEGRATION

Bakker's equation was used to evaluate interfacial tensions in Section 4.4 under the assumption that the interfaces cannot support elastic strain.[19] This is not the case however for solid-liquid and solid-vapor interfaces where the solid molecules at the surface are allowed to vibrate around their equilibrium positions, and thus can indeed support strain.[58] This results in the following Shuttleworth equation:

$$s = \gamma + \frac{\mathrm{d}\gamma}{\mathrm{d}\varepsilon}, \tag{5.1}$$

where s and ε are interfacial stress and elastic strain, respectively. Because of this, using Bakker's equation on solid-liquid and solid-vapor interfaces is appropriate only when the solid surface is completely periodic or a potential wall, such as described by Eq. 2.110. An alternative measuring way is needed to accurately evaluate the interfacial tension when the second term in the right hand side of Eq. 5.1 is non-zero.

An additional type of quasi-one-dimensional simulation systems is constructed in a similar manner to systems in Chapter 4 to independently assess solid-liquid interfacial tensions by using thermodynamic integration as described in Section 2.5.3.

5.1 Simulation System and Conditions

Snapshots of equilibrated single-component water, methanol and IPA systems are shown in Fig. 5.1. Periodic boundary conditions are imposed in all lateral directions and the liquid inside is composed of either 3000 water, 1500 methanol or 1000 IPA

molecules. Two solid surfaces each containing three layers are symmetrically located at the center of the calculation cell, with innermost layers being 3 nm apart. The position of solid atoms in the innermost layers is fixed and the temperature of those in the middle layers is controlled by the Langevin method at 298.15 K. In addition, two sets of three potential walls recreating the mean potential field of the solid surface are also placed symmetrically to the xy-plane. Thirty-seven simulation systems are created for each liquid type with the innermost potential planes being apart from 0 to 6 nm. As well as the integration methods and temperature control used in the previous systems, additional temperature and pressure control is applied to the liquid phase with thermostat and barostat relaxation times τ_T and τ_p set to 2 and 5 ps respectively and pressure set to atmospheric value using the control schemes described in Sections 2.3.2 and 2.4.4. To reduce the effect on the system, the relaxation times are approximately 10 times longer than what would be the minimal ones recommended in the original paper[45] for an L-J liquid with the potential parameters of the oxygen atom in the SPC/E model. Only the z-component of the local pressure tensor in the liquid phase is controlled and the pressure control region starts at 0.175 nm outwards from the equilibrium position of the plane closest to the liquid phase, and no surface or liquid molecules are present at this region. The size of calculation region in x- and y-directions is the same as the systems in Chapter 4: 3.358×3.047 nm^2, while that in z-direction is initially set to 30 nm but this decreases greatly due to the pressure control scheme. After 1 ns of equilibration, the average of simulation for 8 ns data is used to analyze systems with the potential planes closest and furthest apart, while the average of data for 2 ns is used for all others in-between. The time step is set to $h = 1$ fs in accordance to the quasi-one-dimensional systems in Chapter 4.

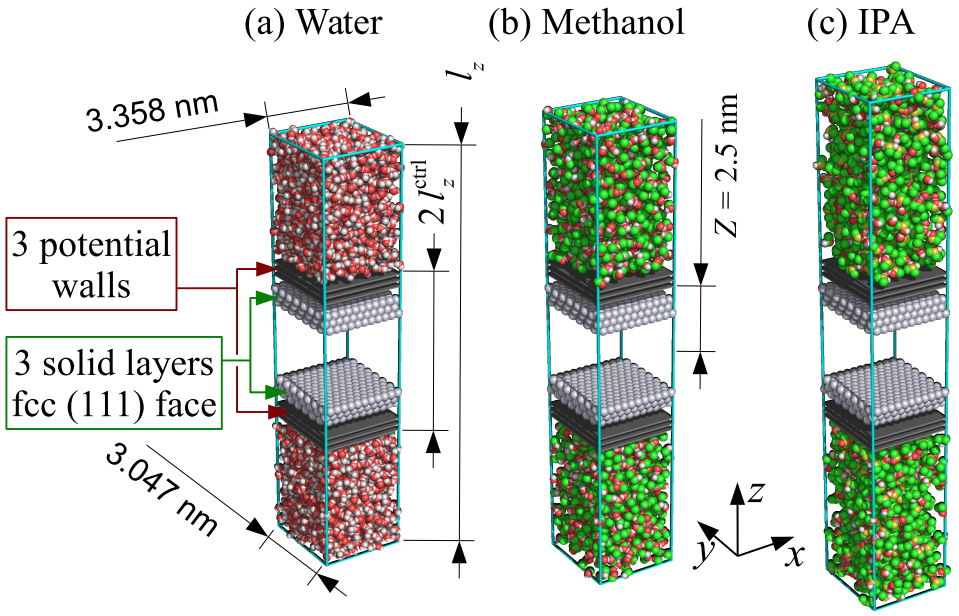

Figure 5.1: Snapshots of single-component (a) water, (b) methanol and (c) IPA simulation system used to independently assess solid-liquid interfacial tensions. Cell size in the z-dimension l_z varies due to the pressure control scheme, and l_z^{ctrl} indicates the distance of the pressure control region from the system center, with details given in Section 2.4.4. The innermost potential plane distance from the system center is set to $Z = 2.5$ nm for all the systems in the snapshots.

5.2 Pressure Exerted on Potential Walls

The pressure exerted on the potential walls is shown in Fig. 5.2. All of the graphs show a similar trend with the pressure being negative at $Z < 1.5$ nm and positive at $Z > 1.5$ nm, i.e. potential walls are attracted towards the liquid components at $Z < 1.5$ nm, and pushed back by the liquid components at $Z > 1.5$ nm. The peaks of water component are slightly smaller than those of methanol and IPA, showing a weaker interaction between water and solid surface than that between alcohol and solid surface. This is to be expected, since the absolute value of the solid-liquid interfacial tension of water is much smaller than that of either methanol or IPA as seen in Figs. 4.25 and 4.27 respectively.

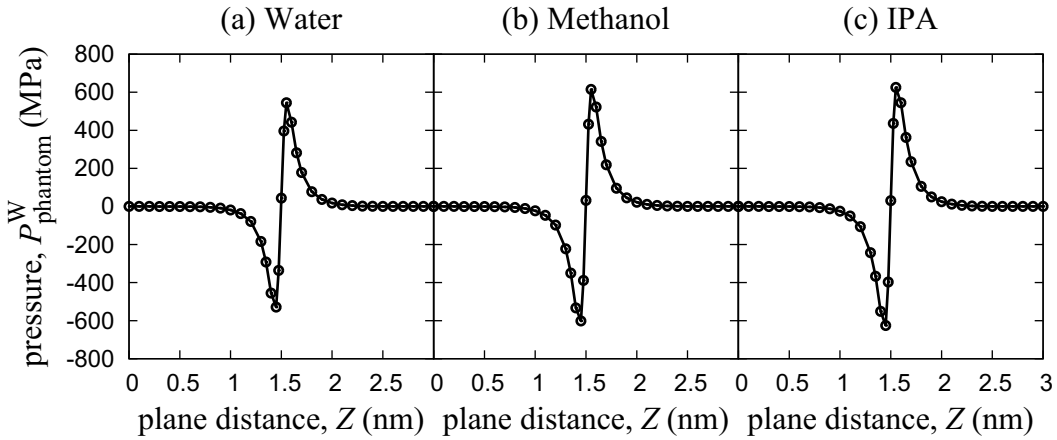

Figure 5.2: Relation between pressure exerted on the potential walls and distance between innermost potential wall and the center of the systems such as shown in Fig. 5.1. The two solid walls are positioned 1.5 nm from the center of the calculation cell.

*Reprinted with permission from "D. Surblys, Y. Yamaguchi, K. Kuroda, M. Kagawa, T. Nakajima and H. Fujimura, The Journal of Chemical Physics, 140, 034505 (2014)". Copyright 2014, American Institute of Physics.

5.3 Density and Pressure Distributions

The density and pressure distributions are provided for systems with the potential planes closest and furthest apart. The same methodology is used as already described in Section 4.2. The results for systems, where the potential planes are at $Z = 0$ and $Z = 3$ nm from the system center, are respectively shown in Figs. 5.3 and 5.4. Because intermolecular interaction range in this study is set to $r_{\text{cut}} = 1.5$ nm, no interaction between the potential walls and liquid molecules occurs for systems of Fig. 5.3, while for Fig. 5.4 nothing interacts with the solid surfaces. Therefore, Figs. 5.3 and 5.4 effectively show density and pressure distributions of systems containing liquid molecules and only either solid surfaces or potential walls, and can be used to evaluate the difference between solid-liquid interfaces. Qualitatively, density and pressure distributions seem to only depend on the liquid component. This is to be expected, because the potential walls have been specifically constructed to recreate the main potential field of the solid surface.

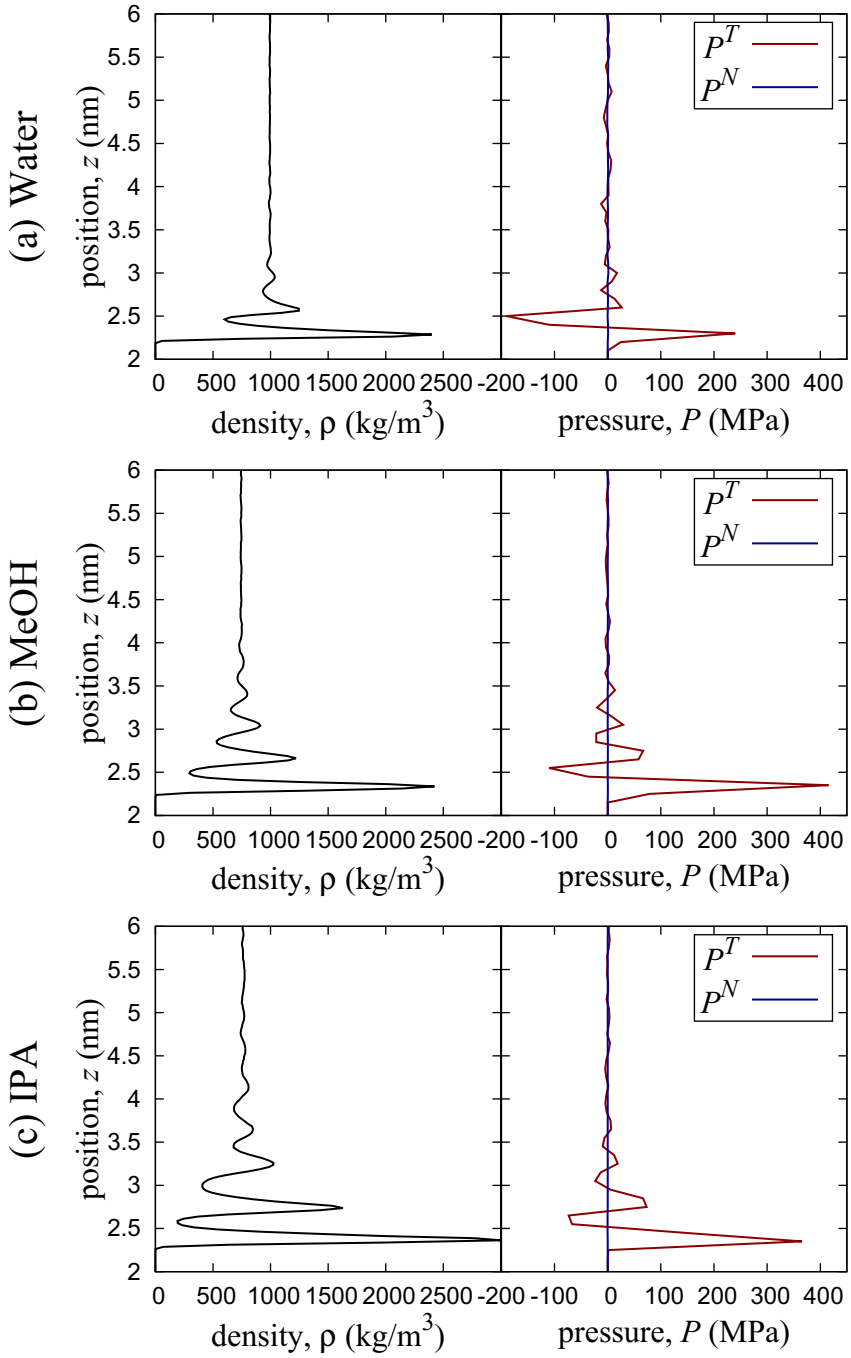

Figure 5.3: Density and pressure distributions of single-component systems, composed of either 3000 water, 1500 methanol or 1000 IPA molecules when the potential walls are at $Z = 0$ from the center of the system. The distributions are averaged with taking system symmetry into account.

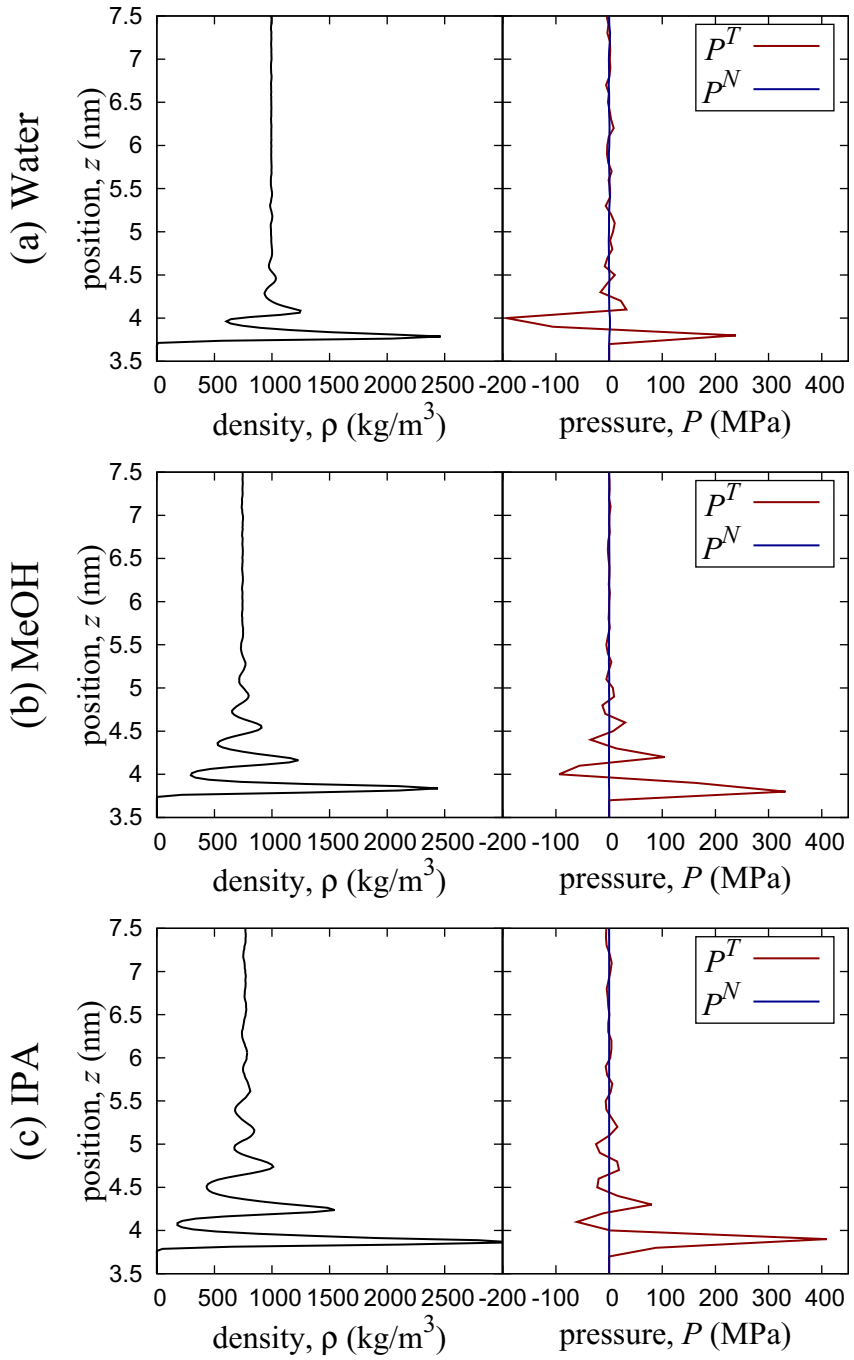

Figure 5.4: Density and pressure distributions of single-component systems, composed of either 3000 water, 1500 methanol or 1000 IPA molecules when the potential walls are at $Z = 3$ nm from the center of the system. The distributions are averaged with taking system symmetry into account.

Table 5.1: Difference in Gibbs free surface energy of solid-liquid interface between solid surface and potential wall together with interfacial tensions obtained using various methods. Note that the values are relative to the interfacial tension of solid-vacuum.
*Reprinted with permission from "D. Surblys, Y. Yamaguchi, K. Kuroda, M. Kagawa, T. Nakajima and H. Fujimura, The Journal of Chemical Physics, 140, 034505 (2014)". Copyright 2014, American Institute of Physics.

	Water	Methanol	IPA
$\gamma^{sl}_{\text{solid}} - \gamma^{sl}_{\text{phantom}}$ (mN/m)	−2.37	−1.66	−0.92
$\gamma^{sl}_{\text{phantom}}$ (mN/m)	−1.12	−46.15	−51.97
$\gamma^{sl}_{\text{solid}}$ (mN/m)	−3.50	−47.81	−52.89
$\gamma^{sl}_{\text{Bakker}}$ (mN/m)	−2.16	−45.22	−53.97

5.4 Interfacial Tensions

In this section interfacial tension difference is evaluated from the data displayed in Fig. 5.2 using thermodynamic integration as described in Section 2.5.3. In addition to this, Bakker's equation described in Section 2.5.1 and also used in Section 4.4 is used with data shown in Figs. 5.3 and 5.4 to directly calculate interfacial tensions $\gamma^{sl}_{\text{Bakker}}$ and $\gamma^{sl}_{\text{phantom}}$ at $Z = 0$ nm and $Z = 3$ nm respectively. Here, $\gamma^{sl}_{\text{Bakker}}$ is the value obtained by using Bakker's equation directly on the solid surface. The results are summarized in Table 5.1. All of the interfacial tensions have negative values, and this might seem unphysical, but this is only because they are relative to that of solid-vacuum, and this was discussed in greater detail in Section 4.4. It is interesting to note that solid surfaces have lower solid-liquid interfacial tensions than potential walls for all liquids. This is to be expected, since the solid surface has a structure which allows liquid molecules to take more energetically stable configurations, and that should result in decreasing the interfacial energy compared to a flat potential wall. This is also confirmed by the fact that the difference is greater for water and methanol with smaller molecule size than IPA. The interfacial tensions obtained by Bakker's equation and those obtained by thermodynamic integration only differ by about 2.6 mN/m at most. This is because the solid surface used in this work is a perfect fcc crystal with only minor thermal vibration and a small lattice spacing compared to the size of liquid molecules, and therefore approximating it as a flat potential wall does not produce a large error. This is effectively done by the Bakker's integration with only using solid-liquid interaction contribution to normal pressure as already described in Section 4.2. It is expected that the error would be much larger for rough or amorphous surfaces.

6

CONTACT ANGLES AND INTERFACIAL TENSIONS

6.1 Applicability of Young's equation

Young's equation describing the horizontal balance of interfacial tensions that was discussed in Sections 2.5.4 and 2.5.5 gives a way to predict the droplet contact angle from interfacial tensions calculated in Chapter 4 by treating the droplet as having zero thickness interfaces. The three-phase interface is not considered and only the interfacial data away from it is used, with the reasoning given in Section 2.5.5.

Alcohol fractions in liquid bulk region of a droplet and relative alcohol adsorption amounts at each interface away from the three-phase line are calculated for the water-methanol and water-IPA droplet systems and the results are shown in Figs. 6.1 and 6.2, respectively. The alcohol fractions in Fig. 6.1 reflect the observations made Figs. 3.5 through 3.10 in Section 3.2 that methanol molecules dissolve into the droplet bulk much easier than IPA molecules. In addition, the relative adsorption amounts of each interface in Fig. 6.2 reveal that the solid-liquid interface in a water-IPA droplet at $f_{\mathrm{IPA}} > 15$ % is saturated by the creation of a mono-layer and excess alcohol molecules start to overflow into the solid-vapor interface, while no such distinct signs of saturation can be observed for water-methanol droplets. Some of preliminary results indicate that the interface also saturates for water-methanol mixtures at a high enough alcohol ratio, but because methanol readily dissolves into water, this only means that the increase rates of interfacial and bulk alcohol become similar, describing a completely different state from the saturation seen in water-IPA.

Interfacial tensions are estimated by linear interpolation of the data shown in Figs. 4.25 and 4.27 (a, b) for solid-liquid and liquid-vapor interfaces or by the lin-

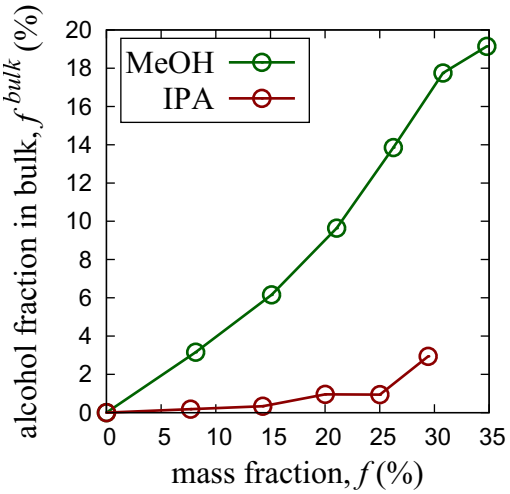

Figure 6.1: Methanol and IPA fractions in liquid bulk in relation to the overall mass fractions in droplet systems. The IPA fraction in liquid bulk is not used in determining droplet interfacial tensions and is only displayed for reference.
*Reprinted with permission from "D. Surblys, Y. Yamaguchi, K. Kuroda, M. Kagawa, T. Nakajima and H. Fujimura, The Journal of Chemical Physics, 140, 034505 (2014)". Copyright 2014, American Institute of Physics.

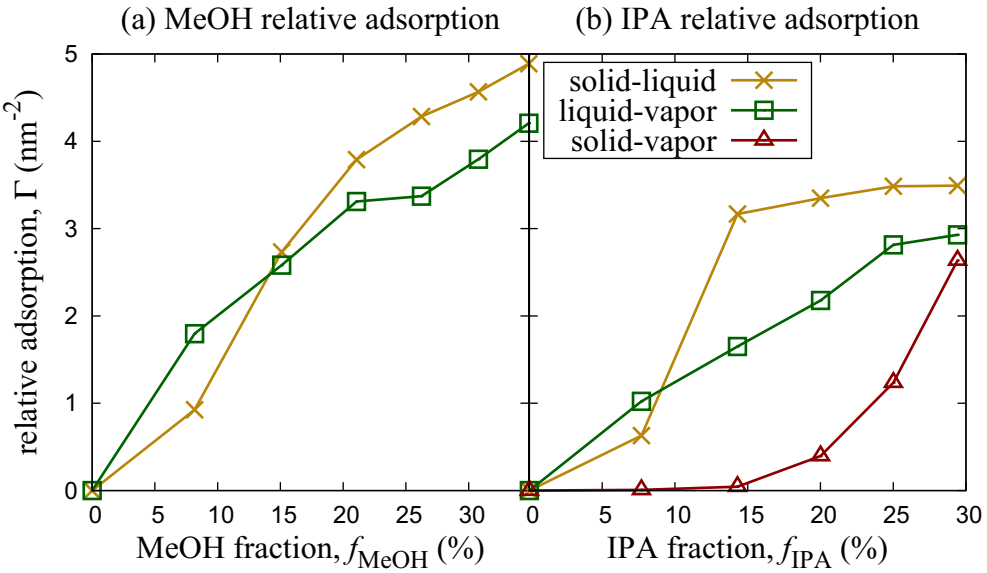

Figure 6.2: (a) Water-methanol and (b) water-IPA relative adsorption amounts at each droplet interface. The water-methanol relative adsorption amounts are not used in determining droplet interfacial tensions and are only displayed for reference.
*Reprinted with permission from "D. Surblys, Y. Yamaguchi, K. Kuroda, M. Kagawa, T. Nakajima and H. Fujimura, The Journal of Chemical Physics, 140, 034505 (2014)". Copyright 2014, American Institute of Physics.

ear fitting function shown in Fig. 4.28 for solid-vapor interfacial tension with IPA. The solid-vapor interfacial tension for water-methanol mixture droplets is assumed to be always zero.

The predicted contact angles are compared with the measured ones in Fig. 6.3. Although there are some discrepancies, a good quantitative agreement can be seen. This means that our method accurately predicts interfacial tensions and shows that Young's approach is still applicable even at nano-scale.

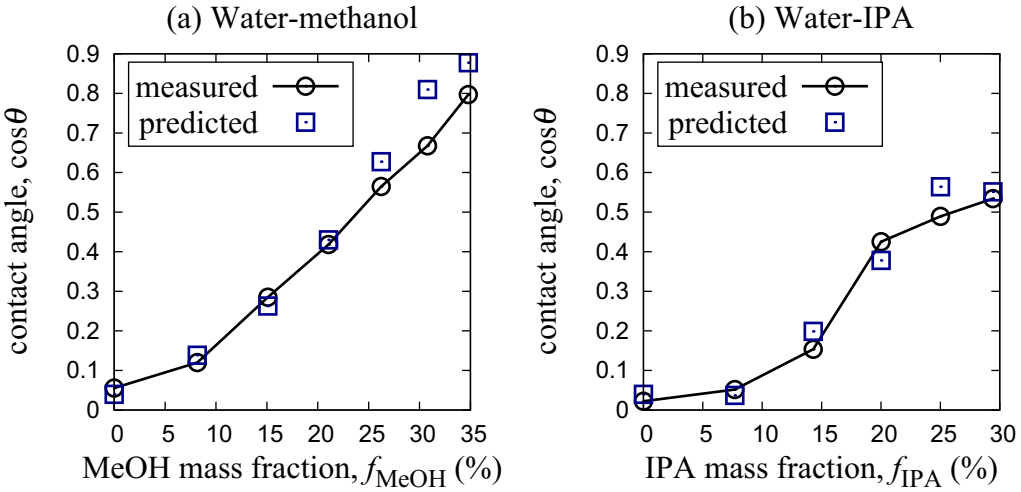

Figure 6.3: Relation between the cosine of contact angle of the water-alcohol mixture droplets and alcohol mass fractions.

*Reprinted with permission from "D. Surblys, Y. Yamaguchi, K. Kuroda, M. Kagawa, T. Nakajima and H. Fujimura, The Journal of Chemical Physics, 140, 034505 (2014)". Copyright 2014, American Institute of Physics.

6.2 Margin of Error Brought by Using Bakker's Equation

It has already been discussed in Chapter 5 that it is not strictly appropriate to use Bakker's equation for interfaces containing a surface that can support strain, and it has been confirmed in Section 5.4 that Bakker's equation does indeed produce slight error in the solid-liquid interfacial tensions for single-component liquids. The same procedure cannot be easily applied to multi-component liquids, because there is a need to obtain the chemical potential of each component, which is a non-trivial task. Instead, data summarized in Table 5.1 are used to estimate the effect of Bakker's equation on mixture liquids. By comparing the interfacial tensions of single-component systems obtained by directly using Bakker's equation $\gamma^{sl}_{\text{Bakker}}$ and thermodynamic integration $\gamma^{sl}_{\text{solid}}$, it is possible to roughly approximate the margin of error introduced by using Bakker's equation on the solid-liquid interfaces of mixtures.

For water and methanol systems, thermodynamic integration produced lower interfacial tensions, and the methanol data showing a larger discrepancy was chosen to approximate the margin of error for water-methanol systems. On the other hand, thermodynamic integration for IPA systems produced higher interfacial tensions, thus both water and IPA data were used for water-IPA systems to give an error range in both directions. The results are displayed in Fig. 6.4. The error bars show that although of similar order, the uncertainty brought by the Bakker's equation does not explain the discrepancies between measured and predicted contact angles, indicating that other sources of uncertainty exist.

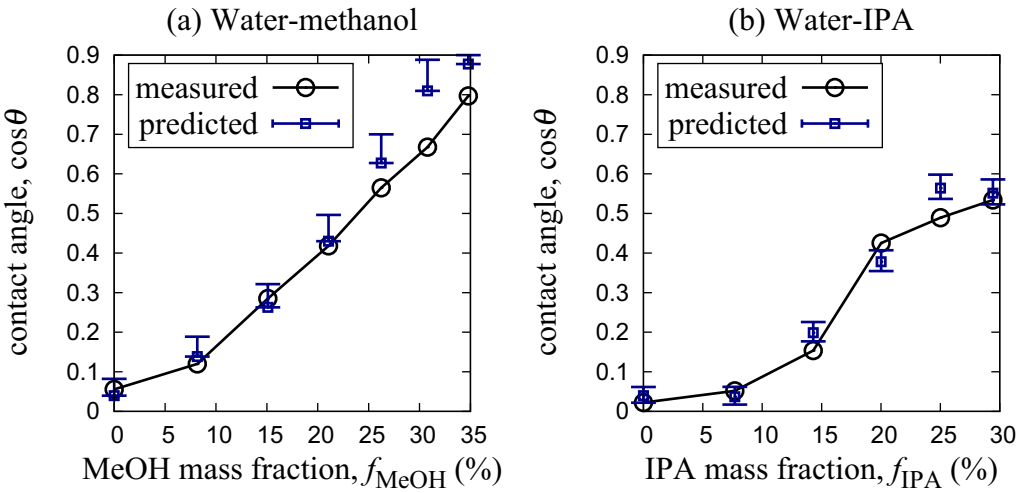

Figure 6.4: Relation between the cosine of contact angle of the water-alcohol mixture droplets and alcohol mass fraction. Error bars show the uncertainty incurred by using Bakker's equation on a solid-liquid interface.

*Reprinted with permission from "D. Surblys, Y. Yamaguchi, K. Kuroda, M. Kagawa, T. Nakajima and H. Fujimura, The Journal of Chemical Physics, 140, 034505 (2014)". Copyright 2014, American Institute of Physics.

6.3 Reevaluation of Liquid-Vapor Interfacial Tensions

It is a well-known fact that liquid-vapor interfacial tension is influenced by the droplet curvature,[48] and this is especially remarkable for very small droplets, such as in this paper. The method of using flat interfaces does not take this into account and therefore some degree of error is expected, which could explain the discrepancies in Fig. 6.4 that the error induced by Bakker's equation could not fully capture.

Because of the relationship between droplets radius and its Laplace pressure as described in Section 2.5.2, it is possible to obtain liquid-vapor interfacial tensions without direct calculation of the pressure tensor. The droplet radii obtained when measuring apparent contact angles in Chapter 3.3 are displayed in Fig. 6.5. The radius R of the droplets increases with larger alcohol mass fractions f, which is in accord with measured contact angles in Fig. 3.16.

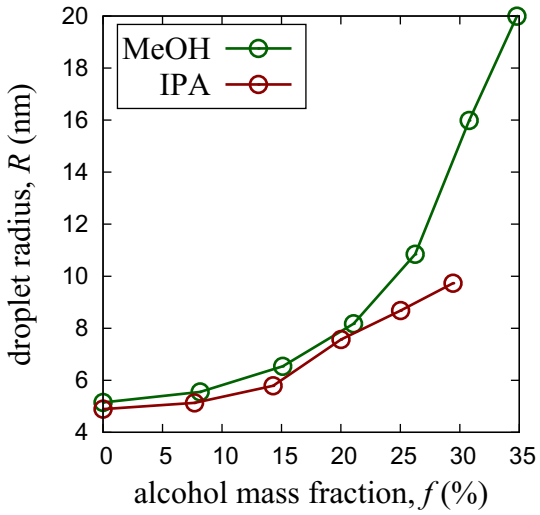

Figure 6.5: Dependence of droplet radius on alcohol mass fraction in water-methanol and water-IPA systems.

Liquid-vapor interfacial tensions obtained from flat interfaces in Chapter 4 and those obtained from the Young-Laplace Equation 2.69 using data in Figs. 3.20 and 6.5 are compared in Fig 6.6.

Before discussing the result, irregular behaviour observed in solid-liquid interfacial tensions obtained by Laplace equation for both water-methanol and water-IPA droplets illustrated with red lines in Fig. 6.6 should be addressed. No such large discrepancies can be observed in either Laplace pressure or droplet radius graphs displayed in Figs. 3.20 and 6.5, respectively. However, because interfacial tension from Laplace

equation is obtained by multiplying the two data, any small discrepancies increase multiplicatively. It is reasonable to assume that the radii are of high precision, because they are obtained from density distribution of the droplets. On the other hand, Laplace pressure is obtained from the intermolecular force, which is a differential quantity, and therefore has much greater fluctuations and a greater margin of error. The fact that the discrepancies are larger at high alcohol concentrations, i.e. at higher radii, also supports the above-mentioned possibility that the discrepancies are due to uncertainty coming from Laplace pressure measurement.

For both water-methanol and water-IPA systems in Fig. 3.20, liquid-vapor interfacial tension of droplets is smaller than that of flat planes, and this would mean that surface tension decreases at small droplet radius, which is both theoretically sound and observed in literature.[48] On the other hand, droplet surface tension becomes larger than that of planar interface at higher alcohol concentrations. It is not believed that a circular interface can have a larger interfacial tension than a planar one, therefore this indicates that either the droplet radius used to obtain Laplace pressure is incorrect or that there are factors besides the droplet curvature that increase the uncertainty in interfacial tension values obtained from flat interfaces.

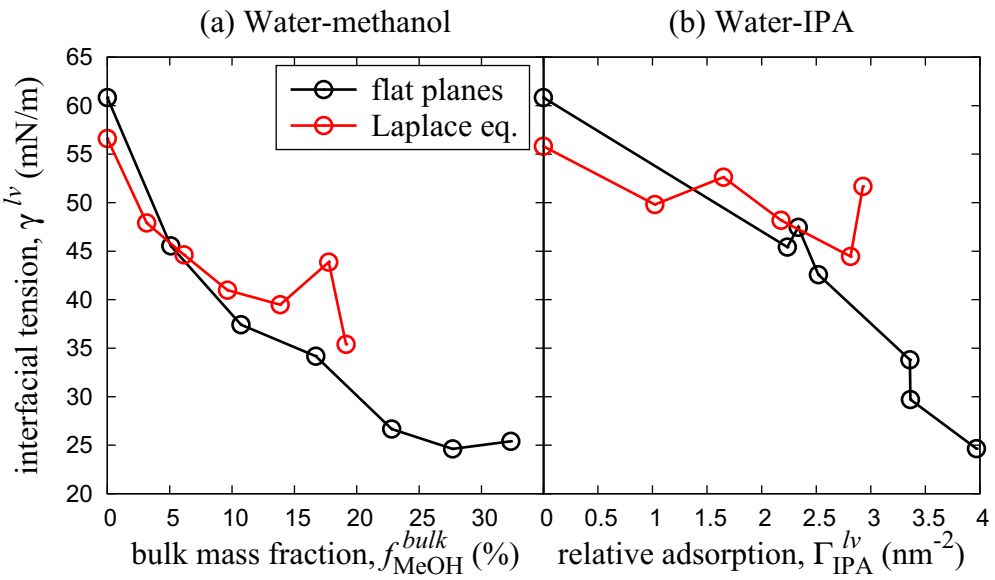

Figure 6.6: Comparison of liquid-vapor interfacial tensions obtained from flat interfaces in Chapter 4 and those obtained from water-methanol and water-IPA droplets using Young-Laplace Equation 2.69

Figure 6.7 displays the measured contact angles together with predicted ones using liquid-vapor interfacial tensions obtained from both Young-Laplace Equation 2.69 and

planar interface data in Section 4.4, where the uncertainty induced from using the Bakker's equation on solid-liquid interfaces is also shown by error bars. If we choose to ignore the data points at $f_{\mathrm{MeOH}} = 31$ % and $f_{\mathrm{IPA}} = 29$ %, where the liquid-vapor interfacial tension was highly irregular compared to other values, then predictions using solid-liquid interfacial tensions obtained from Young-Laplace equation seem to be more precise for water-methanol mixtures at high methanol concentrations at $f_{\mathrm{MeOH}} > 20$ %, while being comparable in other cases. Because there is a systematic overestimation of the water-methanol contact angles at this range when using $\gamma^{lv}_{\mathrm{MeOH}}$ from planar interfaces, it is safe to assume that the liquid-vapor interfacial tensions predicted from planar interfaces are indeed incorrect. On the other hand, this is not observed for water-IPA mixtures, therefore the cause of the error is not interfacial curvature. Three is a strong possibility that using bulk mass fraction to describe the state of water-methanol liquid-vapor interfaces at high alcohol concentrations is not completely adequate and introduces a systematic error.

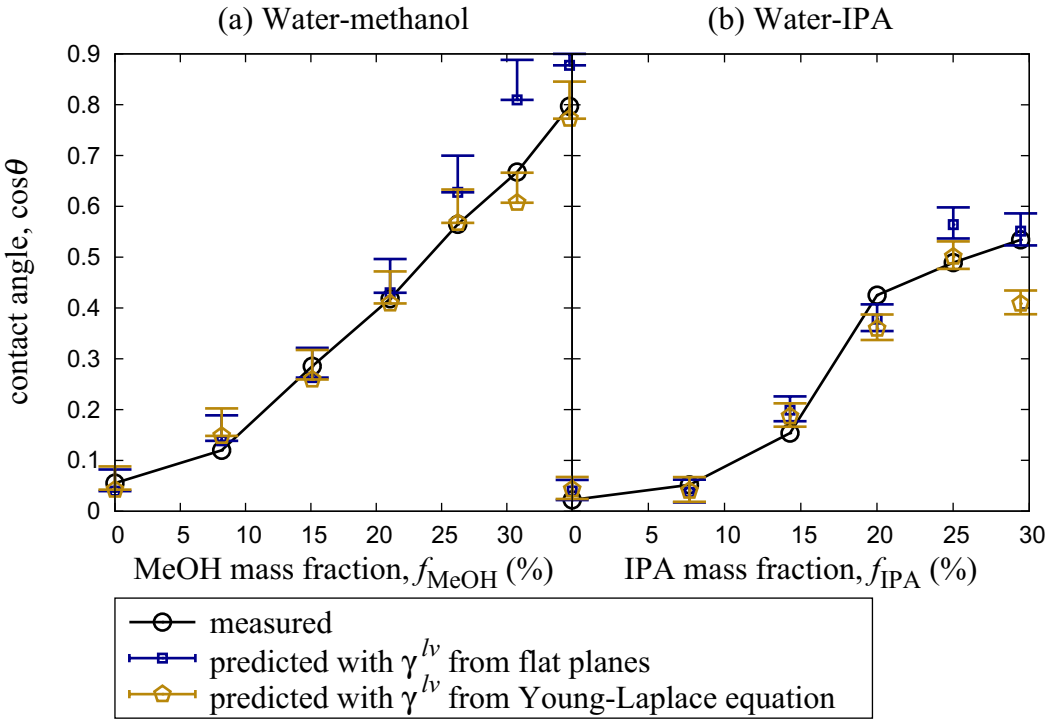

Figure 6.7: Relation between the cosine of contact angle of the water-alcohol mixture droplets and alcohol mass fraction. Error bars show the uncertainty incurred by using Bakker's equation on a solid-liquid interface.

7

CONCLUSIONS

In this study, simulations of water-methanol and water-IPA (isopropyl-alcohol) mixture droplets on a solid surface were performed using molecular dynamics (MD) method to understand better the effect that alcohol additives have on the wettability of water droplet. Simulations of quasi-one-dimensional systems were also performed to quantitatively calculate two-phase interfacial tensions. Finally, the validity of using quasi-one-dimensional systems to predict droplet wettability was investigated for both solid-liquid and liquid-vapor interfaces.

In Chapter 3 water-methanol and water-IPA droplets were created on a solid surface. The droplets generally became more wettable with larger alcohol fractions and both water-methanol and water-IPA mixtures achieved similar wettability at similar alcohol mass fractions. Both types of alcohol molecules showed a strong preference to gather at solid-liquid and liquid-vapor interfaces, and a clear tendency to gather at the three-phase interface was also observed at very low mixture ratios. At high mixture ratios, methanol molecules diffused well into the droplet bulk, while IPA molecules were found to spread out to the solid-vapor interface with almost no molecules dissolving inside the liquid droplet, thus creating two very different mixture systems. The IPA unwillingness to diffuse into droplet bulk is thought to mainly come from the large hydrophobic group. The obtained results such as difference in solubility are highly dependent on the mixing rules, and while the Lorentz-Berthelot rules used in this work do not accurately reproduce experimentally observed mixture properties, the general tendencies are thought to be qualitatively similar. The Laplace pressure inside the droplets was also calculated, and it was confirmed that it decreased as droplets became more wettable, which corresponds well with the macro-scale model.

In Chapter 4 specific two-phase interfacial tensions were calculated in quasi-one-dimensional simulation systems for flat interfaces using Bakker's equation with pres-

sure tensor distribution. Liquid-vapor interfacial tensions of both water-methanol and water-IPA mixtures and solid-liquid interfacial tension of water-methanol mixtures decreased gradually and there was a linear relationship between the interfacial tension values and the relative adsorption amount of alcohol molecules at each interface. On the other hand, a very steep drop and saturation in the solid-liquid interfacial tension of water-IPA mixtures was observed after reaching a specific interfacial alcohol concentration, and this was attributed to the formation of an IPA mono-layer which appeared to have a certain preferable number density and interfacial tension. No such sudden change was observed for water-methanol mixtures, although there also existed a distinct methanol mono-layer at the solid-liquid interface. This was attributed to the fact that methanol readily diffuses into water bulk, thus the formation of the mono-layer is much less restrictive. It is thought that because pure alcohol liquids have lower interfacial tensions than water, alcohol molecules covering the interfaces is the main reason for the decrease of the interfacial tensions there, although none of the mixture interfaces managed to decrease to the interfacial tension value of a single-component alcohol. It was found that the solid-vapor interfacial tensions changed very little and had a negligible effect on wettability even for systems where the solid-vapor interface was clearly moistened by IPA molecules.

In Chapter 5, thermodynamic integration was used as an alternative method to calculate the solid-liquid interfacial tensions of quasi-one-dimensional systems containing single-component liquid. There it was confirmed that the Bakker's equation produces a slight error when used for a solid-liquid interface, where the solid can support elastic strain. Because the solid surface used in this work was a perfect fcc crystal with only minor thermal vibration and small lattice spacing compared to the size of liquid molecules, the error was small, but it is expected that the error would be much larger for rough or amorphous surfaces.

In Chapter 6, droplet interfacial tensions were assessed from the data obtained in the quasi-one-dimensional systems in Chapter 4 using relative interfacial adsorption amount and bulk alcohol fraction as parameters to describe the interfacial states of water-IPA and water-methanol systems, respectively. This produced good quantitative estimation of the contact angle based on the Young's equation, indicating that the macroscopic approach of horizontal interfacial tension balance used in wetting theory is still valid at nano-scale and that we could reliably predict the droplet interfacial tensions. It was discovered that the uncertainty that the Bakker's equation brought into wettability estimation was of the same magnitude as the discrepancies between

the measured and calculated contact angles, although the discrepancies could not be explained by only this. Liquid-vapor interfacial tensions of droplets were alternatively evaluated using the Young-Laplace equation, and this produced better contact angle estimates than the interfacial tensions obtained from the planar interfaces for water-methanol systems with high alcohol mass fractions, while the results in other cases were comparable. This indicates that the alcohol mass fraction inside droplet bulk was not and adequate parameter to describe the water-methanol droplet states at high alcohol concentrations, while no such problems were observed for water-IPA mixtures where relative adsorption amounts of interfacial alcohol were used.

The primary objectives of this research were to investigate the effect of alcohol additives on droplet wettability and to validate if the wetting theory used in the macro-scale was still applicable to nano-scale mixture droplets. These objectives were successfully achieved by directly investigating the change in the interfacial tensions and other interfacial properties of water-alcohol mixture systems, which allowed to prove that even mixture droplet systems of vastly different compositions follow the same principles described by the macroscopic wetting theory, i.e. Young's equation, when an idealized model of interfaces with zero thickness is applied. Although addition of alcohol to water is a well-known way to increase wettability, directly observing interfacial tensions showed that the change in wettability in our systems was due to the decrease of not only liquid-vapor but also solid-liquid interfacial tensions. A secondary objective to evaluate the validity of methods used to obtain the solid-liquid and liquid-vapor interfacial tensions was also achieved. Unfortunately, a detailed evaluation of the solid-liquid interface was only done for single-component liquid systems, and a rather crude assessment had to be made for mixture systems. In principle, it was possible to do the same assessment using mixture systems, although the need to calculate the chemical potential would have arisen. A better evaluation of simulation uncertainty would have also greatly eased the validation process. None the less, it is expected that this new knowledge and insight will be helpful in improving the techniques and methods of controlling droplet wettability. This research only deal with a non-polar and almost ideally smooth solid surface, but the methods described in this work should also be applicable to rougher or polarized surfaces.

References

[1] W. Barthlott and C. Neinhuis. **Purity of the sacred lotus, or escape from contamination in biological surfaces**. *Planta*, **202**(1):1–8, 1997.

[2] Y. T. Cheng, D. E. Rodak, C. A. Wong, and C. A. Hayden. **Effects of micro-and nano-structures on the self-cleaning behaviour of lotus leaves**. *Nanotechnology*, **17**:1359, 2006.

[3] U. Bauer, M. Scharmann, J. Skepper, and W. Federle. **Insect aquaplaning on a superhydrophilic hairy surface: how Heliamphora nutans Benth. pitcher plants capture prey**. *Proc. R. Soc. B*, **280**(1753), 2013.

[4] A. Y. Stark, I. Badge, N. A. Wucinich, T. W. Sullivan, P. H. Niewiarowski, and A. Dhinojwala. **Surface wettability plays a significant role in gecko adhesion underwater**. *Proc. Natl. Acad. Sci.*, 2013.

[5] T. Young. **An Essay on the Cohesion of Fluids**. *Philos. Trans. R. Soc. London*, **95**:65–87, 1805.

[6] K. Narayan Prabhu, Peter Fernades, and Girish Kumar. **Effect of substrate surface roughness on wetting behaviour of vegetable oils**. *Mater. Des.*, **30**(2):297–305, 2009.

[7] X. Zhao, M. J. Blunt, and J. Yao. **Pore-scale modeling: Effects of wettability on waterflood oil recovery**. *J. Petrol. Sci. Eng.*, **71**(34):169–178, 2010.

[8] M. Sakai, T. Yanagisawa, A. Nakajima, Y. Kameshima, and K. Okada. **Effect of Surface Structure on the Sustainability of an Air Layer on Superhydrophobic Coatings in a WaterEthanol Mixture**. *Langmuir*, **25**(1):13–16, 2009.

[9] Z. Pawlak, A. D. Petelska, W. Urbaniak, K. Q. Yusuf, and A. Oloyede. **Relationship Between Wettability and Lubrication Characteristics of the Surfaces of Contacting Phospholipid-Based Membranes**. *Cell Biochem. Biophys.*, **65**(3):335–345, 2013.

[10] Y. Son, C. Kim, and D. J. Yang, D. H. Ahn. **Spreading of an Inkjet Droplet on a Solid Surface with a Controlled Contact Angle at Low Weber and Reynolds Numbers**. *Langmuir*, **24**(6):2900–2907, 2008.

[11] J. G. Park and M. F. Pas. **Effects of Drying Methods and Wettability of Silicon on the Formation of Water Marks in Semiconductor Processing**. *J. Electrochem. Soc.*, **142**(6):2028–2031, 1995.

[12] L. R. White. **On deviations from Young's equation**. *J. Chem. Soc., Faraday Trans. 1*, **73**:390–398, 1977.

[13] L. Boruvka and A. W. Neumann. **Generalization of the classical theory of capillarity**. *J. Chem. Phys.*, **66**(12):5464–5476, 1977.

[14] A. Marmur. **Line Tension and the Intrinsic Contact Angle in SolidLiquidFluid Systems**. *J. Coll. Interf. Sci.*, **186**(2):462–466, 1997.

[15] M. N. Popescu, G. Oshanin, S. Dietrich, and A. M. Cazabat. **Precursor films in wetting phenomena**. *J. Phys.: Condens. Matter*, **24**(24):243102, 2012.

[16] W. R. Tyson and W. A. Miller. **Surface free energies of solid metals: Estimation from liquid surface tension measurements**. *Surf. Sci.*, **62**(1):267–276, 1977.

[17] V. K. Kumikov and Kh. B. Khokonov. **On the measurement of surface free energy and surface tension of solid metals**. *J. Appl. Phys.*, **54**(3):1346–1350, 1983.

[18] J. G. Kirkwood and F. P. Buff. **The Statistical Mechanical Theory of Surface Tension**. *J. Chem. Phys.*, **17**:338–343, 1949.

[19] M. J. P. Nijmeijer and J. M. J. van Leeuwen. **Microscopic expressions for the surface and line tension**. *J. Phys. A: Math. Gen.*, **23**:4211–4235, 1990.

[20] M. J. P. Nijmeijer, C. Bruin, A. F. Bakker, and J. M. J. van Leeuwen. **Wetting and drying of an inert wall by a fluid in a molecular-dynamics simulation**. *Phys. Rev. A*, **42**:6052–6059, 1990.

[21] S. K. Das and K. Binder. **Does Young's equation hold on the nanoscale? A Monte Carlo test for the binary Lennard-Jones fluid**. *Europhy. Lett.*, **92**(2):26006, 2010.

[22] D. Seveno, T. D. Blake, and J. De Coninck. **Young's Equation at the Nanoscale**. *Phys. Rev. Lett.*, **111**:096101, Aug 2013.

[23] J. Z. Tang and J. G. Harris. **Fluid wetting on molecularly rough surfaces**. *J. Chem. Phys.*, **103**:8201–8208, 1995.

[24] S. Maruyama, T. Kuruashige, S. Matsumoto, Y. Yamaguchi, and T. Kimura. **Liquid Droplet in Contact With A Solid Surface**. *Microscale Thermophys. Eng.*, **2**:40, 1998.

[25] F. Bresme and N. Quirke. **Computer simulation of wetting and drying of spherical particulates at a liquid-vapor interface**. *J. Chem. Phys.*, **110**:3536–3547, 1999.

[26] P. van Remoortere, J. E. Mertz, L. E. Scriven, and H. T. Davis. **Wetting behavior of a Lennard-Jones system**. *J. Chem. Phys.*, **110**:2621–2628, 1999.

[27] S. Nishida, D. Surblys, Y. Yamaguchi, K. Kuroda, M. Kagawa, T. Nakajima, and H. Fujimura. **Molecular dynamics analysis of multiphase interfaces based on in situ extraction of the pressure distribution of a liquid droplet on a solid surface**. *J. Chem. Phys.*, **140**(7):074707, 2014.

[28] G. Vazquez, E. Alvarez, and J. M. Navaza. **Surface Tension of Alcohol Water + Water from 20 to 50 .degree.C**. *J. Chem. Eng. Data*, **40**(3):611–614, 1995.

[29] P. H. Winterfeld, L. E. Scriven, and H. T. Davis. **An approximate theory of interfacial tensions of multicomponent systems: Applications to binary liquid-vapor tensions**. *AIChE*, **24**(6):1010–1014, 1978.

[30] B. S. Carey, L. E. Scriven, and H. T. Davis. **Semiempirical theory of surface tension of binary systems**. *AIChE*, **26**(5):705–711, 1980.

[31] J. Escobedo and G. A. Mansoori. **Surface-tension prediction for liquid mixtures**. *AIChE*, **44**:2324–2332, 1998.

[32] M. A. Wilson and A. Pohorille. **Adsorption and Solvation of Ethanol at the Water LiquidVapor Interface: A Molecular Dynamics Study**. *J. Phys. Chem. B*, **101**(16):3130–3135, 1997.

[33] T. M. Chang and L. X. Dang. **LiquidVapor Interface of MethanolWater Mixtures: A Molecular Dynamics Study**. *J. Phys. Chem. B*, **109**:5759–5765, 2005.

[34] F. Biscay, A. Ghoufi, and P. Malfreyt. **Surface tension of wateralcohol mixtures from Monte Carlo simulations**. *J. Chem. Phys.*, **134**(4):044709, 2011.

[35] M. Lundgren, N. L. Allan, and T. Cosgrove. **Wetting of Water and Water/Ethanol Droplets on a Non-Polar Surface: A Molecular Dynamics Study**. *Langmuir*, **18**:10462–10466, 2002.

[36] H. J. C. Berendsen, J. R. Grigera, and T. P. Straatsma. **The missing term in effective pair potentials**. *J. Phys. Chem.*, **91**:6269–6271, 1987.

[37] W. L. Jorgensen, J. D. Madura, and C. J. Swenson. **Optimized intermolecular potential functions for liquid hydrocarbons**. *J. Am. Chem. Soc.*, **106**:6638–6646, 1984.

[38] W. L. Jorgensen. **Optimized intermolecular potential functions for liquid alcohols**. *J. Phys. Chem.*, **90**:1276–1284, 1986.

[39] G. Bussi, D. Donadio, and M. Parrinello. **Canonical sampling through velocity rescaling**. *J. Chem. Phys.*, **126**:014101, 2007.

[40] H. J. C. Berendsen, J. P. M. Postma, W. F. van Gunsteren, A. DiNola, and J. R. Haak. **Molecular Dynamics with Coupling to an External Bath**. *J. Chem. Phys.*, **81**:3684–3690, 1984.

[41] J. Blömer and A. E. Beylich. **Molecular dynamics simulation of energy accommodation of internal and translational degrees of freedom at gassurface interfaces**. *Surf. Sci.*, **423**:127–133, 1999.

[42] R.G. Winkler, H. Morawitz, and D.Y. Yoon. **Novel molecular dynamics simulations at constant pressure**. *Mol. Phys.*, **75**(3):669–688, 1992.

[43] J. H. Irving and J. G. Kirkwood. **The Statistical Mechanical Theory of Transport Processes. IV. The Equations of Hydrodynamics**. *J. Chem. Phys.*, **18**:817–829, 1950.

[44] J. G. Weng, S. Park, J. R. Lukes, and C. L. Tien. **Molecular dynamics investigation of thickness effect on liquid films**. *J. Chem. Phys.*, **113**:5917–5923, 2000.

[45] G. Bussi, T. Zykova-Timan, and M. Parrinello. **Isothermal-isobaric molecular dynamics using stochastic velocity rescaling**. *J. Chem. Phys.*, **130**:074101, 2009.

[46] F. Leroy, D. J. V. A. dos Santos, and F. Müller-Plathe. **Interfacial Excess Free Energies of SolidLiquid Interfaces by Molecular Dynamics Simulation and Thermodynamic Integration**. *Macromol. Rapid Commun.*, **30**:864–870, 2009.

[47] S. W. Ip and J. M. Toguri. **The equivalency of surface tension, surface energy and surface free energy**. *J. Mat. Sci.*, **29**:688–692, 1994.

[48] H. Yaguchi, T. Yano, and S. Fujikawa. **Molecular Dynamics Study of Vapor-Liquid Equilibrium State of an Argon Nanodroplet and Its Vapor**. *J. Fluid Sci. Tech.*, **5**:180–191, 2010.

[49] I. P. Omelyan. **On the Numerical Integration of Motion for Rigid Polyatomics: The Modified Quaternion Approach**. *Computers Phys.*, **12**:97–103, 1998.

[50] N. S. Martys and R. D. Mountain. **Velocity Verlet Algorithm for Dissipative-Particle-Dynamics-Based Models of Suspension**. *Phys. Rev. E*, **59**:3733–3736, 1999.

[51] R.S. Taylor, L.X. Dang, and B.C. Garrett. **Molecular Dynamics Simulations of the Liquid/Vapor Interface of SPC/E Water**. *J. Phys. Chem.*, **100**(28):11720–11725, 1996.

[52] M.P. Gelfand and M.E. Fisher. **Finite-size effects in surface tension: Thermodynamics and the Gaussian interface model**. *Int. J. Thermophys.*, **9**(5):713–727, 1988.

[53] M.P. Gelfand and M.E. Fisher. **Finite-size effects in fluid interfaces**. *Phys. A*, **166**(1):1–74, 1990.

[54] L.J. Chen. **Area dependence of the surface tension of a LennardJones fluid from molecular dynamics simulations**. *J. Chem. Phys.*, **103**(23):10214–10216, 1995.

[55] S.W. Sides, G.S. Grest, and M.D. Lacasse. **Capillary waves at liquid-vapor interfaces: A molecular dynamics simulation**. *Phys. Rev. E*, **60**:6708–6713, Dec 1999.

[56] A.E Ismail, G.S. Grest, and M.J Stevens. **Capillary waves at the liquid-vapor interface and the surface tension of water**. *J. Chem. Phys.*, **125**(1):–, 2006.

[57] M. C. Goh, J. M. Hicks, K. Kemnitz, G. R. Pinto, T. F. Heinz, K. B. Eisenthal, and K. Bhattacharyya. **Absolute orientation of water molecules at the neat water surface**. *J. Chem. Phys.*, **92**(18):5074–5075, 1988.

[58] J. R. Henderson, P. Tarazona, F. van Swol, and E. Velasco. **Weighted density functional theories of drying at solidfluid interfaces: Clarification of recent controversies**. *J. Chem. Phys.*, **96**:4633–4638, 1992.

Publication List

[1] D. Surblys, Y. Yamaguchi, K. Kuroda, T. Nakajima, and H. Fujimura. **Analysis on wetting and local dynamic properties of single water droplet on a polarized solid surface: A molecular dynamics study**. *J. Chem. Phys.*, **135**(1):014703, 2011.

[2] S. Nakaoka, D. Surblys, Y. Yamaguchi, K. Kuroda, T. Nakajima, and H. Fujimura. **Local viscosity change in water near a solidliquid interface and its extraction by means of molecular rotational diffusion A molecular dynamics study**. *Chem. Phys. Lett.*, **591**:306–311, 2014.

[3] D. Surblys, Y. Yamaguchi, K. Kuroda, M. Kagawa, T. Nakajima, and H. Fujimura. **Molecular dynamics analysis on wetting and interfacial properties of water-alcohol mixture droplets on a solid surface**. *J. Chem. Phys.*, **140**(3):034505, 2014.

[4] S. Nishida, D. Surblys, Y. Yamaguchi, K. Kuroda, M. Kagawa, T. Nakajima, and H. Fujimura. **Molecular dynamics analysis of multiphase interfaces based on in situ extraction of the pressure distribution of a liquid droplet on a solid surface**. *J. Chem. Phys.*, **140**(7):074707, 2014.

Acknowledgements

I would like to express my deep gratitude to Associate Professor Yasutaka Yamaguchi for his continuous guidance and encouragement throughout this research and the preparation of this thesis. This work would not have been possible without his invaluable assistance.

I am especially grateful to Professor Takeo Kajishima, Professor Takeru Yano and Professor Masahiko Shibahara for their review of this thesis work.

I am also greatly indebted to Koji Kuroda, Tadashi Nakajima, Hideo Fujimura and Masaru Kagawa of Dai Nippon Printing Co., Ltd. for providing valuable experimental data and guidance.

I would also like to express my appreciation to Assistant Professor Takeshi Omori for fruitful discussion in numerous study meetings held between members of our laboratories.

Thanks go to our laboratory secretary Yukari Saito for her assistance during my studies in Yamaguchi Laboratory for all this time.

I would also like to acknowledge the Japanese Ministry of Education, Culture, Sports, Science and Technology for granting me a scholarship and enabling my studies in Japan.

I am also grateful for the support from JSPS KAKENHI Grant Number 25807.

I would also like to express my thanks and gratitude to all the members in Yamaguchi Laboratory, Mechanical Engineering Department, Osaka University for their cooperation and assistance in making this research possible.

Finally, I would like to thank my parents for providing me with so many opportunities in life and their unconditional support and encouragement throughout my studies.